THE UNIVERSITY OF MICHIGAN
COLLEGE OF ENGINEERING
Department of Nuclear Engineering

Te^{125} MÖSSBAUER EFFECT STUDY OF RADIATION EFFECTS AND MAGNETIC HYPERFINE STRUCTURE IN TELLURIUM COMPOUNDS

John F. Ullrich
Dietrich H. Vincent

ORA Project 07921

supported by:

NATIONAL SCIENCE FOUNDATION
GRANT NO. GK-871
WASHINGTON, D.C.

administered through:

OFFICE OF RESEARCH ADMINISTRATION ANN ARBOR

July 1967

This report was also a dissertation submitted by the first author in partial fulfillment of the requirements for the degree of Doctor of Philosophy in The University of Michigan, 1967.

ACKNOWLEDGEMENTS

I am deeply grateful for the patient and helpful guidance and advice provided throughout my academic career, and most particularly through the course of this work, by Professor Dietrich Vincent.

The advice and assistance on numerous aspects of the research by the other members of the doctoral committee: Professor A. Ziya Akcasu, Professor Chihiro Kikuchi, and Professor Paul G. Rasmussen, are also deeply appreciated.

I want to express particular thanks to Mr. Poh-Kun Tseng for his kind help and many interesting discussions.

I am grateful to the entire staff of the Phoenix Memorial Laboratory for the technical and administrative help they provided. Particular thanks are due the personnel of the Ford Nuclear Reactor for their assistance in many sample irradiations, but more particularly for their willing cooperation in monitoring experiments and filling with liquid nitrogen during overnight runs.

Financial support of the research was provided by the National Science Foundation (Grant GK 871). Support in the early stages of the research was provided by the National Aeronautics and Space Administration (Grant NsG-115-61) and the Michigan Memorial-Phoenix Project (Project 310). Financial assistance during my academic career was provided by three Atomic Energy Commission Special Fellowships in Nuclear Science

and Engineering and a University of Michigan Rackham Pre-doctoral Fellowship.

I would like to thank Miss Helen Walker for the excellent job done in preparing the final manuscript under rather trying circumstances.

The most heartfelt expression of gratitude is due my wife, Sue, for her untiring support and encouragement during the course of this thesis. Our children, Frederick, Kathryn, and Amy, also deserve recognition for the enjoyable respites they provided.

CONTENTS

TABLES

FIGURES

ABSTRACT

The purpose of the first part of this study was to experimentally determine the effects of neutron capture induced defects on Mössbauer hyperfine spectra in Te^{125}. Thermal neutron capture in Te^{124} is used to simultaneously produce the Mössbauer isomeric state parent Te^{125m} and to introduce the parent nucleus as a defect in the lattice. The displacement mechanism is the recoil of the nucleus due to the emission of 6.4 Mev of "prompt" gamma rays following the neutron capture. Since the Mössbauer hyperfine spectrum is sensitive to the immediate electronic environment of the emitting nucleus, the Mössbauer spectrum should provide information on characteristic defect environments.

The effects were experimentally investigated by irradiating tellurium compounds enriched in Te^{124} with thermal neutrons. The Mössbauer resonance absorption spectrum was then measured against a single line absorber. This spectrum should be characteristic of the lattice with the atoms displaced from the normal lattice sites. The spectrum characteristic of the "ideal" lattice was obtained using the same sources following heat treatment to restore the atoms to their normal lattice environment.

The measurements were performed using sources of PbTe, Te metal, and TeO_2. For all three compounds, there were no statistically significant differences in the pre-anneal and post-anneal Mössbauer hyperfine spectra. Differences of

several percent in the resonance intensity are within the experimental accuracy of the measurement.

The lack of any significant changes in the hyperfine spectra may be due to either: a) a recoil energy too low to produce displacements; b) replacement collisions; c) defect annealing; or d) insignificant changes in hyperfine interaction parameters.

The purpose of the second part of this study was to experimentally investigate magnetic hyperfine spectra in magnetic compounds of tellurium. The diamagnetic Te^{2-} ion with paired 5s and 5p electrons would not normally be expected to give rise to a magnetic hyperfine field at the Te nucleus. However, in compounds with the transition metals, the magnetically coupled transition metal ions can act to spin polarize the paired electron shells of the tellurium ion. The unpaired tellurium 5s electron spins will have a net spin density at the tellurium nucleus and will give rise to a magnetic hyperfine field through the Fermi contact interaction.

Mössbauer resonance absorption measurements in the ferromagnetic spinel $CuCr_2Te_4$ show a partially resolved magnetic hyperfine pattern. From the least squares curve fitting to the data, the magnetic moment for the 3/2 + excited state of Te^{125} was determined to be $\mu_e = +.74 \pm .07$ nm. The internal hyperfine field was measured as $H_{eff} = 148 \pm 5$ kgauss. The unpairing of the tellurium 5s electrons in the spinel probably arises through either covalent mixing of the 5s electrons with the

chromium 3d electrons or exchange polarization of the 5s electrons by the chromium 3d electrons.

Mössbauer resonance absorption measurements in antiferromagnetic MnTe and ferromagnetic CrTe show only broadened lines. The broadening in MnTe is presumably due to unresolved quadrupole splitting, whereas the broadening in CrTe is probably unresolved magnetic hyperfine splitting.

CHAPTER I.

INTRODUCTION

A. Motivation for Present Study

Recoilless emission and absorption of nuclear gamma radiation (the Mössbauer effect) was discovered in 1958. The hyperfine structure in Mössbauer spectra has provided a very valuable tool for study of the solid state. From the spectra it is possible to gain information on lattice binding forces, internal magnetic fields and electric field gradients, and s-electron densities at the nucleus. This information can consequently provide an understanding of the electron environment of the Mössbauer emitting or absorbing nucleus.

In the past few years the use of the Mössbauer effect as a solid state probe has been applied to the study of radiation effects. The interest has developed in part from the expanded use of new techniques for population of the Mössbauer level. Traditionally, the Mössbauer level has been populated by the beta decay of a parent nuclide. In many cases low lying nuclear levels which should be potential Mössbauer levels are inaccessible by such decays. Many new techniques have been developed recently in an attempt to make Mössbauer effect measurement in these nuclides possible. These techniques include alpha decay, Coulomb excitation, nuclear reactions, and thermal neutron activation. The use of these techniques has caused concern for the effects of the method of production on the environment of the Mössbauer emitting nucleus.

Considerable interest has also developed in the use of the Mössbauer effect as a tool for study of radiation induced defects in solids. The Mössbauer effect is rather unique as a tool for study of the defect solid state in that the spectra are characteristic of only the immediate environment of the emitting nucleus. Such information is not obtainable by most techniques which are used for study of the defect solid state such as resistivity, Hall coefficient, thermal conductivity, specific heat, optical emission and absorption, etc., since these techniques essentially provide information on the transport properties of the material. The only technique providing comparable information on the defect environment is electron spin resonance.

The fact that the characteristic structure of Mössbauer spectra is only sensitive to the immediate environment of the emitting nucleus excludes observation of any radiation effects producing low defect concentrations unless the emitting nucleus itself is in the defect state. Thus, although the transport properties of materials may be drastically altered by charged particle, electron, gamma ray, or neutron irradiation, the characteristic Mössbauer pattern would probably be little changed due to the relatively low defect concentrations. Since time and intensity limitations usually exclude the possibility of high defect concentrations, the alternative is to use low defect concentrations in which the Mössbauer nucleus itself is introduced as the defect.

The neutron capture process offers such a possibility for simultaneously producing the Mössbauer parent nuclide and introducing it as a defect in the lattice. The displacement mechanism is the recoil of the nucleus due to the emission of prompt gamma rays following the neutron capture. This displacement mechanism also has the advantage that recoil energies are relatively low, so the resultant displaced atom configurations remain rather simple. In studying neutron capture induced recoil effects, it is desirable to produce a parent nuclide which is an isomeric state. This eliminates any complicating effects caused by the chemical change associated with beta decay. In some cases, the Mössbauer level itself is populated very shortly after the neutron capture so Mössbauer experiments must be performed with a neutron beam (e.g., $Fe^{56}(n,\gamma)Fe^{57m}$). In other cases, a long-lived metastable state precedes the Mössbauer level so that in-pile irradiation may be done first and the Mössbauer experiment may be conducted away from the reactor (e.g., $Te^{124}(n,\gamma)Te^{125m}(58d)$).

The effects of neutron capture induced recoils have been studied most extensively in semiconducting materials. This is due to the expanding use of semiconducting devices (i.e., transistors, diodes, thermoelectric elements, radiation detectors, etc.) in radiation environments (i.e., reactors, weapons systems, space, etc.). As mentioned earlier, most techniques used in studying the radiation effects involve measurement of transport properties. It was hoped that Mössbauer effect measurements would provide supplementary information on defect environments.

Te^{125} seemed to be one of the best Mössbauer nuclides for studying neutron capture effects. Previous studies of radiation effects in tellurium compounds have principally involved PbTe. This compound has received considerable attention because it is a good thermoelectric material and has potential application for energy conversion in radiation environments.

Mössbauer effect measurements of Te^{125} have been rather limited. Thus a great deal of valuable information is yet to be obtained from isomer shift and quadrupole splitting data in tellurium compounds

One of the most interesting and least explored areas of Mössbauer measurement in Te^{125} is in magnetic hyperfine structure. The magnetic compounds formed from tellurium and transition series metals offer an opportunity to measure transferred hyperfine fields at the nonmagnetic tellurium site. These measurements can provide information on both the excited state magnetic moment in Te^{125} and the internal magnetic field.

B. Literature Survey

1. Radiation Effect Measurements Using the Mössbauer Effect

A considerable number of papers have appeared the past few years which are concerned with the effect of nuclear reaction induced recoils on the Mössbauer spectrum. In one group of papers the impetus was the development of new techniques for populating Mössbauer parent nuclides. The methods employed include alpha decay,[1] Coulomb excitation,[2-5] nuclear reactions,[6-8] and thermal neutron activation.[9] The results

indicate that all of these processes can be used for source production without destroying the recoilless emission. However, in most cases the recoil effects due to the source production did alter the line intensity or line width to some degree.

A second group of papers, which we shall now discuss in more detail, is directly concerned with the use of the Mössbauer effect for lattice defect studies. The feasibility of using Mössbauer effect techniques for study of lattice defects was first proposed by Gonser and Wiedersich.[10] Dederichs, Lehmann, and Wegener[11] theoretically investigated the replacement probabilities for displaced atoms and proposed a Mössbauer experiment using Coulomb excitation in which the replacement probability could be measured. Belogurov,[12] in a comment to the paper by Dederichs, et al., proposed neutron capture gamma ray recoil as an alternative method for studying replacement collisions.

Fink and Kienle[13] have investigated the recoil effects following neutron capture in Gd^{155} and Gd^{157}. In a "mirror experiment" in which the spectrum for a Gd metal target and $Gd_2^{158}O_3$ absorber was compared to that for a $Gd_2^{157}O_3$ target and Gd metal absorber, the corrected area under the transmission line for the oxide target was only .6 that for the metal target. The line for the oxide target was also about 10 percent broader.

The Johns Hopkins group[14] has performed Coulomb excitation measurements in Fe_2O_3 and observed an f value a factor of two less than that for a normal Fe_2O_3 lattice. No changes were observed in the hyperfine splitting. The results can be

qualitatively explained on the basis of a dynamical model in which individual displacements occur but do not seem to be explainable on the basis of a localized heating or thermal spike model.

Effects of thermal neutron capture in Sn^{118} have been observed by Hannaford, Howard, and Wignall[15] in the Mössbauer spectrum of Mg_2SnO_4. The irradiation of Sn^{118} to produce the isomeric state Mössbauer parent Sn^{119m} produced a weak secondary line in the Mössbauer spectrum. The secondary line was removed by annealing in the temperature range 600-1000°C. The authors concluded that the secondary line was due to Sn atoms in the divalent state and that approximately 25 percent of the atoms have suffered the displacement induced valence change from four to two.

Neutron capture experiments in Fe^{56} by Obenshain and Berger[16] have given evidence of changes in the effective hyperfine field due to recoil effects. Using both Fe metal and Fe_2O_3 targets, the effective hyperfine fields were seen to increase in Fe metal and decrease in Fe_2O_3 with respect to the fields obtained using the same materials as absorbers.

In a very recent letter, Stepanov and Aleksandrov[17] report on the effects of neutron capture in Te^{124} on the Mössbauer spectrum for $PbTe^{125}$. After irradiating the $PbTe^{124}$ with 2.3×10^{14} neutrons/cm^2-sec for 45 days, the isomer shift was measured with respect to a PbTe absorber. Twenty days after the irradiation, the isomer shift was .2 cm/sec. The isomer shift then changed exponentially as a function of time with a

characteristic lifetime $\tau = 10 \pm 3$ days, eventually reaching the value 0.

The results of all Mössbauer measurements described above are summarized in Appendix A.

2. Neutron Capture Effects

Possibilities of neutron capture induced defects in silicon and germanium were first pointed out by Schweinler[18] in 1959. With average recoil energies of 780 ev in silicon and 180 ev in germanium, it was concluded that almost every neutron capture results in a displacement of the capturing nucleus.

Walker[19] noted that in a number of elements neutron capture induced defects can form a significant fraction of the total defects produced upon reactor irradiation.

Experimental evidence of the neutron capture induced defects in silicon and germanium has been shown by Crawford and Cleland.[20] Hall coefficient and resistivity measurements in silicon and germanium indicated approximately two and one electron removed respectively per thermal neutron captured. Annealing at 450°C in the germanium restored the displaced atoms to the normal lattice sites.

Neutron capture effects have been studied in the semiconductor CdS by Oswald and Kikuchi[21] and in CdS and CdTe by Barnes and Kikuchi.[22] The effects of the Cd^{114} recoil in CdS were studied using luminescence and conductivity measurements. Both properties changed drastically with thermal neutron irradiation and were restored with annealing at 500°C.

The thermal neutron effects in CdS were monitored by use of the Hall effect, electrical conductivity, and luminescence. The Hall coefficient and resistivity measurements in CdTe indicated one Cd vacancy and one Cd interstitial are introduced per thermal neutron absorbed. Annealing occurred between 160 and 200°C.

3. Radiation Effects in PbTe and Te Metal

a. PbTe

Since considerable interest has been shown in the use of the thermoelectric properties of PbTe for direct energy conversion, many measurements have been made of the effect of reactor neutrons on this material.

Danko, Kilp, and Mitchell[23] have investigated the changes in electrical resistivity and Seebeck coefficient in PbTe due to irradiation in a thermal neutron flux. The coefficients were first measured prior to the irradiation. The samples were then irradiated at reactor ambient temperature (50°C) with a dose of 1.5×10^{20} thermal neutrons and a similar number of fast neutrons. The measurements following the irradiation showed an increase in both the electrical resistivity and Seebeck coefficient. After annealing above 200°C both parameters returned to the preirradiation values.

The group at Knolls Atomic Power Laboratory has performed numerous measurements of the Hall coefficient, electrical resistivity, and Seebeck coefficient in both n- and p-type PbTe.[24,25] Irradiating with doses up to 5×10^{19} fast

(E > 1 Mev) neutrons/cm^2 and 6 x 10^{20} thermal neutrons/cm^2 at 60°C, both the Seebeck coefficient and resistivity showed an increase. From the Hall coefficient measurements, it was determined that the increase in Seebeck coefficient and resistivity could be attributed to a decrease in carrier concentration. Similar results obtained in comparison with cadmium shielded and unshielded specimens indicated most of the effect was due to the fast neutrons. Annealing experiments indicated recovery occurred in the range 100°C to 170°C and 140°C to 180°C for p- and n-type material respectively.

b. Te

Much less effort has been devoted to the study of radiation effects in tellurium. However, some measurements have been performed.

Samples of p-type tellurium were irradiated at 78°K with 25 Mev electrons by van Lint, Wikner, and Miller.[26] The irradiation caused an initial increase in conductivity due to the introduction of carriers. Annealing measurements indicated the defects introduced were stable at 78°K but were completely annealed out when the specimen was left at room temperature for several hours.

Similar increases in conductivity were obtained by irradiation of tellurium in neutron doses of 10^{13}/cm^2.[27] No annealing measurements were reported.

4. Mössbauer Effect Measurements Using Te^{125}

Mössbauer effect measurements using Te^{125} have been performed by several groups.

Resonance scattering studies were performed in Te^{125m} by Hien, Shapiro, and Shpinel[28] in 1962. Using a source of neutron irradiated $Te^{124}O_2$ at both liquid nitrogen temperature and room temperature and an absorber of $Te^{125}O_2$ at room temperature, values of the recoil-free fraction were obtained. At liquid nitrogen temperature $f=.12 \pm .03$ and at room temperature $f=.067 \pm .008$. No apparent quadrupole splitting was observed for the TeO_2. No effect was observed for Te^{125} metal at room temperature.

The most extensive study of the Te^{125} Mössbauer resonance has been done by the group at Lawrence Radiation Laboratory.[29-31] Measurements were performed using sources of I^{125} in $NaIO_3$ which exhibited four resonance lines and I^{125} in a Cu host lattice which had a single line emission spectrum. Absorbers studied include ZnTe, MnTe, β-FeTe, TeF_4, TeI_4, TeO_2, Na_2TeO_4, and Te metal. Measurements were made at liquid nitrogen temperature. The quadrupole splitting in Te metal was observed to be $7.6 \pm .2$ mm/sec.* A calculation of the electric field gradient using a molecular orbital model[30] for Te yielded $eq=-2.8 \pm^{.3}_{.4} \times 10^{16}$ esu. The resultant quadrupole moment was then $|Q|=.20 \pm^{.03}_{.02}$ barns. This was in good agreement with a configuration-mixing calculation which gave $Q=-.23$ barns.[32]

*For the 35.6 kev gamma ray resonance in Te^{125}, 1 mm/sec = 1.19×10^{-7} ev. (See Equation (III.1).)

Violet, et al.,[31] did not observe quadrupole splitting in cubic ZnTe, in the Cu host lattice source, or in hexagonal NiTe. Quadrupole splittings reported for MnTe, β-FeTe, α-TeO_2, TeF_4, and TeI_4 are respectively 3 ± 1, 3 ± 1, $7.3 \pm .1$, 7 ± 1, and 6 ± 1 mm/sec.

Violet, et al., attributed the existence of four lines in the emission spectrum of the $NaIO_3$ source to the presence of two charge states.[31] This may result from the K x-ray and Auger transitions following the I^{125} decay. In the model proposed, the higher charge state decays to the lower charge state by electron capture with a half life of $\approx 1.6 \times 10^{-9}$ sec.

Shikazono[33] has reported observation of the Mössbauer effect in several compounds of Te^{125}. From the observed quadrupole splitting of 7 mm/sec in Te metal an electric field gradient calculation yielded an excited state quadrupole moment $|Q| = .17$ barns. The α-TeO_2 spectrum had an identical quadrupole splitting of 7 mm/sec. No quadrupole splitting was observed in MnTe; the lack of splitting was attributed to the ionic structure of this compound. A broadened single line spectrum observed for CrTe was attributed to an unresolved magnetic hyperfine splitting. An estimate of the excited state nuclear moment $\mu_e \simeq .7$ nm led to an upper limit for the internal field at the Te nucleus in CrTe of 50 kgauss. A source of Sb^{125} imbedded in an iron lattice produced a partially resolved magnetic hyperfine splitting with internal field ~600 kgauss.

Using both a source and absorber of Te metal, the Debye temperature Θ_D=125 ± 5° has been determined for Te metal by Frankel, Barrett, and Shirley.[34,35] The measured quadrupole splitting was 7.7 mm/sec.

Buyrn and Grodzins[32] measured quadrupole splittings in Te, TeO_2, Na_2TeO_4, and NiTe of 7.5 mm/sec, 7.0 mm/sec, 7.0 mm/sec, 0, and 0 respectively. The isomer shifts relative to Te for the latter three compounds were 0, -1.5, and -1.0 mm/sec with error ± .1 mm/sec. Debye temperatures for Te, TeO_2, and Na_2TeO_4 were estimated as 125°K, 170°K, and 190°K.

Stepanov, et al.,[36] observed Te^{125} Mössbauer resonances in PbTe, Te metal, "amorphous" Te, and TeO_2. The quadrupole splitting for Te metal was reported as 7.8 mm/sec. The TeO_2 spectrum consisted of four lines with splittings 5.5 mm/sec and 10.1 mm/sec which were attributed to the presence of both the tetragonal and orthorhombic crystal modifications of TeO_2.

Magnetic hyperfine structure has been measured for Te^{125} by Frankel, et al.,[37] using an Sb^{125} source in both Fe and Ni hosts. The hyperfine pattern measured against a single line ZnTe absorber showed a partially resolved hyperfine structure with the pattern 3:2:1:1:2:3. This established the excited state moment μ_e as positive.

CHAPTER II.

BACKGROUND

A. Selection of Suitable Mössbauer Nuclide for Studies of Neutron Capture Effects

Several factors were considered in selecting a suitable Mössbauer nuclide for studies of neutron capture effects. The principal factor in the selection was the desire for a Mössbauer parent which was an isomer of the Mössbauer level. This is necessitated by the fact that any non-isomeric parent will be a chemical impurity in the host lattice (e.g., Fe^{57} populated by the electron capture decay of Co^{57}). Use of an isomeric state parent eliminates any effects the chemical impurity could have on the Mössbauer spectrum. This includes changes in the recoil-free fraction attributable to localized lattice modes introduced by the impurity and changes in the isomer shift and quadrupole splitting arising from the electronic rearrangement associated with the decay. In all likelihood these effects are small. The mass difference between the impurity and host would be only 1 amu. Electronic relaxation times are usually fast ($\sim 10^{-10}$ sec) compared to the lifetime of the Mössbauer level; however, metastable charge states may be produced. Nevertheless, to avoid any possible effects, it appeared best to use an isomeric state parent.

A second consideration was that the Mössbauer effect should have been observed previously so that: 1) there was some guarantee of obtaining a spectrum, and 2) the relevant

parameters were known. From the list of nuclides for which the Mössbauer effect has been observed,[38] those listed in Table II-1 can be populated from an isomeric state. Also included in the table are the thermal neutron activation cross section,[39] the half life of the isomeric state, and the binding energy of the neutron in the product nucleus.[40] The relevant Mössbauer parameters, including the lifetime and energy of the Mössbauer level,[38] are also given.

The criteria used in selection of the nuclide most suitable for radiation effect measurements are: 1) the Mössbauer parent must have a reasonably long half life so that Mössbauer measurement, annealing, and remeasurement can be performed; 2) the thermal neutron activation cross section must be sufficient so that sources can be activated within a reasonable length of time; 3) the recoil-free fraction should be as large as possible (implies a low lying energy level, large mass number, and chemical compounds with a high Debye temperature); and 4) the resonance line width should be sufficiently narrow to resolve hyperfine structure (implies a long lifetime for the Mössbauer level).

On the basis of these considerations, Te^{125} provides the best compromise of the conditions. The only unsatisfactory parameter for Te^{125} is the rather short lifetime ($T_{\frac{1}{2}} = 1.4 \times 10^{-9}$ sec) of the Mössbauer level. The natural line width ($\Gamma = 2.744$ mm/sec) is quite broad and makes resolution of hyperfine structure somewhat difficult.

TABLE II-1

RELEVANT PARAMETERS FOR MÖSSBAUER NUCLIDES WITH ISOMERIC STATE PARENTS POPULATED BY AN (n,γ) REACTION

Stable Isotope	σ(n,γ) Barns	Binding* Energy Mev	Mössbauer Parent	$T_{1/2}$ for Parent	Mössbauer Level E_o kev	Mössbauer Level $T_{1/2}$ Sec
Ge^{72}	.94 ± .09	6.4	Ge^{73m}	.53s	13.5	4.0×10^{-6}
Kr^{82}	45 ± 15	7.5	Kr^{83m}	1.86h	9.3	1.47×10^{-7}
Sn^{118}	10 ± 6mb	6.54	Sn^{119m}	245d	23.8	1.85×10^{-8}
Te^{124}	40 ± 25mb	6.48	Te^{125m}	58d	35.6	1.4×10^{-9}
Xe^{128}	< 5	7.1	Xe^{129m}	8d	40	9.6×10^{-10}
Xe^{130}	< 5	6.60	Xe^{131m}	12d	80.2	5.0×10^{-10}
W^{182}	19 ± 2	6.29	W^{183m}	5.5s	46.5 99.1	1.5×10^{-10} 5.2×10^{-10}
Pt^{194}	1.2 ± .9	6.09	Pt^{195m}	4.1d	98.9 129.7	1.7×10^{-10} 5.5×10^{-10}

*Binding energy of the neutron in the product nucleus.

In retrospect, the Sn^{119} probably would have been a better choice of nuclides. At the time of selection the Te^{124} activation cross section was listed as 5 ± 3 barns rather than the more recently tabulated 40 ± 25 millibarns.[39] The two orders of magnitude larger cross section for Te^{124} then seemed to outweight the order of magnitude decrease in line width for Sn^{119}. Only after we had become seriously involved in Te^{125} measurements did we find that the Te^{124} activation cross section was in error and the broad lines of Te^{125} were a handicap in resolving hyperfine structure.

B. Thermal and Fast Neutron Effects in Tellurium Compounds

1. Thermal Neutrons

The Mossbauer isomeric state parent Te^{125m} is produced by thermal neutron capture in Te^{124}, described by

$$Te^{124} + n \longrightarrow Te^{125*} \longrightarrow Te^{125m} + \gamma\text{-rays} \quad . \qquad \text{(II.1)}$$

Intrinsic defects can be introduced in the solid if the recoil energy of the Te^{125m} nucleus is greater than the minimum energy for displacement. The recoil energy arises from the conservation of momentum following the emission of the prompt gamma rays. The process is depicted in Figure II-1 for the emission of a single gamma ray. By conservation of momentum, the recoil energy E_R is given by

$$E_R = \frac{E_\gamma^2}{2Mc^2} \quad , \qquad \text{(II.2)}$$

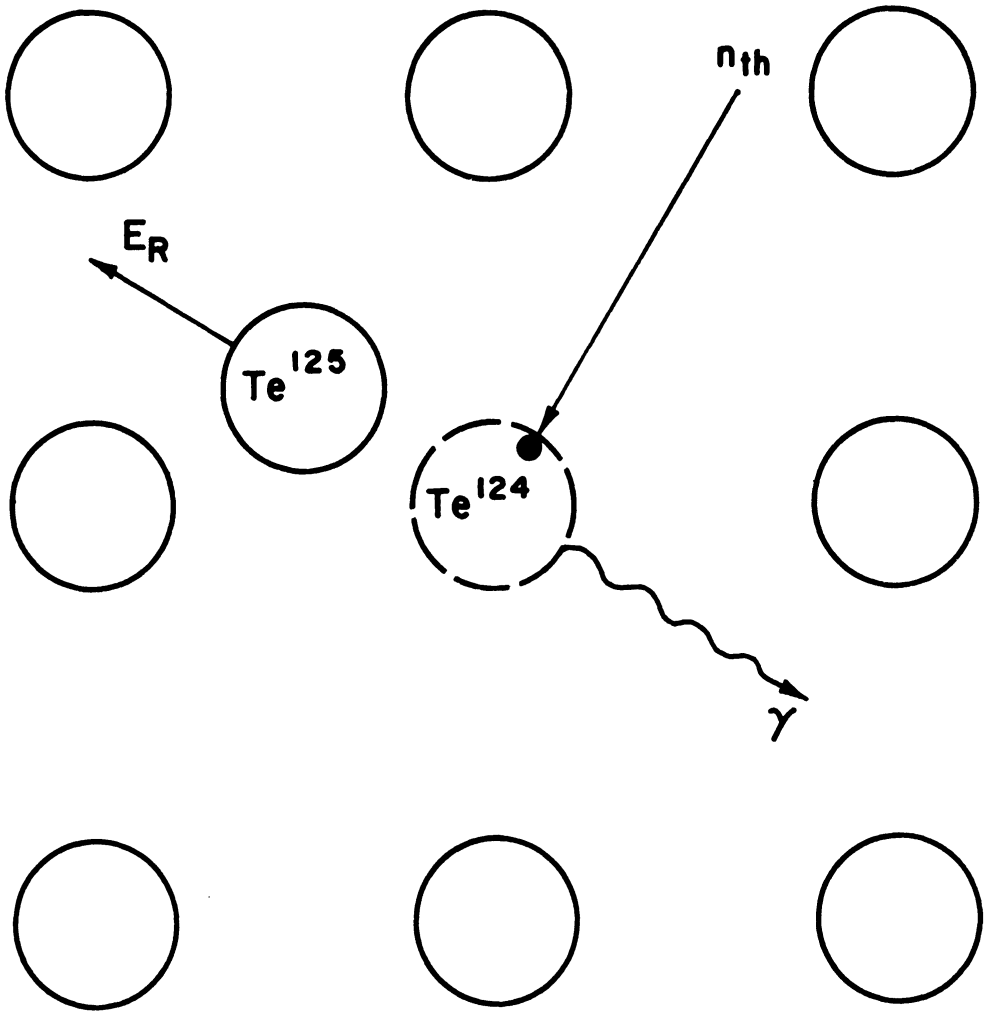

FIGURE II-1

DIAGRAM OF $Te^{124}(n,\gamma)$ Te^{125}
RECOIL MECHANISM

where E_γ is the gamma ray energy, M the nuclear mass, and c the speed of light. Evaluating Equation (II.2) numerically for Te^{125} with a gamma ray energy of 6.37 Mev, $E_R \simeq 174$ ev.

However, the decay of the highly excited state does not usually proceed by the emission of a single gamma ray, but rather a cascade of gamma rays emitted in transitions between various nuclear excited levels. If it is assumed that the gamma rays are emitted randomly and isotropically, Schweinler[41] has shown that the mean recoil energy $\langle E_R \rangle$ is just equal to the sum of the recoil energies due to the individual gamma rays, or

$$\langle E_R \rangle = \sum_i \frac{E_{\gamma_i}^2}{2Mc^2} \quad . \tag{II.3}$$

Unfortunately, the spectrum of neutron capture gamma rays has not been experimentally measured for Te^{125}. Thus the mean recoil energy for Te^{125} can only be estimated. In the study of neutron capture effects in germanium, Crawford and Cleland[20] estimated the recoil energy assuming that after neutron capture in the even-even isotopes two photons of equal energy were emitted and in the even-odd isotopes four photons of equal energy were emitted. Assuming that two photons of equal energy are emitted for neutron capture in Te^{124}, the mean recoil energy obtained from Equation (II.3) is $\langle E_R \rangle = 87$ ev. This estimate may be somewhat high in consideration of data on neutron capture in other even-even nuclides.[40] Most exhibit maxima in the energy distribution curve of gamma rays emitted in the range 2-2.5 Mev. This would indicate that

perhaps an assumption of three equal energy gamma rays would be more realistic. Based on this assumption, the resultant mean recoil energy is $\langle E_R \rangle = 58$ ev.

In the measurement by Muehlhause[97] of the mean number of prompt gamma rays emitted for a series of elements, the number increased with increasing mass. Judging from his results, an estimate of three gamma rays does not appear unreasonable for Te^{125}.

An estimate of the average number of displacements produced per thermal neutron captured can be obtained using simple radiation damage theory. The average number of displacements, $\bar{\nu}$, is given by[42]

$$\bar{\nu} = \begin{cases} 0 & \langle E_R \rangle < E_d \\ 1 & E_d \leq \langle E_R \rangle \leq 2E_d \\ \dfrac{\langle E_R \rangle}{2E_d} & 2E_d \leq \langle E_R \rangle \leq E_i \\ \dfrac{E_i}{2E_d} & E_i < \langle E_R \rangle \end{cases} , \qquad \text{(II.4)}$$

where E_d is the threshold energy for displacement and E_i is the ionization cut-off energy.

If it is assumed that the threshold energy for displacement in tellurium compounds $E_d = 25$ ev and $\langle E_R \rangle = 58$ ev, the average number of displacements $\bar{\nu} = 1.16$. This means that on the average we can expect only one displacement per thermal neutron captured, the Te^{125} nucleus itself.

2. Fast Neutrons

Since all source irradiations were done in or near the core of the Ford Nuclear Reactor (FNR), it is necessary to consider the effects of the fairly significant fast neutron flux on the tellurium compounds. Since the cross section for thermal neutron capture in Te^{124} (40 millibarns[39]) is fairly small, the number of fast neutron induced displacements may be considerably larger than those produced by thermal neutron capture. However, as discussed in Chapter I, the fast neutron induced displacements may still have little effect on the Mössbauer spectra due to the relatively low concentration of defects and the small probability of their being near the Mössbauer emitting nucleus. We will consider the effects of the fast neutrons in PbTe, Te metal, and TeO_2.

The displacements are created by the scattering of a high energy neutron from a lattice atom. The primary recoiling atom creates additional displacements as it dissipates its energy in the lattice. The number of displacements produced by a fast neutron flux can be estimated using simple radiation damage theory.

In an elastic collision, the maximum energy of the primary recoiling atom is[43]

$$E_p\,(max) = \frac{4Mm}{(M+m)^2}\,E_n \quad , \qquad \text{(II.5)}$$

where M and m are the mass of the atom and neutron respectively, and E_n is the neutron energy. For target atoms where $M \gg m$, Equation (II.5) can be approximated by

$$E_p(max) \simeq \frac{4E_n}{A} \quad , \tag{II.6}$$

where A is the ratio of the target atomic mass to the neutron mass. If the scattering is isotropic in the center of mass coordinate system, the mean energy of the primary recoiling atom is[42]

$$\bar{E}_p = \frac{E_p(max)}{2} \quad . \tag{II.7}$$

Combining Equations (II.7) and (II.5) together with a correction factor, f',

$$\bar{E}_p = f' \frac{2Mm}{(M+m)^2} E_n \quad , \tag{II.8}$$

where f' is a factor correcting for anisotropy and inelasticity in fast neutron scattering.[43]

The average number of displacements produced per primary recoil atom can be determined using Equation (II.4) where $\bar{E}_p$ replaces $\langle E_R \rangle$. However, it is first necessary to determine whether $\bar{E}_p$ is less than the ionization energy E_i. Seitz[44] has shown that E_i can be estimated as

$$E_i = \frac{1}{8}\left(\frac{M}{m_e}\right) E_g \quad , \tag{II.9}$$

where M and m_e are the mass of the primary recoiling atom and electron respectively and E_g is the lowest electronic excitation energy.

The total number of fast neutron displacements produced per unit volume in the material is given by

$$I = \nu_f \sum_s^f \varphi_f t \quad , \qquad \text{(II.10)}$$

where ν_f is the mean number of displacements per fast neutron scattered, $\sum_s^f$ is the macroscopic fast neutron scattering cross section, φ_f is the fast neutron flux, and t is the irradiation time.

The foregoing parameters were evaluated for the source materials PbTe, Te, and TeO_2. The results are shown in Table II-2. $\bar{E}_p$ is calculated from Equation (II.8) for each of the elements assuming an average fast neutron energy $\bar{E}_n \simeq 1$ Mev and a nominal value of $f' \simeq 2/3$.[43] The band gap energies in PbTe, Te, and TeO_2 are respectively E_g=.31 ev, E_g=.34 ev, and E_g=1.5 ev.[45] The respective ionization energies are calculated from Equation (II.9). Again assuming E_d=25 ev, the average number of displacements produced by each primary recoiling atom, ν_f, can be determined from Equation (II.4).

The macroscopic fast neutron scattering cross sections[39] are also listed in Table II-2. Values of the integrated flux ($\varphi_f t$) are obtained from Table III-2 for each of the sources. The total number of fast neutron displacements produced per unit volume is calculated for each element using Equation (II.10).

TABLE II-2

PARAMETERS RELATING TO FAST NEUTRON INDUCED DISPLACEMENTS IN TELLURIUM SOURCE MATERIALS

Compound	Element	$\bar{E}_p$ (kev)	E_g (ev)	E_i (kev)	ν_f	Σ_s^f (cm^{-1})	$\varphi_f t$ (n/cm^2)	I (defects/cm^3)
PbTe	Pb	6	.31	14.6	120	.088	6.4×10^{16}	6.8×10^{17}
	Te	11		8.8	176	.094		1.1×10^{18}
Te	Te	11	.34	9.6	192	.194	7.6×10^{16}	2.8×10^{18}
TeO_2	Te	11	1.5	42.4	220	.137	6.5×10^{17}	2.0×10^{19}
	O	83		5.5	110	.150		1.1×10^{19}

(Continued)

Compound	I_{tot} (defects/cm^3)	N (atoms Te/cm^3)	I_{tot}/N (defects/atom Te)
PbTe	1.8×10^{18}	1.5×10^{22}	1.2×10^{-4}
Te	2.8×10^{18}	2.9×10^{22}	9.7×10^{-5}
TeO_2	3.1×10^{19}	2.1×10^{22}	1.5×10^{-3}

The total number of defects per unit volume for each compound is compared to the density of tellurium atoms per unit volume, $N = \rho \frac{N_o}{A}$.

For each of the source materials, the concentration of fast neutron induced displacements is only $\sim 10^{-4}$-10^{-3} of the concentration of tellurium atoms. Hence, on the average, the displaced atoms will be separated by approximately ten lattice spacings. The probability of such widely spread displaced atoms being in the immediate environment (nearest or next-nearest neighbor) of a Mössbauer emitting nucleus is very small.

C. Characteristics of Mössbauer Spectra in Te^{125}

1. Decay Scheme of Te^{125m}

The decay scheme for Te^{125m} is shown in Figure II-2. The 145 kev isomeric state decays to the 35.6 kev level with the emission of a 109.4 kev gamma ray (γ_1). The 35.6 kev Mössbauer level has a half life $T_{\frac{1}{2}} = 1.4 \times 10^{-9}$s and decays to the ground state by the emission of a 35.6 kev gamma ray (γ_M). The decay from the 58 d state is highly converted with internal conversion coefficient $\alpha_K = 160$.[47] The ratio of conversion coefficients is K:L:M:N = 54:36:8.3:1.7 and $L_I:L_{II}:L_{III}$ = 0.66:0.30:1. The internal conversion coefficient for the decay from the 35.6 kev level is $\alpha_K = 11.4$.[47] The ratio of conversion coefficients is K:L:M:N = 80:11:1.7:0.3.

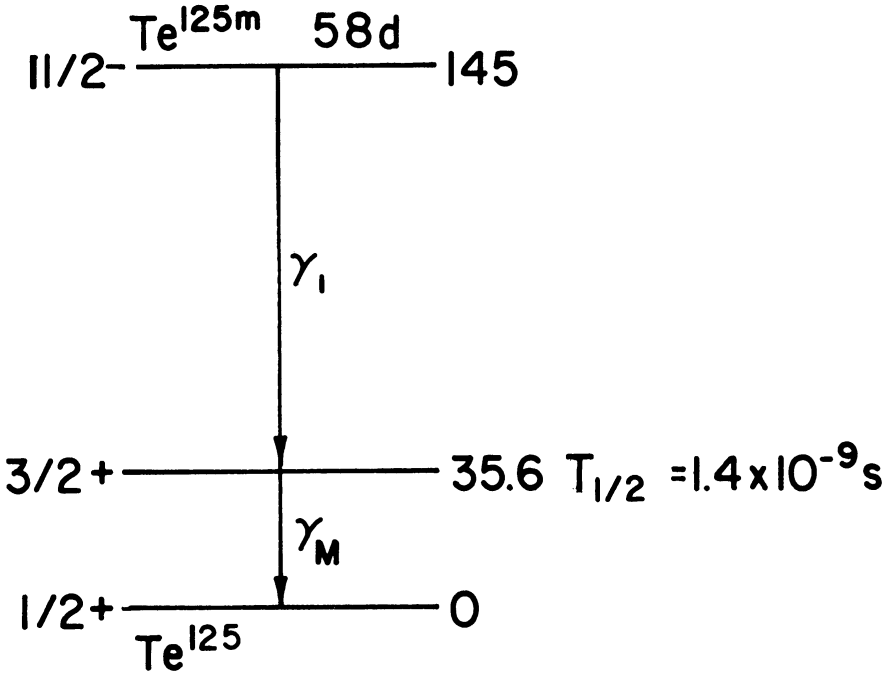

FIGURE II-2

Te^{125m} DECAY SCHEME

One of the difficulties in using the 35.6 kev gamma ray from Te^{125} for Mössbauer measurements lies in the discrimination of the gamma ray from the x-ray background. The relative locations of the gamma ray and x-ray energies are shown in Figure II-3. The x-ray energies are K_{α_1} = 27.47 kev, K_{α_2} = 27.20 kev, K'_{β_1} = 31.06 kev, and K'_{β_2} = 31.71 kev.

FIGURE II-3

RELATIVE LOCATION OF X-RAY AND GAMMA RAY ENERGIES IN DECAY OF Te^{125m}

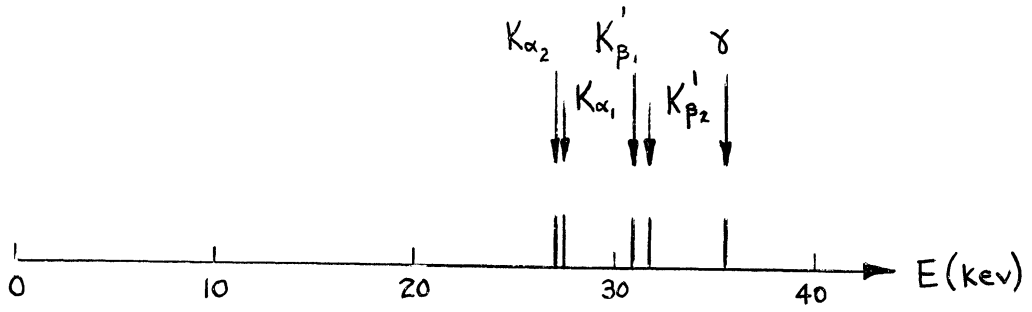

Not only are the x-ray energies very close to the gamma ray energy, but the x-ray intensities are much greater. The relative intensity of the 35.6 kev gamma ray and the tellurium x-rays can be calculated using the internal conversion coefficients. The total internal conversion coefficient is just the sum of partial coefficients, so α = 296.2 and α = 13.25 for transitions γ_1 and γ_M respectively. The relative intensities of the K_α and K_β components of the x-rays emitted can easily be calculated[48] and $K_\alpha : K_\beta$ = .823:.177. Using these values and the K-shell fluorescent yield ω_K = .855,[48]

the yield of K_α and K_β x-rays and 35.6 kev gamma rays per decay of the 145 kev excited state are $K_\alpha : K_\beta : \gamma = .942 : .203 : .070$. The weighted average of the components of the K_α and K_β x-ray lines yields x-ray energies $\bar{E}_{K_\alpha} = 27.4$ kev and $\bar{E}_{K_\beta} = 31.2$ kev.

2. Mössbauer Recoilless Fraction

The Mössbauer effect is the recoilless resonant emission and absorption of gamma rays by nuclei. Resonance occurs if a gamma ray emitted by a nucleus in decaying from an excited state to the ground state is then absorbed by an identical nucleus which is excited from the ground state to the excited state.

For a free nucleus, the recoil energy loss will usually prevent the resonance process. For a nuclear transition energy E_o, the gamma ray energy E_γ will be

$$E_\gamma = E_o - E_R \quad , \tag{II.11}$$

where the recoil energy E_R is given by the expression described earlier in Equation (II.2), or

$$E_R = \frac{E_\gamma^2}{2Mc^2} \simeq \frac{E_o^2}{2Mc^2} \quad . \tag{II.12}$$

M is the mass of the nucleus after emission and c is the speed of light. Since approximately the same recoil energy is given up to the absorbing nucleus, the gamma ray emission spectrum and absorption cross section will be separated in energy by $2E_R$.

Due to the finite lifetime of the nuclear excited state, the energy level has a Lorentzian distribution of energies described by a line width

$$\Gamma = \hbar/\tau \qquad \text{(II.13)}$$

where τ is the mean lifetime of the state. For Te^{125}, E_R = 5.44×10^{-3} ev and $\Gamma = 3.27 \times 10^{-7}$ ev so $E_R \gg \Gamma$ and negligible resonant absorption will occur for emission by the free nucleus.

Mössbauer discovered[98] that for nuclei bound in a solid, there are conditions for which a fraction, f, of the gamma rays are emitted or absorbed without recoil loss. In such a case, the recoil momentum is imparted to the entire crystal rather than an individual nucleus. The gamma ray then has the full transition energy or $E_\gamma = E_o$. For such "recoilless" emission and absorption, the resonance process can occur.

The recoilless fraction, which is variously referred to as the f value or recoil-free fraction, has been discussed in innumerable papers. Assuming a Debye model for the case of an infinite crystal lattice, the recoilless fraction can be expressed as[99]

$$f = e^{-2W} \quad , \qquad \text{(II.14)}$$

where the Debye-Waller factor W is given by

$$W = \frac{3E_R}{k\Theta_D}\left[\frac{1}{4} + \left(\frac{T}{\Theta_D}\right)^2 \int_0^{\Theta_D/T} \frac{x\,dx}{e^x - 1}\right] \quad . \qquad \text{(II.15)}$$

In this expression E_R is the recoil energy for the free nucleus, T is the ambient temperature of the source or absorber, and Θ_D is the Debye temperature.

It is readily apparent from Equations (II.14) and (II.15) that in order to obtain a significant recoilless fraction f, $k\Theta_D$ must be greater than E_R and T must be less than Θ_D. Θ_D is of the order of 150°K in most tellurium compounds. In tellurium compounds, then, $k\Theta_D \simeq 13 \times 10^{-3}$ ev, which satisfies the first condition since $k\Theta_D > E_R$. To satisfy the second condition requires temperatures $T < 150^{\circ}K$--or temperature of the order of liquid nitrogen temperature or lower.

It must be kept in mind that the Debye model is only an approximation to the real lattice frequency spectrum. In fact, for anything but a monatomic lattice the use of the Debye model is questionable. The use of an "effective" Debye temperature, however, has proven adequate in characterizing Mössbauer recoil-free fractions. In general, though, Debye temperatures obtained from Mössbauer effect measurements do not agree with Debye temperatures obtained from specific heat measurement, etc. The difference arises in the different sensitivity to the shape of the real lattice frequency spectrum.

3. Mössbauer Hyperfine Structure

The Mössbauer spectrum can display either individually or in combination the isomer shift, electric quadrupole splitting, and magnetic hyperfine splitting. The following is a description of the interactions leading to these phenomena.

a. Isomer Shift

The isomer shift arises from the change in electrostatic interaction between the nuclear charge and the s-electron charge density caused by a difference in the nuclear radius between the excited and ground states. A non-relativistic perturbation calculation yields an energy difference between the source and absorber of[49]

$$\delta = \frac{2}{3}\pi Z e^2\left[\langle R^2\rangle_e - \langle R^2\rangle_g\right]\left[\left|\psi_s(0)\right|_a^2 - \left|\psi_s(0)\right|_s^2\right] \quad , \qquad \text{(II.16)}$$

where $\langle R^2\rangle_e$ and $\langle R^2\rangle_g$ are the mean square radii of the nucleus in the excited and ground state, respectively, and $\left|\psi_s(0)\right|_a^2$ and $\left|\psi_s(0)\right|_s^2$ are the s-electron densities at the nucleus in the absorber and source, respectively. Assuming the nuclear charge distribution has a constant value out to radius R, the isomer shift can be rewritten as

$$\delta = \frac{4\pi}{5} Z e^2 R^2\left[\left|\psi_s(0)\right|_a^2 - \left|\psi_s(0)\right|_s^2\right]\left(\delta R/R\right) \quad , \qquad \text{(II.17)}$$

where

$$\delta R = R_e - R_g \quad \text{and} \quad R = \frac{R_e + R_g}{2} \quad .$$

In heavier elements, relativistic effects become important.[51] These relativistic effects can be accounted for by multiplying Equation (II.17) by a correction factor S'(Z), which for tellurium is S'=2.44.

The isomer shift is measured by determining the shift of the centroid of the Mössbauer spectrum with respect to zero velocity. It is difficult to obtain information on s-electron densities from a single isomer shift since both source and absorber s-electron densities are included. However, by measuring relative shifts for a series of compounds with respect to a standard source or absorber, the change in s-electron density can be determined.

Tellurium has a wide range of valence states in different compounds. These should provide measurable changes in the s-electron density. Ionic tellurium configurations range from Te^{2-} with the electronic configuration $(KLM)4s^24p^64d^{10}5s^25p^6$ and filled 5s and 5p shells to Te^{6+} with a bare 5s and 5p shell. Metallic tellurium with configuration $5s^25p^4$ and Te^{4+} with configuration $5s^25p^0$ both have filled 5s shells, but differ in 5p shell filling. In purely ionic configurations, there should be an obvious difference in s-electron densities between the Te^{6+} with an empty 5s shell and the ions with a filled 5s shell. Different s-electron densities can also be expected between ions with filled 5s shells. Here the different s-electron densities arise due to variations in shielding of the 5s electrons by the differing numbers of 5p electrons. In 6s electrons, it has been estimated that this shielding effect is $\sim$10 percent for 6p electrons shielding 6s electrons.[52]

Covalent bonding can also provide intermediate conditions since both 5s and 5p electrons are involved in the bonding

orbitals. Covalency results in the delocalization of the 5s and 5p electrons associated with the ionic configurations. Such effects can be directly reflected through variations of the 5s electron density or in variations in 5p shielding. Interpretation of isomer shifts in the covalent compounds is much more difficult than in ionic compounds, however, since rigorous theoretical treatment of the molecular orbitals has been done in only relatively few cases.

Knowledge of the variation in isomer shift with variation in s-electron density can provide information on the change in nuclear radius between the excited and ground states. Shirley[51] has estimated $\delta R/R$ in Te^{125} from the experiments which have been performed. Using the shift of -1.5 mm/sec obtained by Buyrn and Grodzins[32] for a tellurium source versus a tellurate absorber, the value $\delta R/R \approx +0.7 \times 10^{-4}$ was obtained assuming the environments differed by one 5s electron. This numerical value for $\delta R/R$ should only be taken as a rough estimate since other calculations by Shirley yield values differing by an order of magnitude. The sign of $\delta R/R$ definitely appears to be positive, however.

b. Quadrupole Splitting

Electric quadrupole splitting arises from the interaction between the nuclear quadrupole moment and the electric field gradient created by the electronic environment of the nucleus. The Hamiltonian for the interaction can be written as[50]

$$\mathcal{H}_Q = \frac{e^2qQ}{4I(2I-1)}\left[3I_z^2 - I(I+1) + \eta/2\,(I_+^2 + I_-^2)\right] \quad , \qquad \text{(II.18)}$$

where Q is the electric quadrupole moment, eq = V_{zz} is the z component of the electric field gradient in the crystal principal axis system, $\eta = \frac{V_{xx} - V_{yy}}{V_{zz}}$ is the asymmetry parameter, and I_z, I_+, and I_- are the spin projection and raising and lowering operators respectively.

The ground state in Te^{125} has no quadrupole moment since $I_g = \frac{1}{2}$.[53] The eigenvalues of H_Q for the excited state with spin I = 3/2 are

$$E_m = \frac{e^2qQ}{4I(2I-1)}\left[3m^2 - I(I+1)\right]\left(1 + \eta^2/3\right)^{1/2} \quad . \qquad \text{(II.19)}$$

Hence the electric quadrupole interaction partially removes the spin degeneracy of the excited state, splitting it into two levels (|m| = 1/2, 3/2). In this case, the transitions between the excited and the ground states give rise to a two-line Mössbauer pattern with quadrupole splitting

$$\Delta E_Q = E_{3/2} - E_{1/2} = \frac{e^2qQ}{2}\left(1 + \eta^2/3\right)^{1/2} \quad . \qquad \text{(II.20)}$$

The quadrupole moment for the excited state obtained by Violet, Booth, and Wooten[30] from quadrupole splitting in Te metal is $|Q| = .20\ ^{+.03}_{-.02}$ barns. The configuration-mixing calculation result is Q = -.23 barns.[32]

Using the value $|Q| = .2$ barns for the excited state moment, it is possible from measurements to determine the crystalline electric field gradient. The electric field gradient arises from two sources, eq^c due to electrons inside the central cell surrounding the nucleus and eq^l due to all electrons and nuclei surrounding the cell in the rest of the lattice. The resultant field gradient is

$$eq = eq^{\ell}(1-\gamma_\infty) + eq^{c}(1-R) \quad , \tag{II.21}$$

where γ_∞ and R are Sternheimer polarization factors. The polarization factors account for the polarization of the closed electron shells by the lattice and cell electrons, respectively, and the resulting induced field gradient.

In purely ionic configurations Te^{2-}, Te^{4+}, and Te^{6+}, there should be no contribution eq^c since the 5p shell is either filled or empty. If the lattice structure has cubic symmetry, eq^l is also zero since $\eta = 0$ and $V_{zz} = 0$ for cubic symmetry. For lower symmetry, there should be a contribution eq^l. Evaluation of eq^l does not require precise knowledge of the electron wave functions and may be considered in a first approximation by assuming the lattice as an assembly of point charges. For a crystal structure with axial symmetry, $\eta = 0$, and the field gradient tensor is reduced to $eq^l = V_{zz}$ where[54]

$$eq^{\ell} = \int \rho(\underline{r}) \frac{3z^2 - r^2}{r^5} d^3r \tag{II.22}$$

$$eq^{l} = 2\int \rho(\underline{r}) \frac{P_2(\cos\theta)}{r^3} d^3r \quad . \tag{II.23}$$

Assuming a point charge distribution, the integral reduces to a lattice sum

$$eq^{l} = 2\sum_{j} e_j \frac{P_2(\cos\theta_j)}{r_j^3} \quad . \tag{II.24}$$

In general, eq^1 will be small compared to eq^c due to the $1/r^3$ dependence. However, the polarization factor γ_∞ may be very large for heavier ions,[55] providing a significant enhancement of eq^1.

In covalently bonded tellurium compounds, the dominant contribution to eq comes from eq^c. Evaluation of eq^c requires rather precise knowledge of the electron wave functions. eq^c arises principally from the valence p-electrons and knowledge of these wave functions requires a molecular orbital calculation for the solid. Needless to say, such calculations have been done for only a limited number of cases.

c. Magnetic Hyperfine Splitting

Magnetic hyperfine splitting arises from the interaction of the nuclear magnetic moment with the magnetic field at the nucleus. In the absence of an applied magnetic field, the magnetic field is solely the internal magnetic field arising

from the electrons. The Hamiltonian for the interaction can be written as[50]

$$\mathcal{H}_D = -\mu \cdot \underline{H}_{eff} \quad , \tag{II.25}$$

where μ is the nuclear magnetic moment and H_{eff} is the effective internal magnetic field.

Magnetic hyperfine splitting can occur in both the excited and ground states in Te^{125} as shown in Figure II-4. The energy eigenvalues of H_D are

$$E_m = -\frac{\mu H_{eff} m}{I} \quad . \tag{II.26}$$

The magnetic hyperfine interaction completely removes the spin degeneracy of each of the states.

The 35.6 kev gamma ray transition is predominantly a magnetic dipole (M1) transition with only a .035 percent[56] admixture of electric quadrupole (E2) radiation. The selection rule for magnetic dipole transitions is $\Delta m = 0, \pm 1$, implying that six transitions between the excited and ground states are allowed. These are shown in Figure II-4.

The relative location of each of the six component lines is completely determined by the ratio g_e/g_g where g_e and g_g are the excited and ground state g factors ($g = \mu/I$). All the possible absorption patterns can be described by a "g-factor diagram" as shown in Figure II-5. For a given g-factor ratio, the magnetic hyperfine spectrum is obtained by drawing a horizontal

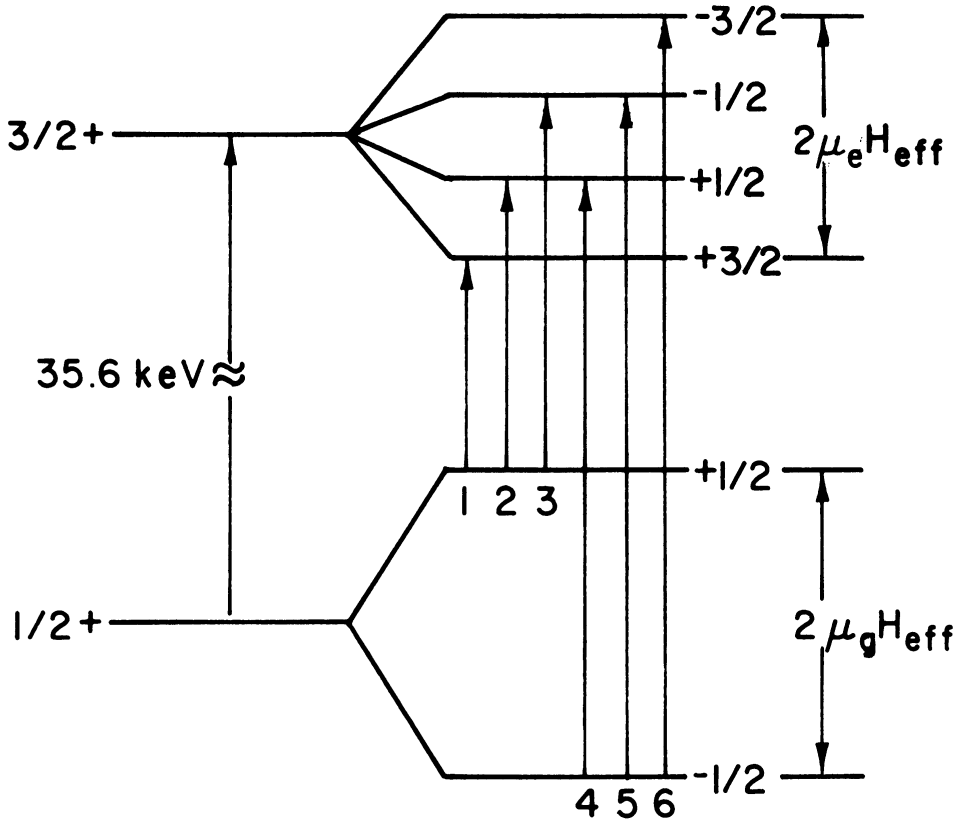

FIGURE II-4

MAGNETIC HYPERFINE SPLITTING OF THE 3/2 + AND 1/2 + STATES OF Te^{125}

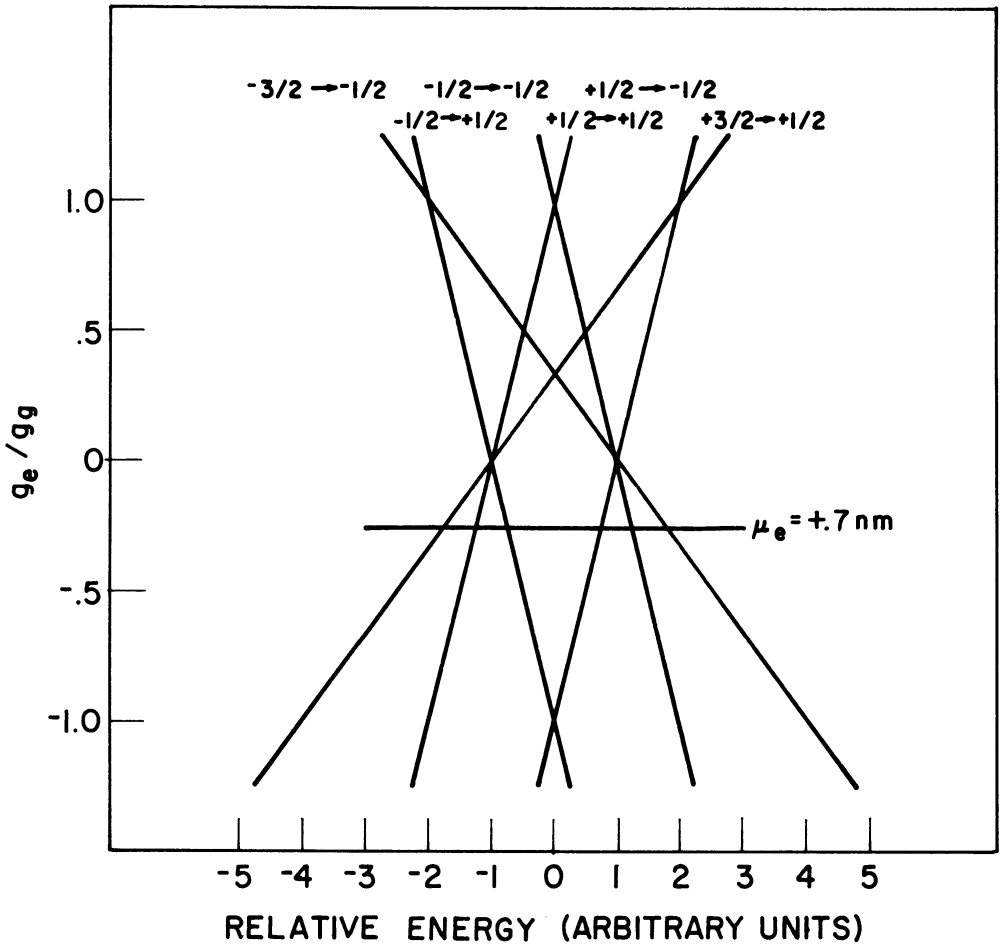

FIGURE II-5

"g-FACTOR DIAGRAM" SHOWING THE RELATIVE LOCATION OF MAGNETIC HYPERFINE STRUCTURE LINES AS A FUNCTION OF THE RATIO OF THE EXCITED STATE TO GROUND STATE g VALUES

line across the diagram. The intercept of this line with the transition lines then gives the relative splitting in the magnetic hyperfine spectrum.

The value of μ_g determined by nuclear magnetic resonance techniques for Te^{125} is $\mu_g = -0.8872$ nm.[57] The excited state moment μ_e has not been experimentally measured, although it is definitely observed to be positive.[33,37] Shikazono[33] has estimated $\mu_e \simeq +.7$ nm by comparing the single neutron $d_{3/2}$ nuclear state of Te^{125} with the nuclides Sn^{119} and Xe^{131} which also have single neutron $d_{3/2}$ excited states. Using the estimated value for μ_e, the g-factor ratio is $g_e/g_g = -.26$. The relative location of the lines in the magnetic hyperfine spectrum for this g-factor ratio is shown in Figure II-5.

The theoretical angular dependence of the intensities of the six transitions numbered in Figure II-4 are[50]

$$I_1 = I_6 = \tfrac{9}{4}(1 + \cos^2\theta)$$

$$I_2 = I_5 = 3\sin^2\theta \qquad \text{(II.27)}$$

$$I_3 = I_4 = \tfrac{3}{4}(1 + \cos^2\theta) \quad ,$$

where θ is the angle between the axis of quantization and the direction of the gamma ray beam. If the internal fields (axis of quantization) are randomly oriented as in a nonmagnetized polycrystalline aggregate, then an average over angles in Equations (II.27) leads to relative intensities 3:2:1:1:2:3 for the six lines. With the application of an external magnetic field, the

internal fields can be aligned. If the internal field is aligned perpendicular to the direction of the gamma ray beam ($\theta = 90^{o}$), the relative intensities of the six lines are 3:4:1:1:4:3. If the internal field is aligned parallel to the direction of the gamma ray beam ($\theta = 0^{o}$), the relative intensities are 3:0:1:1:0:3.

The effective internal magnetic field arises from several different sources. For an independent electron model[58,59]

$$\underline{H}_{eff} = g\mu_o \sum_i \left\{ -\underline{l}_i \langle r_{l_i}^{-3} \rangle + \left(\underline{s}_i - 3(\underline{s}_i \cdot \hat{\underline{r}}_o)\hat{\underline{r}}_o \right) \langle r_{sc_i}^{-3} \rangle - \frac{8\pi}{3} \underline{s}_i \langle r_{c_i}^{-3} \rangle \right\} \quad , \qquad \text{(II.28)}$$

where g is the electron g value and μ_o is the Bohr magneton. The sum is taken over all electrons. $\underline{l}_i$ and $\underline{s}_i$ are the orbital and spin angular momenta for the i^{th} electron and $\langle r_{l_i}^{-3} \rangle$, $\langle r_{sc_i}^{-3} \rangle$, and $\langle r_{c_i}^{-3} \rangle$ are appropriate radial averages of the wave function of the i^{th} electron for the orbital, spin dipolar, and Fermi contact contribution to the effective hyperfine field.

The sum in Equation (II.28) is simplified considerably by the fact that for spherically symmetric states the orbital and spin dipolar contribution is zero. Hence only unfilled electron shells need be considered. The Fermi contact term is proportional to the s-electron spin density at the nucleus, or

$$|\psi_s(0)|_c^2 = |\psi_s(0)|_{\uparrow}^2 - |\psi_s(0)|_{\downarrow}^2 \quad . \qquad \text{(II.29)}$$

For a filled s-shell, the spin density should be zero since the spins are paired. The sum in Equation (II.28) is then reduced simply to a sum over unpaired electrons.

In magnetic compounds of tellurium, the Te^{2-} ion itself is nonmagnetic. On the basis of an independent electron model, the electrons in the $5s^2 5p^6$ electronic configuration for Te^{2-} would be expected to be paired--consequently yielding an $H_{eff}=0$. However, the experimental measurement of hyperfine fields for ions with paired electron orbitals in magnetic materials implies that unpairing of the electron orbitals can occur. Such may be the case for the normally nonmagnetic tellurium ion in magnetic compounds. This unpairing presumably arises from interelectron interactions unaccounted for in the independent electron model. (Such effects are not unexpected since the Sternheimer polarization factor is a manifestation of interelectron interactions for the quadrupole coupling.) Theoretical interpretations of core and conduction electron polarization have been performed for magnetic atoms in ferromagnetic materials.[58,59] However, this has not generally been applied to nonmagnetic atoms in ferromagnetic materials. Only the hyperfine field at the diamagnetic F^- site in MnF_2 has been studied in any detail.[60,61] A discussion of the hyperfine field at the tellurium site in magnetic compounds of tellurium will be presented in Chapter V.

4. Possible Effects of Neutron Capture Induced Displacements on Mössbauer Spectra

Of the three compounds, PbTe, Te, and TeO_2, used for the study of neutron capture induced displacements, PbTe offered

the best possibility for observation of changes in the characteristic Mössbauer spectrum. The previous neutron radiation effects measurements indicated that defects introduced into the PbTe lattice were stable at reactor ambient temperatures.[23-25] For the Te metal, recoil induced displacements are more than likely not stable at reactor temperatures. Measurements of the effects of electron bombardment on Te metal indicate that defects anneal fairly rapidly even at room temperature.[26] No previous radiation effects measurements have been made using TeO_2, so whether or not defects would be stable at reactor temperatures is a matter of conjecture. Based on the defect annealing characteristics then, PbTe is the only compound for which there is positive evidence that defects can be introduced which are stable at reactor irradiation temperatures.

Since PbTe appears to be the most interesting possibility, the effects of defects on the Mössbauer spectrum will be discussed in relation to PbTe. PbTe has the NaCl crystal structure with lattice constant $a_o = 6.452\text{Å}$. The structure is shown in Figure II-6(a). In the normal lattice, the tellurium atoms are in a cubic environment, so no quadrupole splitting is expected. The lack of quadrupole splitting in the normal Mössbauer pattern confirms this observation.

If the tellurium atom was displaced from a normal lattice site, many possible defect configurations could result. In most cases, however, the displaced tellurium atom would end up in a site which no longer had cubic symmetry. Such an environment should give rise to an electric field gradient at the

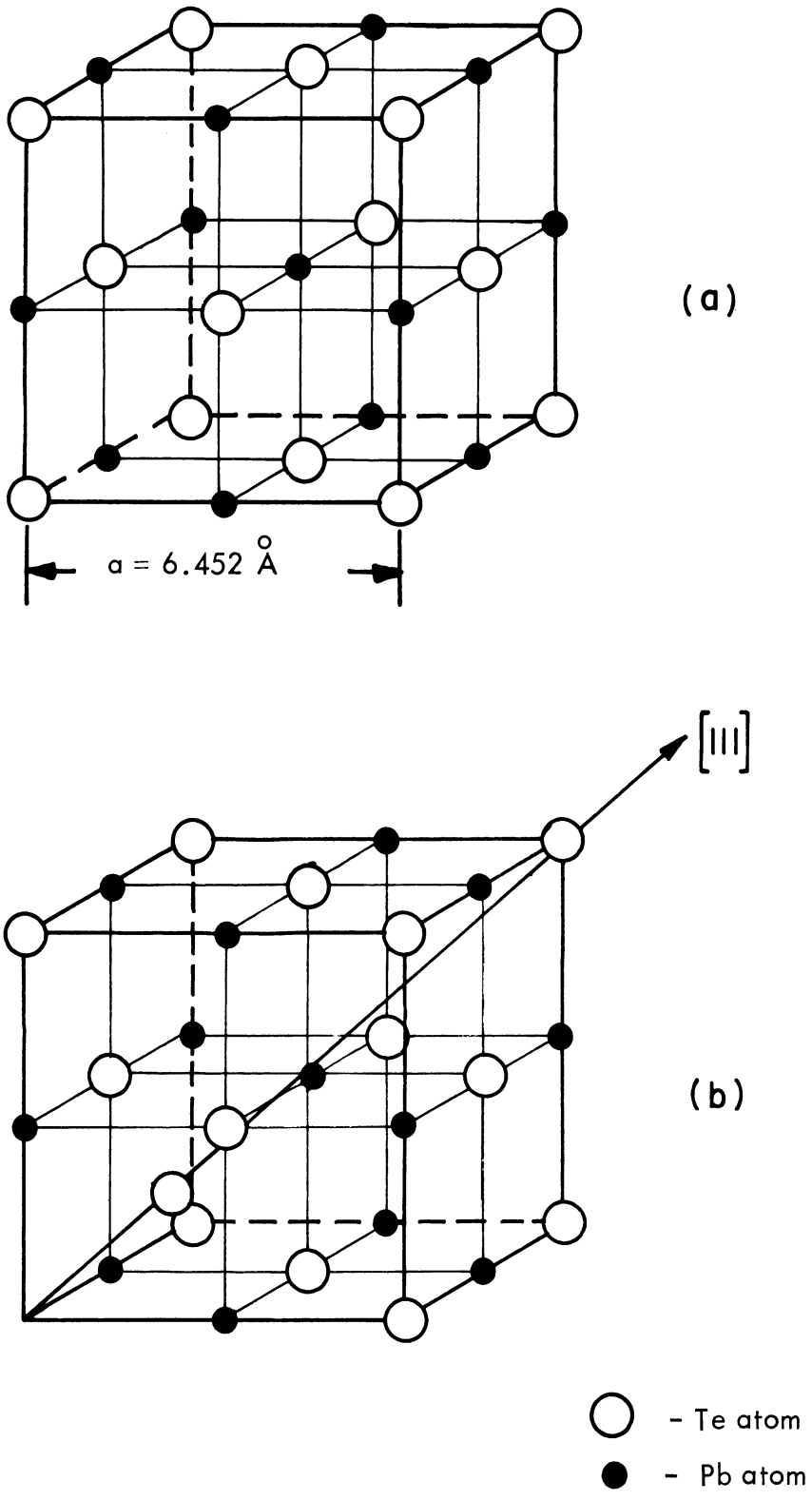

FIGURE II-6

(a) LEAD TELLURIDE CRYSTAL STRUCTURE

(b) FRENKEL DEFECT IN LEAD TELLURIDE LATTICE

tellurium nucleus and subsequent electric quadrupole splitting in the Mössbauer spectrum. One possible simple configuration is shown in Figure II-6(b). Here a Frenkel defect is formed consisting of a vacancy at the original tellurium site and an interstitial at the center of one octant of the unit cell. This configuration was chosen for computational simplicity and does not necessarily represent an energetically stable configuration.[71] It is readily apparent from the figure that there will be an axially symmetric field gradient in the (111) direction.

Each of the possible configurations would also be expected to have a somewhat different isomer shift than found at the normal lattice site due to the alterations in chemical bonding associated with the displacement of the atom from its normal site. The recoil-free fraction, or f value, would also be changed for atoms in defect configurations. Localized vibrational modes would be introduced at the impurity site due to the altered lattice binding forces at this location. These in turn would affect the f value for the impurity atom.

The resultant Mössbauer emission spectrum would be described by a sum over all possible normal and defect configurations of the emission line characteristic for each configuration times the fraction of sites with that configuration. The emission line characteristic of each site would be described by an isomer shift, quadrupole splitting, and f value dependent on the particular configuration.

One of the reasons for using neutron capture induced displacements for the investigation was that the number of possible defect configurations was small. Since the recoil energy due to the prompt gamma ray emission is low, few displacements are produced per thermal neutron captured. With a minimum of displacements, only a relatively small number of defect configurations can be formed. Even with a limited number of defect configurations, it is still highly probable that the resultant Mössbauer spectrum would not display well-defined structure. A sum over several equally probable defect configurations with different isomer shifts and quadrupole splittings would only result in inhomogeneous broadening. The only conditions for which a well-defined structure might be expected is if one defect configuration was dominant and the quadrupole splitting for this configuration was large compared to the natural line width ($\Delta E_Q \gg \Gamma$).

To make a quantitative evaluation of the Mössbauer parameters for defect environments is extremely difficult. As discussed in the preceding section, the electric field gradient eq arises from both the valence electrons and the external lattice charges. The valence electron contribution eq^c is usually the larger due to the $1/r^3$ dependence of eq. Evaluation of the valence electron contribution to eq for displaced atom environments would require knowledge of the defect atom chemical bonding. Detailed knowledge of the electron environment for displaced atoms is known for relatively few

configurations. The only contribution to eq that can be estimated is eq^1 due to the external lattice charges. If an ionic model is assumed, eq^1 can be calculated by performing a lattice sum calculation as described in Equation (II.24). For covalently bonded structures such as PbTe, a lattice sum calculation will certainly be in error. In doing the lattice sum calculation, it is assumed that the valence electrons are localized at the lattice site so the effective charge is that of the free ion. Covalency would result in delocalization of the valence electrons and a reduced effective charge. Being aware of the inadequacy of a lattice sum calculation for a covalent crystal, any result obtained from such a calculation must be treated with some care. Nevertheless, a lattice sum calculation was performed for the configuration described in Figure II-6(b). The result is a field gradient $eq^1 = 49.3\ e/a_o^3$ in the (111) direction. Using $a_o = 6.452\text{Å}$ for PbTe and the measured quadrupole moment Q = .20 barns, the calculated quadrupole splitting is $\Delta E_Q = 2.65 \times 10^{-9}$ ev = .0223 mm/sec. This is very small compared to the line width 2Γ = 5.488 mm/sec. However, we have not taken into account the Sternheimer polarization factor $(1 - \gamma_\infty)$. Although γ_∞ has not been calculated for the $Te^{125\ 2-}$ ion, indications are that it is very large in heavier ions such as this (e.g., γ_∞ for the I^{127-} ion is -179).[55] Such a large Sternheimer antishielding factor would make the quadrupole splitting of the same order of magnitude as the natural line width and perhaps measurable.

Variations in isomer shift are expected to be very small compared to the line width 2Γ. The principal result of the defect production would most likely be in alternation of the 5p valence electron configuration. Such changes would only affect the isomer shift through variations in shielding of the 5s electrons. The measured variation in isomer shift from an empty to a filled 5p shell is of the order of .5 mm/sec. These isomer shifts are quite small compared to the natural line width and not measurable with a high degree of accuracy.

The effects of the defect environment on the Mössbauer recoil-free fraction or f value are even more difficult to predict than hyperfine structure changes. As mentioned earlier, the altered binding forces for the defect atom will introduce localized modes into the lattice vibrational spectrum. These changes in the lattice vibrational spectrum will definitely affect the f value, but the effect is difficult to determine quantitatively. Only for very simple lattices with mass impurities and force constant impurities has quantitative analysis been made of the change in f value.[72,73]

The expected effect of displaced atoms on the Mössbauer spectrum for Te and TeO_2 cannot be predicted with any more certainty than for PbTe. The significant difference for Te and TeO_2 is that the normal Mössbauer spectrum contains a significant quadrupole splitting. Here displaced atom configurations may have significantly lower electric field gradients and may produce structure between the two normal lines. Again isomer shift variations would probably be small.

CHAPTER III.

APPARATUS AND EXPERIMENTAL PROCEDURE

A. Mössbauer Spectrometer

1. Drive System

The Mössbauer effect is observed by measuring the transmission of the resonant gamma ray through an absorber as a function of the relative velocity v between the source and absorber. For each velocity, the gamma ray is then given a Doppler shift in energy

$$\Delta E = \frac{v}{c} E_\gamma \quad , \tag{III.1}$$

where E_γ is the gamma ray energy and c is the speed of light. Relative velocities in the present experiments were obtained by moving the source with a velocity v while the absorber was held stationary. By cyclically sweeping a range of velocities, the energy spectrum can be continuously scanned. To minimize data correction and optimize the counting time, equal times should be spent in each velocity interval. Imposing this condition on the cyclical motion, the velocity wave form should have a triangular shape as a function of time.

A schematic of the experimental system used is shown in Figure III-1. The source was mounted on the moving shaft of a commercially available electromechanical transducer* operated

*Model C31, Pickup Calibrator/Exciter, MB Electronics, New Haven, Connecticut.

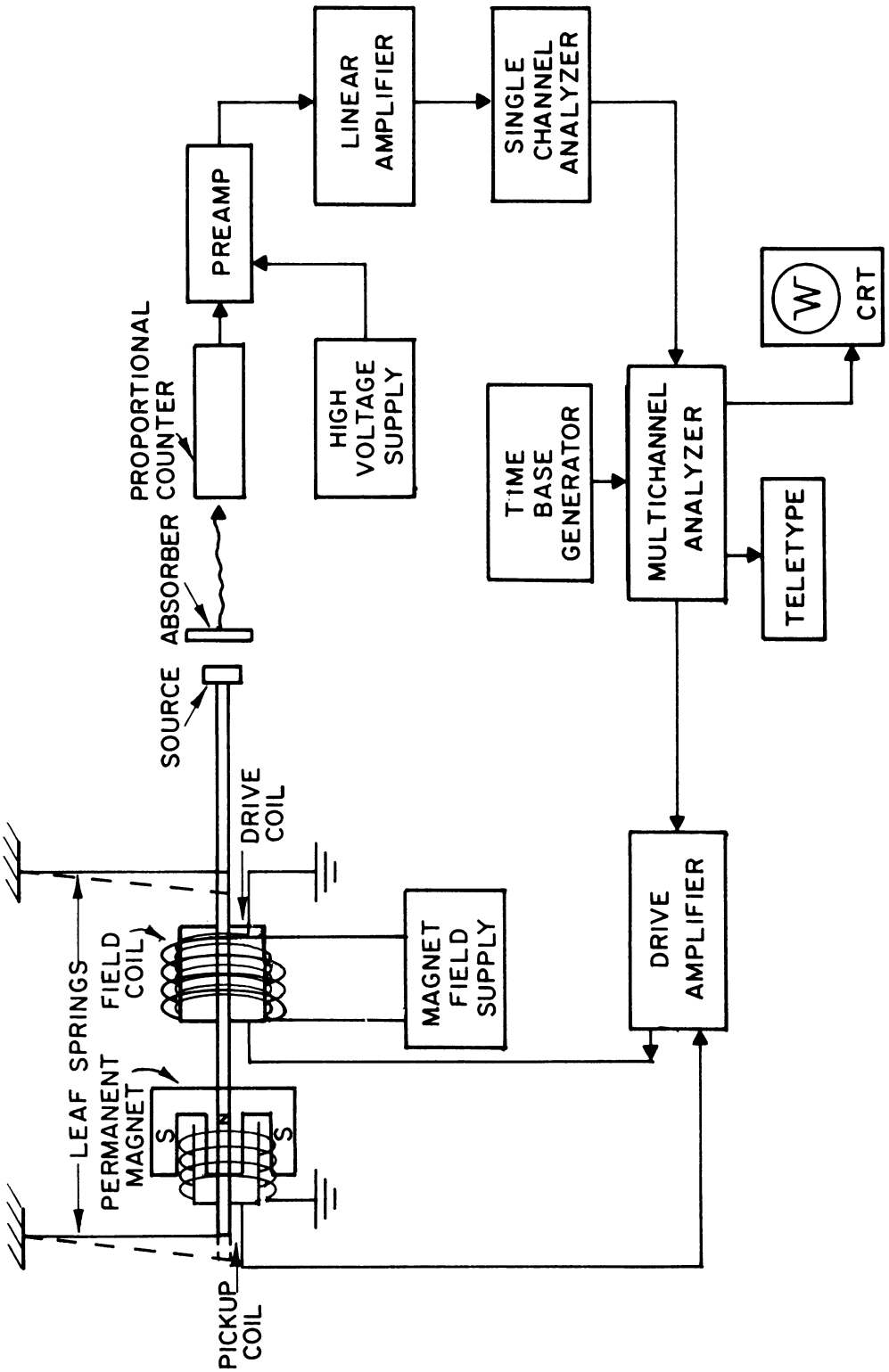

FIGURE III-1

SCHEMATIC OF THE EXPERIMENTAL SYSTEM

in the horizontal position. The moving shaft is supported at both ends with leaf springs. These allow free movement in the horizontal direction but suppress other motion. The original springs were changed to .010 inch phosphor bronze springs to reduce the natural frequency and the effect of transient oscillations and allow greater control of the vibrator with less current. Mounted on one end of the moving shaft is a drive coil which moves within an outer field coil. A magnetic field was produced within the field coil by applying a DC voltage to the magnet coil windings. The magnet field supply is shown in Appendix B, Figure B-1. With the magnetic field activated, the displacement of the moving shaft is proportional to the current through the drive coil.

The velocity of the moving shaft is measured with a pickup coil mounted on the end opposite the drive coil. The pickup coil moves within a radial magnetic field created by a permanent magnet. The output voltage of the pickup coil is proportional to its velocity with a proportionality constant approximately equal to .065 volts/cm/sec.

The electromechanical transducer was driven by a Nuclear Data* multichannel analyzer operating in the time mode. With a rather inexpensive modification by the manufacturer, the analyzer was adapted for operation as a forward-backward multiscaler. The multiscaler dwell time was controlled with a Nuclear Data time base unit.** The analog address scaler signal

*Model ND-180FM, Nuclear Data, Inc., Palatine, Illinois.
**Model ND-180ITB.

generated by the forward-backward multiscaler is a triangular wave form. Using a feedback amplifier, the velocity of the transducer can be forced to follow this triangular wave form. The linearly varying time scale of the multiscaler then corresponds to a digital representation of the linearly varying velocity of the transducer. With the forward-backward drive, only a single Mössbauer spectrum was stored, corresponding to a reflection and overlap of the double spectrum stored in other time mode spectrometers.(62)

The drive amplifier used was similar to that employed by M. B. Stearns.* It is a modified version of the amplifier originally designed by Rubin.(63) A schematic of the drive amplifier is shown in Appendix B, Figure B-2. The analog address scaler signal (.44 volts peak to peak for 256 channels) is amplified 50 times by an operational amplifier** and integrated and differentiated by subsequent operational amplifiers. Since the displacement of the moving shaft is proportional to the current (voltage) through the drive coil, the velocity is proportional to the time derivative of the current. To produce a triangular velocity wave form requires a parabolic displacement wave form. Hence the principal driving voltage is the parabolic output of the integrating amplifier. Triangular and square wave (output of differentiating amplifier) voltage components are combined to provide corrections for the friction

*Scientific Laboratory, Ford Motor Company, Dearborn, Michigan.
**All operational amplifiers are by George A. Philbrick Researches, Inc., Boston, Massachusetts.

and inertia of the transducer. The combined signals are fed through two booster amplifiers to provide the driving current for the transducer. Without feedback, however, the output of the velocity pickup coil varies somewhat nonlinearly. Feedback is provided by amplifying the output of the pickup coil 55 times and comparing it to the triangular wave input signal. The difference signal is then also applied to the booster amplifier.

The operating frequency of the transducer was normally about 10 cps. The frequency is determined by the multiscaler dwell time and the number of channels used (200 μsec and 256 channels, respectively, for the above). The operating velocity range for most of the Te^{125} measurements was $\simeq \pm 2.5$ cm/sec. This velocity range can easily be varied by changing the amplification factor of the signal from the velocity pickup coil.

The observed velocity error signal was approximately .2 percent of the maximum velocity. The major portion of this error signal arises from 60 cycle pickup and noise due to the finite steps in the analog address scaler driving signal. The linearity of the drive system was checked using the magnetic hyperfine spectrum of Fe^{57} metal and plotting the measured peak locations versus the known peak locations. The deviation from linearity was less than .5 percent. Some difficulty was encountered with a phase shift of the analog address scaler signal in the first amplifier stage of the drive amplifier. Efforts to eliminate this were not completely successful and the phase shift had to be compensated electronically using

the differentiated signal. The maximum line broadening due to both noise and phase shift was determined by evaluation of the excess broadening in the lines of the Fe^{57} calibration spectrum. Correcting only for absorber thickness, the unaccounted broadening amounted to .27 percent of the full velocity range of ± 2.5 cm/sec.

Live display of the multichannel analyzer memory was provided by a Tektronix oscilloscope.* Data was printed out using a teletype machine.** The teletype provides both a typewritten page printout and an ASCII coded punched paper tape output.

The velocity scale of the analyzer was calibrated using the room temperature Mössbauer hyperfine spectrum of Fe^{57} in a natural iron absorber. The six-line spectrum was fit using the excited and ground state splitting factors $g_1 = 2.245$ mm/sec and $g_0 = 3.922$ mm/sec determined by Preston, et al.[87] Some care must be exercised, however, in the interpretation of such calibrations, using uncalibrated natural iron absorbers. The effective internal hyperfine fields can vary by ~ 1.5 percent between different natural iron foils, depending on the metallurgical history of the samples. This uncertainty was included in the error bars listed for all measurements. Velocity calibrations were performed after each tellurium run.

The only difficulty encountered using the Fe^{57} hyperfine spectrum for calibration was the difference in velocity range

*Type 503, Tektronix, Inc., Beaverton, Oregon.
**Model 33TC, Teletype Corporation, Skokie, Illinois.

of Te^{125} and Fe^{57} Mössbauer spectra. The full Fe^{57} hyperfine spectrum occupied only one-fifth of the velocity span used for the Te^{125} measurements. When using 128 channels, this provided limited resolution of the six-line spectrum. A room temperature calibration standard with larger splittings than Fe^{57} would be desirable. Eu^{151} is currently being investigated as such a standard.

2. Cryostat

The low Debye temperatures for most tellurium compounds ($\theta_D \sim 150^{\circ}K$) necessitate Mössbauer measurements with both the source and absorber at liquid nitrogen temperature or lower. The cryostat shown in Figure III-2 was designed for use with both the source and absorber at liquid nitrogen temperature and with the motion fed through from the outside to the source. The cryostat was similar to one originally described by DeWaard, DePasquali, and Hafemeister.[64,65] The chief features of this cryostat were the low cost, simplicity in construction, and ease of operation.

The cryostat consisted of a commercially available 8 liter stainless steel Dewar.* A 3" x 2½" x 15" block of aluminum acted as a cold finger for conduction cooling of the source and absorber. The source and absorber mounting was completely assembled prior to insertion in the cold finger and then was simply threaded into the aluminum block. The source and absorber mounting consisted of an outer aluminum holder fitted

*Virtis Company, Inc., Gardner, New York.

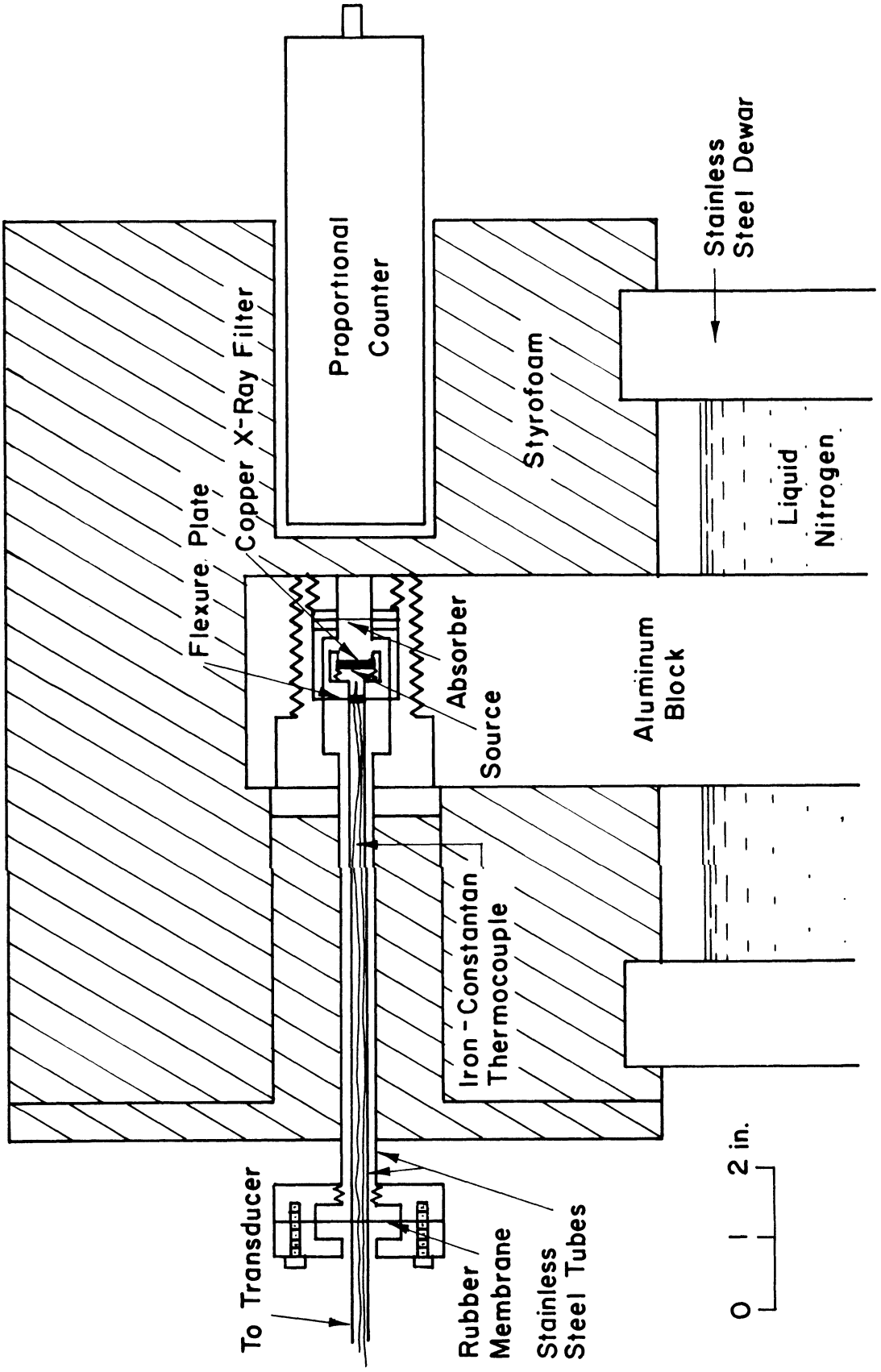

FIGURE III-2

CRYOSTAT

with a ½" diameter stainless steel tube. The sources were mounted in a small aluminum holder which was attached to a 1-1/8" diameter, 6 mil thick beryllium-copper flexure plate* and a ¼" diameter stainless steel tube. This tube acted as the source driving rod. The flexure plate was held in the holder with a cap on which was mounted the absorber holder. The cap and absorber holder were firmly clamped in place with a second screw cap.

After mounting in the aluminum cold finger, the stainless steel driving rod was coupled to the moving shaft of the electromechanical transducer by a second piece of tubing. The source and absorber holder was sealed to the air with a rubber membrane mounted at the joint of the two driving rods and clamped between two pieces of aluminum attached to the outer stainless steel tube.

An iron-constantan thermocouple was sealed inside the aluminum source holder with epoxy. The leads pass out through the driving rod to a temperature recorder.**

The aluminum cold finger and source and absorber holder were insulated with styrofoam. A single block of styrofoam was cut in the proper shape to fit over the aluminum cold finger and to seal on the rim of the stainless steel Dewar. The source and absorber holder was mounted through a hole in the side of the styrofoam block, which was sealed with a piece

*The beryllium-copper flexure plates were prepared by etching the pattern in ferric chloride etching solution.
**Fisher Recordall, Fisher Scientific.

of styrofoam after mounting. The styrofoam block was rigidly clamped to a work bench after the driving rod was coupled to the transducer.

The temperature of the source and absorber in the cryostat was 82°K when the Dewar was completely full. The temperature increase during a cycle was approximately 9°K. The liquid nitrogen boil-off rate was about 1 liter/hour.

3. Detection System

As discussed in Chapter II, one of the difficulties in the detection of the 35.6 kev gamma ray of Te^{125} is the intense background from the K_α and K_β x-rays at 27.4 kev and 31.2 kev. The number of x-rays and gamma rays emitted per decay from the 145 kev level was calculated in Chapter II as $K_\alpha : K_\beta : \gamma = .942 : .203 : .070$.

The three energy peaks cannot be resolved using a NaI scintillation crystal and can only be partially resolved with a proportional counter. The difficulty with resolution can be circumvented by detecting only the escape peak. Violet[29-31] originally used this method with a NaI scintillation detector; however, the method is equally applicable with a xenon-filled proportional counter. In both iodine and xenon, the energy of the K-absorption edge (33.17 kev and 34.51 kev, respectively) is between the Te^{125} x-ray and gamma ray energy. Thus, only the 35.6 kev gamma ray absorption is capable of K-shell photoelectric absorption and subsequent excitation of iodine and

xenon x-rays. The escape peak arises from the loss of the iodine or xenon x-rays from the detector.

The technique was tried using both a thin NaI(Tl) scintillation crystal* and xenon-filled proportional counter.** The calculated optimum NaI crystal thickness for this technique is 9 mils; however, there is considerable difficulty in cleaving crystals this thin. The crystal provided by Harshaw was apparently much thicker, and consequently the escape peak efficiency was quite low. In addition, the resolution of the escape peak was considerably better with the proportional counter than with the scintillation detector. Subsequently, all measurements were made with the proportional counter rather than the scintillation detector.

The pulse height spectrum taken with the xenon/nitrogen-filled proportional counter is shown in Figure III-3(a). The x-ray and gamma ray photopeaks are not resolved. Escape peaks occur at both 3.0 kev and 7.0 kev energies corresponding respectively to the loss of the xenon K_β and K_α x-rays. The 3.0 kev peak occurs below the noise threshold, so only the 7.0 kev peak is selected for the Mössbauer experiment. The signal-to-noise ratio of the escape peak can be improved a factor of 3.5 with only a factor of 1.5 reduction in the count rate by using a Cu absorber to selectively filter out the tellurium x-rays. With a 5 mil Cu absorber (113 mg/cm^2), the intensities at the detector are reduced to $K_\alpha : K_\beta : \gamma = .186 : .066 : .033$. Less

*Integral Line Assembly, Harshaw Chemical Company, Cleveland, Ohio.

**Model RSG-30A, Reuter-Stokes Electronic Components, Inc., Cleveland, Ohio.

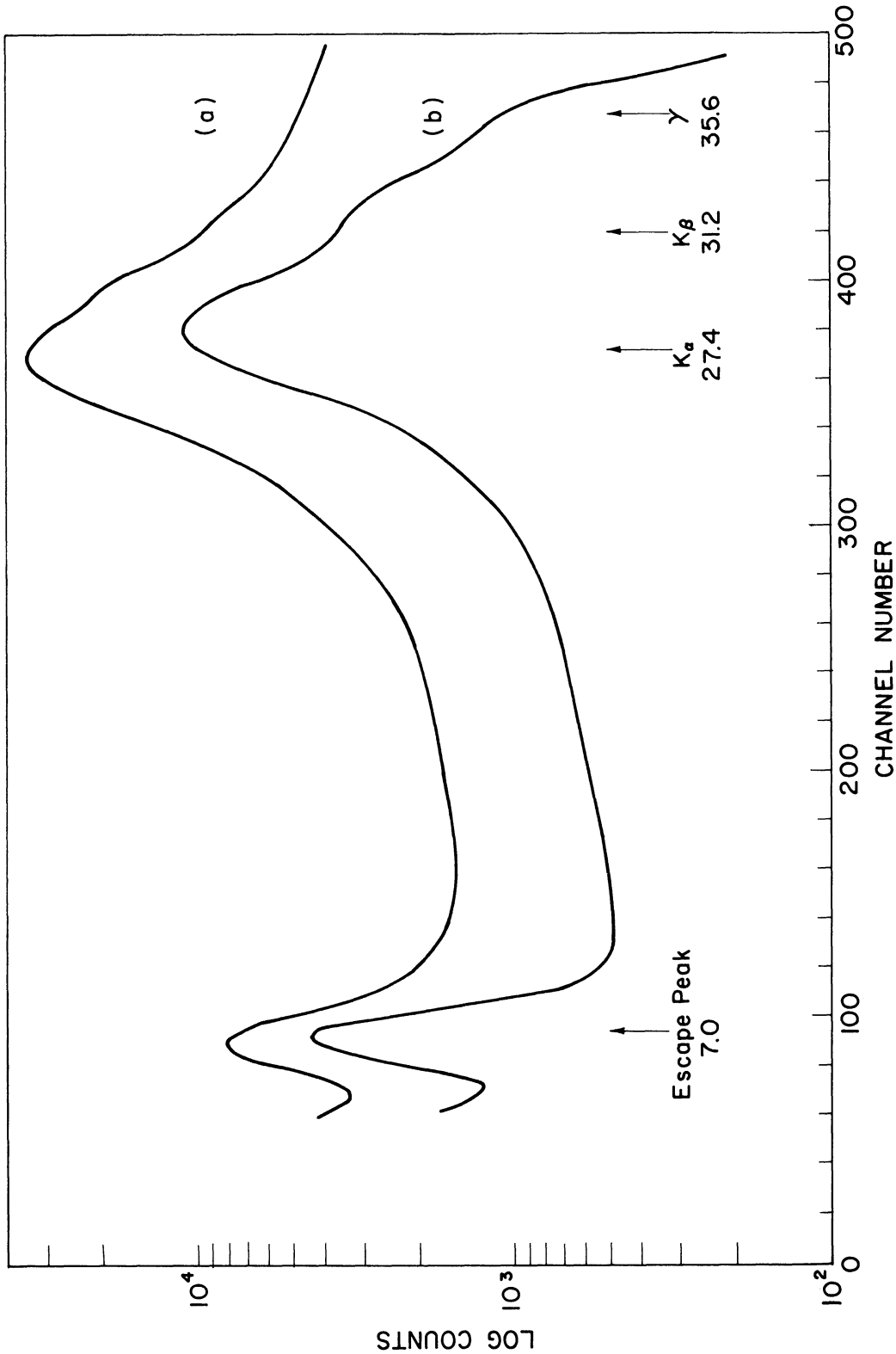

FIGURE III-3

Te^{125m} GAMMA AND X-RAY SPECTRUM TAKEN WITH A XENON-NITROGEN PROPORTIONAL COUNTER USING: (a) NO X-RAY FILTER, AND (b) 5 Mil Cu X-RAY FILTER

than 1 percent of the 8.0 kev copper x-rays generated by the photoelectric absorption are transmitted through the 20 mil aluminum window on the proportional counter. The spectrum taken using the 5 mil Cu absorber is shown in Figure III-3(b). The energy resolution of the escape peak is 26 percent and the signal-to-noise ratio is 3:1. The signal-to-noise ratio could be improved further by using a thicker copper selective absorber. However, the decreased count rate made this prohibitive.

The output pulses from the proportional counter were fed through a preamplifier and double delay line linear amplifier into a single channel analyzer.* The proportional counter voltage was supplied by a regulated high voltage power supply.** The pulses in the escape peak were selected with the single channel analyzer. Peak settings are easily accomplished using a multichannel analyzer by coincidence gating the total spectrum with the output pulses of the single channel analyzer. The single channel analyzer output pulses were stored in the multichannel analyzer operating in the multiscaler mode.

B. Source and Absorber Preparation

1. Sources

All of the sources used in the experiments described in this paper consisted of Te^{125m} in various compounds of tellurium. The Te^{125m} was prepared by the reaction $Te^{124}(n,\gamma)Te^{125m}$ as described in Chapter II. Irradiations must be done using

*Models NB-19, NA-12D, and NC-14, Hamner Electronics Company, Inc., Princeton, New Jersey.
**Model N-4035.

tellurium compounds enriched in Te^{124}. This is made necessary by the presence of stable isotopes of tellurium (notably Te^{120}, Te^{122}, Te^{126}, Te^{128}, and Te^{130}) which have abundances and capture cross sections comparable to Te^{124} and which produce reaction products with half lives comparable to Te^{125m}. The gamma and x-rays produced in the decay of these reaction products would create a background intolerable for detection of the Te^{125m} 35.6 kev gamma ray. The source enrichments were all 93.9 percent in Te^{124}.

a. PbTe

The $PbTe^{124}$ was prepared by New England Nuclear Corporation (NEN)* by reacting stoichiometric amounts of Pb and Te in vacuum for 30 minutes at 900°C. The sample was in powder form and had a purity greater than 99 percent. The principal contaminant in the sample was sulfur, which was present in the enriched Te^{124} obtained by NEN.

For use as a source in the radiation effect measurements, the $PbTe^{124}$ powder was pressed into the form of a thin platelet and sintered. The initial density of the powder was only 37.6 percent of that of the solid material. Densification was achieved by several compacting and grinding steps. The final platelet was formed by grinding the densified powder through a 100 mesh screen and pressing between two steel plates with approximately a 20,000 pound load.

*New England Nuclear Corporation, Boston, Massachusetts.

The ¼" diameter platelet was sintered in a hydrogen atmosphere in an annealing furnace at 550°C for three hours. The annealing removes the stresses induced by the compacting and causes recrystallization and coalescence of the powder particles. Less than 10 percent of the mass was lost by sublimation during the sintering. The resultant platelet was quite brittle, but successfully withstood several handlings. The weight of the irradiated platelet was 57.7 mg.

b. Te Metal

The Te^{124} metal was supplied by NEN. The metal was electromagnetically enriched in Te^{124}. The samples were of purity greater than 99 percent, with sulfur as the major contaminant.

A sintered metal platelet was prepared using the same procedure as for the PbTe. The platelet was annealed at 350°C for six hours. The weight of the irradiated platelet was 30.3 mg.

c. TeO_2

$Te^{124}O_2$ was prepared from Te^{124} metal using a modification of the procedure described by Marshall.[66] Samples of Te^{124} weighing approximately 60 mg were placed in a 50 ml beaker and covered with 10 ml of water. 10 ml of HNO_3 were slowly added to dissolve the Te metal. The clear liquid was then evaporated on a water bath in an open 20 ml beaker. Crystals of basic tellurium nitrate ($2TeO_2 \cdot HNO_3$) were deposited during the evaporation. Evaporation was continued to dryness. The beaker was

then covered with a watch glass and heated in an oven for two hours at 415°C. The decrepitation of the basic tellurium nitrate yielded TeO_2 in the tetragonal crystal form. X-ray diffraction analysis of the powder confirmed the existence of only the tetragonal crystalline modification with lattice constants $a_o = 4.810\text{Å}$ and $c_o = 7.613\text{Å}$ (X-Ray Powder File, Card 11-693).

Some other interesting observations were made during preliminary preparations of TeO_2. X-ray diffraction measurements of the "basic tellurium nitrate" crystals deposited on evaporation indicated the structure was nearly identical to the tetragonal TeO_2. Only a slight trace of additional structure was discernible in the diffraction pattern. This observation was further confirmed by the catalogued diffraction pattern (X-Ray Powder File, Card 1-0862) for "basic tellurium nitrate," which is essentially the pattern for tetragonal TeO_2 with only slight differences. The origin of the apparent similarity is the nearly identical Te-O structure for tetragonal TeO_2 and $2TeO_2 \cdot HNO_3$.[101]

The possibility of introducing a phase change from the tetragonal to the orthorhombic structure on heating was indicated by Marshall.[66] The existence of a phase change was studied by heating the sample at various temperatures and taking the x-ray diffraction pattern after each heating. Samples were heated in an annealing oven at 405°C, 630°C, and 775°C. The first two samples were heated for two hours. The

latter sample was melted (MP = 733°C) and quickly cooled to room temperature. The diffraction pattern for each of the samples following heating showed only the tetragonal crystal structure. This indicates that over the temperature range from 405°C to the melting point TeO_2 forms only a tetragonal lattice. No structure change from the tetragonal to the orthorhombic phase was observed. This result is confirmed by Zlomanov, et al.,[67] who observed the identical result over the range 457-704°C. Dutton and Cooper[68] have concluded that the tetragonal form is produced by any artificial method of preparation and the rhombic structure occurs only for the naturally occurring mineral "tellurite."

For use as source material, the $Te^{124}O_2$ was retained in powder form. Powder samples were sealed in aluminum foil packets for irradiations.

2. Absorbers

All of the absorber material used were in powder form. Rigid absorbers were prepared by imbedding the powder in lucite. The procedures was as follows: The powdered tellurium compounds were ground through 100 mesh screen and thoroughly mixed with ~100 mg of 100 mesh lucite powder. The mixture was placed in a 5/8" diameter stainless steel mold between two heater plates in a mechanical press.* Approximately 200 psi was applied and the mold was heated to 115°C and quenched. The powder appeared to be very homogeneously dispersed. The thin, rigid mounting proved very convenient to use.

*Carver Laboratory Press, Fred S. Carver, Inc., Summit, New Jersey.

It was originally felt that absorbers enriched in Te^{125} would be necessary to provide significant f values. Assuming no resonant absorption occurs in the source, the maximum resonant intensity is given by[69]

$$\epsilon(0) = \frac{P(\infty) - P(0)}{P(\infty)} \qquad \text{(III.2)}$$

$$= f_s\left[1 - e^{-T_A/2}\, J_o\left(i\,T_A/2\right)\right] , \qquad \text{(III.3)}$$

where f_s is the source f value and T_A is the effective absorber thickness

$$T_A = f_A\, n_A\, a_A\, \sigma_o\, t_A \quad . \qquad \text{(III.4)}$$

f_A is the absorber f value, n_A is the number of atoms per cubic centimeter, a_A the fractional abundance of resonantly absorbing atoms, σ_o the resonant cross section, and t_A the absorber thickness. An increased abundance a_A increases T_A and $\epsilon(0)$ approaches the source f value.

However, the resolution of hyperfine structure in Te^{125} is inherently poor due to the broad natural line width. This necessitates the use of thin absorbers to minimize the line broadening. The experimentally measured line width is given as[69]

$$\Gamma_{theor} = (2 + .27\,T_A)\Gamma \qquad T_A \leq 5 \quad . \qquad \text{(III.5)}$$

Here it is assumed that the effective source and absorber line widths are equal and equivalent to the natural line width. For values of T_A less than one, the line width increase is less than 15 percent. With poor resolution, however, even a broadening of this magnitude can be significant. In the end, the need for better resolution exceeded the need for higher f values and natural abundance absorbers were used.

The absorber thicknesses were chosen to maximize the information obtainable from a Mössbauer experiment. The criterion for maximum information is that the ratio of the maximum resonant intensity in counts per channel to the standard deviation of the counts per channel be a maximum, or

$$\mathcal{J}_{max} = \max\left(\sqrt{P(\infty)}\,\epsilon(0)\right) \quad . \tag{III.6}$$

Using Equation (III.3) and the fact that

$$P(\infty) = S e^{-\mu x_A} \quad , \tag{III.7}$$

where S is an appropriate source strength per channel, μ is the electronic absorption coefficient in cm^2/mg, and $X_A = \rho t_A$ is the absorber thickness in mg/cm^2, the maximum of Equation (III.6) can be determined. The ideal effective absorber thickness is given as the solution to

$$\left(\mu/c_A\right) e^{T_A/2} = \frac{\left[I_0\left(T_A/2\right) - I_1\left(T_A/2\right)\right]}{\left[1 - e^{-T_A/2}\, I_0\left(T_A/2\right)\right]} \quad , \tag{III.8}$$

where $C_A = T_A/X_A$. The solution to Equation (III.8) is shown in Figure III-4 for various μ/C_A ratios. The optimum effective absorber thickness is the intercept with the appropriate μ/C_A curve.

Since the f values for most of the tellurium absorbers were not known, the μ/C_A ratio could only be estimated. This introduced considerable uncertainty in the optimum thickness. For most natural abundance tellurium absorbers (a_A^{125} = 6.99 percent), the optimum thickness is of the order of 50 mg/cm^2.

The effective thicknesses of the prepared absorbers were determined by measuring the attenuation in the absorbers of the 14.4 kev Fe^{57} gamma ray from a Co^{57} source. These values are all tabulated in Table III-1.

From Equations (III.4) and (III.5), it is possible to calculate the expected line width for each absorber, correcting for the absorber broadening. For most of the absorber materials, the Debye temperature is unknown so the value cannot be calculated directly. The Debye temperature for TeO_2 was measured previously as $\Theta_D \simeq 170^oK$.[32]

A comparison of the measured resonance intensities and absorption areas of the other compounds with TeO_2 indicated that an assumed Debye temperature of $\Theta_D \sim 170^oK$ for each of them would not be too unreasonable. The line widths listed in Table III-1 were calculated under this assumption. For the absorbers with a natural abundance of Te^{125}, the absorber corrections amounted to $\sim$10 to 20 percent of the natural line width. An extreme error

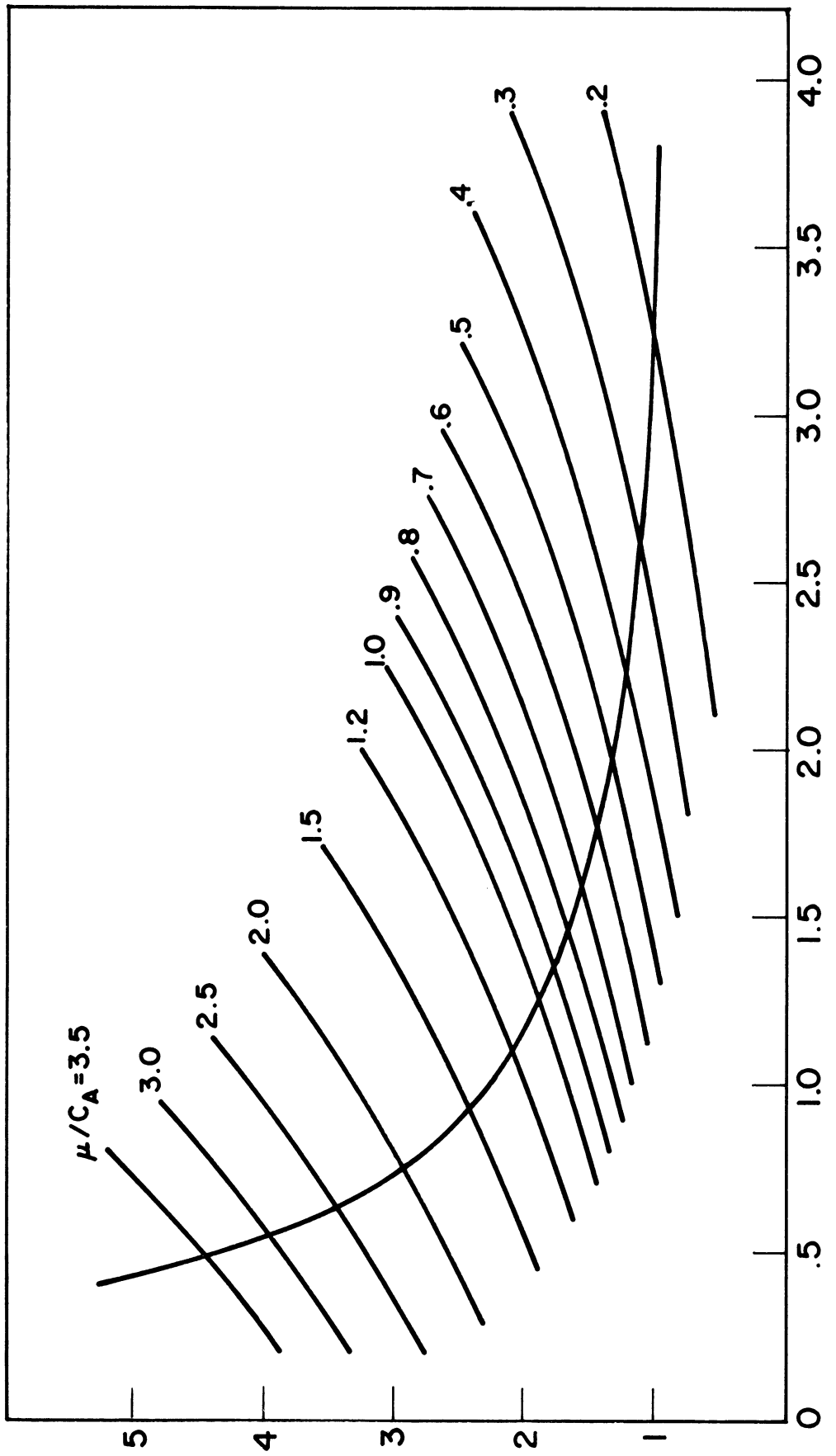

FIGURE III-4

OPTIMUM EFFECTIVE ABSORBER THICKNESS
FOR MAXIMUM INFORMATION

TABLE III-1

MEASURED THICKNESS AND ESTIMATED LINE WIDTH FOR TELLURIUM ABSORBERS

Absorber	Total* Thickness (mg/cm^2)	Te^{125} (%)	Te^{125} Thickness (mg/cm^2)	Θ_D** (^oK)	T_A	Γ_{theor} (mm/sec)
PbTe-1	17.2	95	6.2	150	2.0	7.0
PbTe-2	17.9	95	6.4	150	2.1	7.1
TeO_2	61.9	7	3.5	170	1.5	6.6
$CuCr_2Te_4$-1	30.7	7	1.6	170	.7	5.9
$CuCr_2Te_4$-2	53.5	7	2.8	170	1.2	6.4
MnTe	32.8	7	1.6	170	.7	6.0
CrTe	35.2	7	1.4	170	.8	6.1
H_6TeO_6	39.0	7	1.5	170	.7	6.0

*Thickness determined by gamma ray attenuation measurement.
**Debye temperatures are estimated values except for PbTe and TeO_2.

of 100 percent in the estimated value of T_A would amount to only $\sim$ 10 to 20 percent error in the estimated line width.

The Mössbauer spectra for H_6TeO_6, $CuCr_2Te_4$, and TeO_2 gave measured line widths which were only of the order of 5 percent greater than the calculated value. Broadening of this magnitude can be accounted for principally by the uncertainty in the estimated line width and the experimentally introduced broadening. Other small contributions include source broadening and absorber inhomogeneities. The MnTe and CrTe lines were broadened by unresolved hyperfine splittings, as will be discussed in Chapter V. The PbTe absorbers enriched in Te^{125} displayed line widths approximately 36 percent greater than the expected value. This will be discussed in Chapter IV.

Information on the procedures used for preparation of the tellurium compounds used as absorbers is given below.

a. PbTe

Lead telluride enriched to 95.0 percent in Te^{125} was prepared by NEN as described in the above section dealing with sources.

b. TeO_2

Tellurium dioxide with natural abundance tellurium was prepared using the procedures described in the above section dealing with sources. X-ray diffraction confirmed the existence of only the tetragonal crystalline form.

c. $CuCr_2Te_4$

$CuCr_2Te_4$ powder was obtained from C. Colominas.* The procedure used in preparation of the material and the results of neutron and x-ray diffraction study of the material are reported in a recent paper.(70)

d. MnTe

A sample of manganese telluride powder was obtained from Tseng-Ying Tien.** The sample was selected from several which had been prepared as being the closest to a stoichiometric mixture. The sample was prepared using approximately 1 percent excess tellurium by weight. High purity Mn and Te powder were ground through 200 mesh screen, mixed, and pressed into pellet form. The powders were reacted in a graphite crucible in an evacuated Vycor tube. The graphite was used because of the high heat of reaction and because the MnTe reacts with Vycor. The powder was reacted for four hours at 500°C. X-ray diffraction patterns indicated no trace of the elements or other compositions.

e. CrTe

Chromium telluride was prepared by reacting high purity Cr and Te powder. Stoichiometric amounts of Cr and Te were mixed and ground together. The powder was sealed in an evacuated quartz tube and heated at 1000°C in a temperature controlled,

*C.N.R.S., Grenoble, France.
**Department of Chemical and Metallurgical Engineering, The University of Michigan, Ann Arbor, Michigan.

rotating combustion furnace for 19 hours. The CrTe was removed from the quartz tube and the sample was reground and again sealed in an evacuated quartz tube. The powder was heated to 1000°C for 21 hours and then quenched to room temperature. The reheating was done to insure the homogeneity of the sample.

X-ray diffraction patterns confirmed the presence of CrTe of hexagonal structure with lattice constant a_o = 3.96Å and c_o = 6.17Å (X-Ray Powder File, Card 2-0682). There was no trace of any additional structure in the diffraction pattern.

f. H_6TeO_6

A sample of orthotelluric acid in powder form was obtained from the Department of Chemistry of The University of Michigan. The procedure used in preparation was not known. X-ray powder diffraction patterns agreed well with the data for the cubic phase with lattice constant a_o = 15.51Å (X-Ray Powder File, Card 1-0329). Some monoclinic form may be present since it is somewhat difficult to distinguish between the two phases with the x-ray diffraction pattern.(68)

C. Source Irradiations

The sources were all irradiated in the Ford Nuclear Reactor at The University of Michigan. The reactor is a swimming pool-type research reactor which operates at two megawatts. The core consists of enriched U-235 fuel elements. The core is light water moderated, but a tank of D_2O has been installed on one face to act as a reflecting element. Provision is made for

irradiations in core, in the heavy water tank, or in the light water moderator away from the core. The highest thermal neutron flux is obtained in the D_2O tank holes nearest the core. The flux here is approximately 2.5×10^{13} neutrons/cm^2-sec; however, the cadmium ratio (thermal flux/fast flux) is only 4.5. Sources which were not used for radiation effects measurements were usually irradiated at this location or in the core (approximately 1.5×10^{13} neutrons/cm^2-sec maximum thermal flux).

The sources used in the radiation effects measurements were irradiated at lower thermal neutron fluxes but with higher cadmium ratios to minimize fast neutron effects. The thermal and fast neutron fluxes used for each of these sources are listed in Table III-2.

TABLE III-2

IRRADIATION CONDITIONS FOR Te^{125} SOURCE MATERIALS FOR RADIATION EFFECTS MEASUREMENTS

Source	φ_{th} (n/cm^2-sec)	φ_f (n/cm^2-sec)	t (hrs)	$\varphi_{th} t$ (n/cm^2)	$\varphi_f t$ (n/cm^2)	φ_{th}/φ_f
PbTe	6.4×10^{11}	5.3×10^{10}	336	7.7×10^{17}	6.4×10^{16}	12
Te	6.4×10^{11}	5.3×10^{10}	400.7	9.2×10^{17}	7.6×10^{16}	12
TeO_2	5.8×10^{12}	4.5×10^{10}	399.3	8.3×10^{18}	6.5×10^{17}	13

Both the PbTe and Te metal platelets were mounted in an aluminum holder for the irradiations. The TeO_2 powder was sealed in an aluminum foil packet. The source holders were then sealed in a 3/4" diameter by 2' aluminum tube by welding

caps on both ends of the tube. This was made necessary by the relatively long irradiation times. Sources were irradiated by inserting the tubes directly into the irradiation holes.

Following irradiation, the samples were stored in the pool for a period of approximately one week. This reduced the 15-hour Na^{24} activity produced by the reaction $Al^{27}(n,\alpha)Na^{24}$ to a tolerable level so that the irradiation tube could be safely handled. The Te^{125} sources were then removed from the aluminum holders and remounted to eliminate any background activity from the holders.

All irradiations were done at reactor ambient temperature. Measurements were made of the sample temperatures during irradiation by inserting dummy source holders into the core with copper-constantan thermocouple wires attached. Equilibrium sample temperatures ranged from a maximum of 55°C at the in-core irradiation hole to 41°C in the second irradation cup (C2) in the water away from the core.

CHAPTER IV.

EXPERIMENTAL RESULTS OF THE RADIATION EFFECTS MEASUREMENTS

The procedure used for investigating the effects of neutron capture on the Mössbauer spectrum was as follows: The PbTe, Te, and TeO_2 source materials were prepared and irradiated as described in Chapter III. After irradiation, the Mössbauer spectrum was taken for each of the sources against a single line absorber. These spectra should be characteristic of the lattice with atoms displaced from normal lattice sites by the mechanism described in Chapter II. The spectra characteristic of the "ideal" lattice were obtained using the same sources following treatment to restore the displaced atoms to their normal lattice environment. In the case of the PbTe and Te metal, the defects were removed by annealing. The PbTe was heat treated in a hydrogen atmosphere for 11 hours at 400°C. The Te metal was also annealed in a hydrogen atmosphere at 350°C for 12 hours. The TeO_2 powder was dissolved and recrystallized following the procedure described in Chapter III. The Mössbauer spectrum was taken again for each of the sources under the same conditions as the initial spectrum. These data served as reference spectra characteristic of the "ideal" lattice. By comparison of the "defect" and "ideal" Mössbauer spectra, the effects of the neutron capture induced displacements could be determined.

The following are the results and discussion of the measurements on PbTe, Te metal, and TeO_2.

A. PbTe

1. Results

The Mössbauer spectrum was taken using the $PbTe^{125}$ source and a single line PbTe absorber enriched to 95 percent in Te^{125}. The measurements were all made at liquid nitrogen temperature. The data taken in the Mössbauer measurement before annealing are shown in Figure IV-1. The data, uncorrected for background, are presented as the resonance absorption normalized to the background counting rate. The solid line is the best fit with a single Lorentzian line shape.* The results of the fitting to the Mössbauer spectrum after annealing are shown by the dashed line in Figure IV-1. The fitting parameters and the error limits** for each of the spectra are listed in Table IV-1.

TABLE IV-1

PARAMETERS FROM PbTe RADIATION EFFECTS DATA

PbTe Source	Γ_{exp}*** (mm/sec)	δ # (mm/sec)	Resonance## Intensity	Area### (mm/sec)	χ^2/N
Pre-anneal	9.60 ± .23	.07 ± .05	.0324± .0003	.444	1.469
Post-anneal	9.58 ± .22	.03 ± .04	.0351± .0003	.471	1.142

*The least squares fitting program is described in Appendix C.
**The error limits for line shifts and splittings include both statistical error and uncertainty in the velocity calibration. The error limits on the intensity are only statistical and do not include experimental uncertainty.
***Full width at half maximum of the resonance line.
#The center shift relative to zero velocity.
##Maximum resonance intensity uncorrected for background.
###Area under the resonance spectrum obtained by numerical integration.

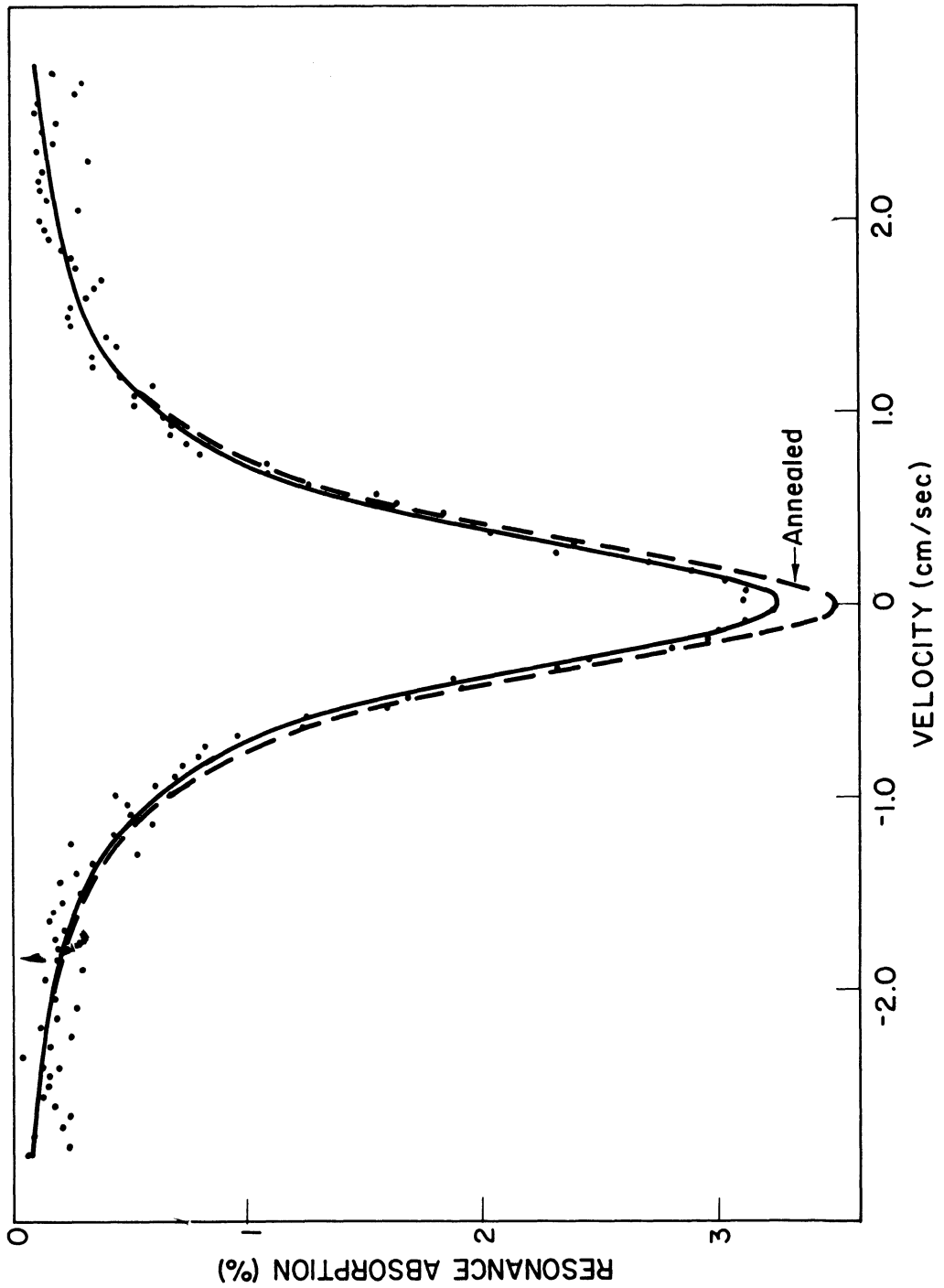

FIGURE IV-1

RESONANCE ABSORPTION SPECTRUM FROM THE PbTe SOURCE AND PbTe ABSORBER BEFORE AND AFTER ANNEALING

The following observations can be made of the data. The line width remains constant in the two measurements. The isomer shift is slightly more positive* before annealing, but it is not statistically significant. A similar experiment performed earlier did not show this same trend. The line intensity, uncorrected for background, increases 7.7 percent upon annealing. The increase in area of 5.8 percent is approximately equal to the change in line intensity.

2. Discussion of the Data

a. Radiation Effects

In summary, the only apparent difference between the spectra is in the resonance intensity. This change in resonance intensity will be discussed following presentation of the results of the Te and TeO_2 data. These results for reactor irradiation of $PbTe^{124}$ do not show the dramatic change in isomer shift reported by Stepanov and Aleksandrov.[17] The reported isomer shifts up to 2 mm/sec should easily be seen in the present measurement. The lack of such a shift in the present measurement is probably due to the lower concentration of fast neutron defects. The irradiation conditions for the Stepanov and Aleksandrov experiment were considerably different than ours. The integrated thermal flux for irradiations by Stepanov and Aleksandrov was 9.0×10^{20} neutrons/cm^2 compared to the value 7.7×10^{17} neutrons/cm^2 listed in Table III-2 for the present

*Positive velocities are defined by the motion of the source toward the absorber.

measurement. No information was presented in their paper on the fast flux; however, with a reactor thermal flux of 2.3×10^{14} neutrons/cm^2-sec, the cadmium ratio is probably no better than 5. With this assumption, the integrated fast flux would be 1.8×10^{20} neutrons/cm^2 compared to our value of 6.4×10^{16} neutrons/cm^2. Assuming no saturation behavior, the defect concentration produced by the fast flux in the Stepanov and Aleksandrov irradiation would be approximately .4--meaning roughly one of every two tellurium atoms would be displaced by fast neutron scattering. In this case, the concentration of fast neutron induced defects is so large that these defects, in addition to the thermal neutron induced defects, may have a significant effect on the Mössbauer emission spectrum. Stepanov and Aleksandrov interpret the origin of the isomer shift as a change in the band structure of PbTe which alters the probabilities of s- and p-electron transitions to the conduction band. The surprising fact is that the defects appear to anneal at room temperature, contrary to what had been reported earlier on neutron effects in PbTe.[23-25]

b. Line Width

The apparent single line spectrum for PbTe confirms the absence of quadrupole splitting in cubic structures. The one disturbing feature of the spectrum is the unexpectedly large line width. The measured line widths are approximately 36 percent broader than the predicted line widths. The predicted line widths Γ_{theor} may be as much as 10 percent in error, however, due to the

estimate of the f value and the uncertainty in the measured thickness. In all likelihood the predicted line widths are low estimates.

Part of the broadening arises due to the difference between the line width determined from a "best-fit" Lorentzian and the true width at half maximum of the absorption spectrum. For increasing values of T_A, the Lorentzian line shape differs significantly from the true absorption spectrum. This was readily apparent in observation of the deviation of the "best-fit" Lorentzian from the true absorption spectrum for PbTe. The result showed identical behavior to that described by Bowman, et al.[102] A significant deviation is also confirmed by the relatively large χ^2/N values for the PbTe spectra. The paper by Bowman, et al., indicates that this broadening may amount to several percent. A second contribution to the broadening is the effect of the granular absorbers. Bowman, et al., have shown that the line widths are broadened by the finite grain size of the absorber powder. If it is assumed that the average powder size is 200 mesh (.074 mm diameter), the average resonant thickness of a grain of $PbTe^{125}$ is approximately $\bar{T}_A = 4$. The total average resonant thickness of the $PbTe^{125}$ absorber is $T_A \simeq 2.1$. The results of Bowman, et al., indicate the relative width for such an absorber is $\Gamma_{theor} \simeq 3.4\,\Gamma = 9.35$ mm/sec. This is in good agreement with $\Gamma_{exp} = 9.6$ mm/sec. This estimated line width must be treated with some care since some of the factors are only crude estimates. The point of interest

is the fact that the grain size can provide broadening factors of the order of 30 percent. It appears that this factor easily explains the observed broadening.

Such a large broadening would not be expected in the absorbers with a natural abundance of Te^{125}. Assuming the powders are of identical grain size, the average resonant absorption per grain will decrease approximately in proportion to the ratio of abundances (.07/.95 = .074); so for the natural abundance absorbers $\overline{T}_A \sim .3$. With a total average resonant thickness $T_A \simeq 1$, the broadening is now only about 3 percent.

Other sources of broadening which were discussed in Chapter III include that due to resonant absorption in the source and instrument broadening. Both of these factors contribute relatively little broadening in the measurements reported herein. A final possible source of broadening may arise from inhomogeneous hyperfine structure in the Mössbauer spectrum due to defects, nonstoichiometry, dislocations, grain boundaries, etc. These effects are also expected to be small.

B. Te Metal

1. Results

The Mössbauer spectrum was taken using the Te^{125} source and a single line PbTe absorber enriched to 95 percent in Te^{125}. The measurements again were all taken at liquid nitrogen temperature. The Mössbauer data taken before annealing are shown in Figure IV-2. The data are fit with two Lorentzian

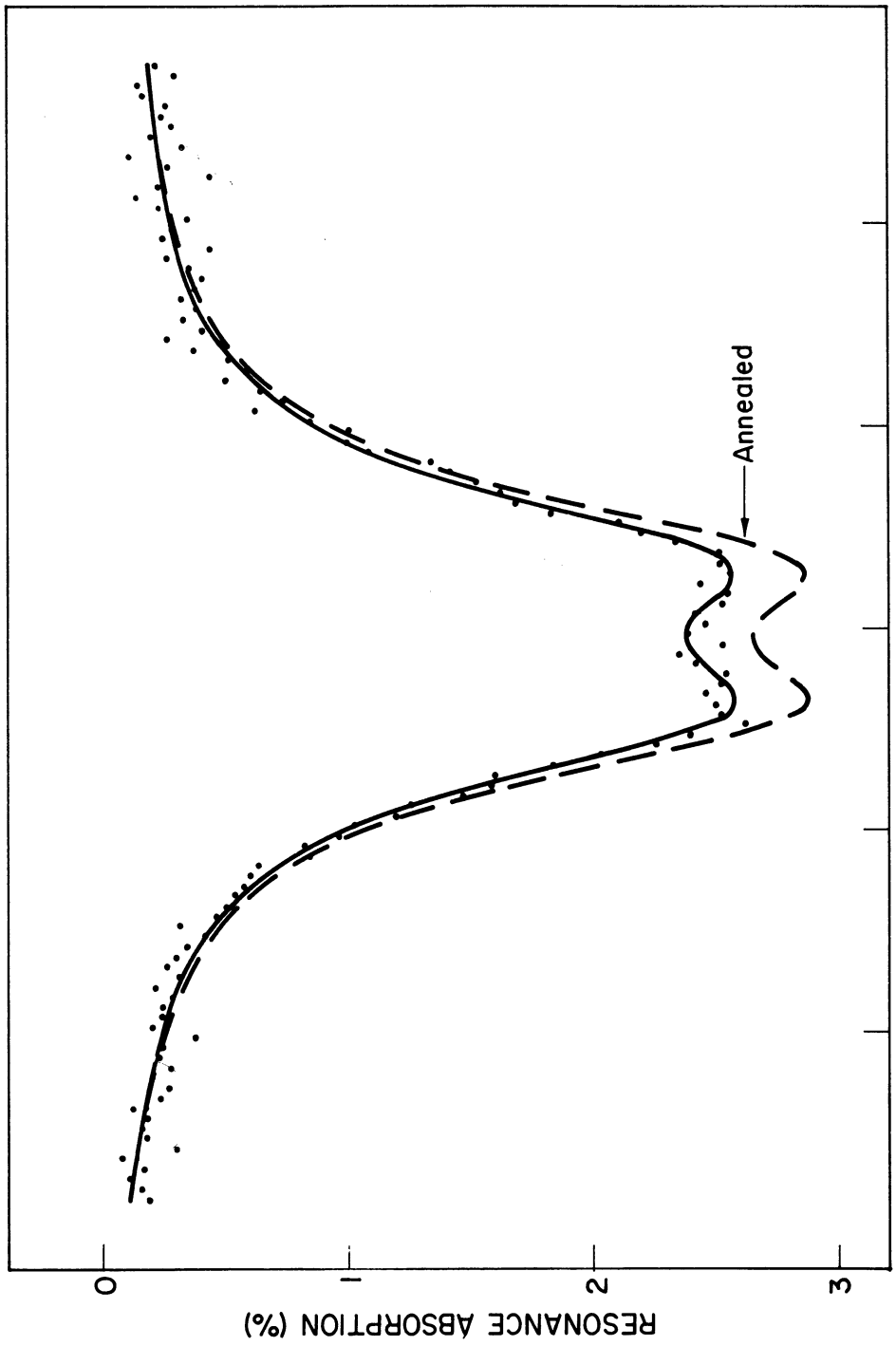

FIGURE IV-2

RESONANCE ABSORPTION SPECTRUM FROM THE Te SOURCE AND PbTe ABSORBER BEFORE AND AFTER ANNEALING

line shapes with variable intensities for each of the lines. The results of the fitting and the subsequent fitting to the spectrum after annealing are shown as the solid and dashed lines, respectively, in Figure IV-2. The fitting parameters for each of the spectra are listed in Table IV-2.

TABLE IV-2

PARAMETERS FROM Te RADIATION EFFECTS DATA

Te Source	Γ_{exp} (mm/sec)	δ (mm/sec)	ΔE_Q (mm/sec)	Resonance* Intensity
Pre-anneal	9.07±.24	-.44±.08	7.51±.14	.0197±.0004
Post-anneal	8.83±.26	-.41±.09	7.35±.15	.0221±.0005

*Average resonance intensity for the two lines, uncorrected for background.

Te Source	Area (mm/sec)	χ^2/N
Pre-anneal	.528	.894
Post-anneal	.573	1.065

The line width, isomer shift, and quadrupole splitting parameters remain constant within the statistical accuracy of the fitting. The resonance intensity increases 10.1 percent upon annealing and the area increases 7.9 percent. Again, for Te metal there appear to be no hyperfine effects attributable to displacements. This is not unexpected in Te though due to the probable self-annealing during irradiation. With rapid annealing

prior to measurement, the initial spectrum should also be characteristic of the "ideal" lattice. In consideration of the annealing, resonance intensity changes are unexpected. This would lead one to suspect that the observed changes in resonance intensity are not real effects but due to uncertainty in the experimental measurement. This will be discussed in detail in this chapter.

2. Discussion of the Data

a. Quadrupole Splitting

The quadrupole splitting in tellurium metal has been analyzed in considerable detail by both Violet, et al.,[30] and Shikazono.[33] The structure of tellurium metal is shown in Figure IV-3(a) and (b). The crystal consists of infinite spiral chains of tellurium atoms. The atoms are covalently bonded in the chains but only weakly bound between chains by electronic and van der Waals forces. The electric field gradient arises principally from bonding between adjacent atoms on the same chain. The covalent bonding scheme results in unbalanced p_x, p_y, and p_z orbitals, which provide a field gradient

$$eq = eq_o\left[\frac{N_x + N_y}{2} - N_z\right]f = eq_o U_p f \quad . \tag{IV.1}$$

N_x, N_y, and N_z are the electron populations in the p_x, p_y, and p_z orbitals; eq_o is the electric field gradient due to a single unbalanced p-electron; and f is the fractional importance of such

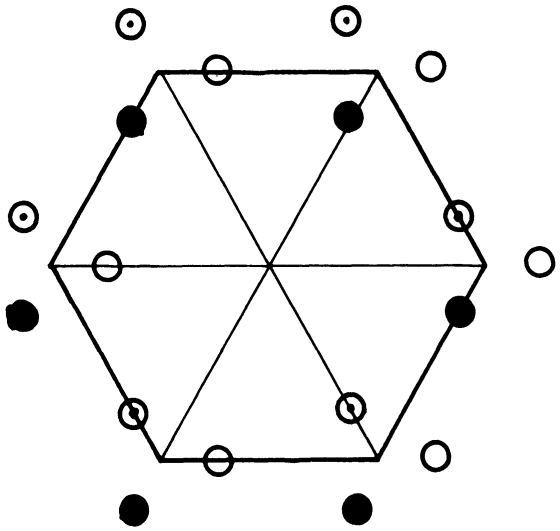

(a)

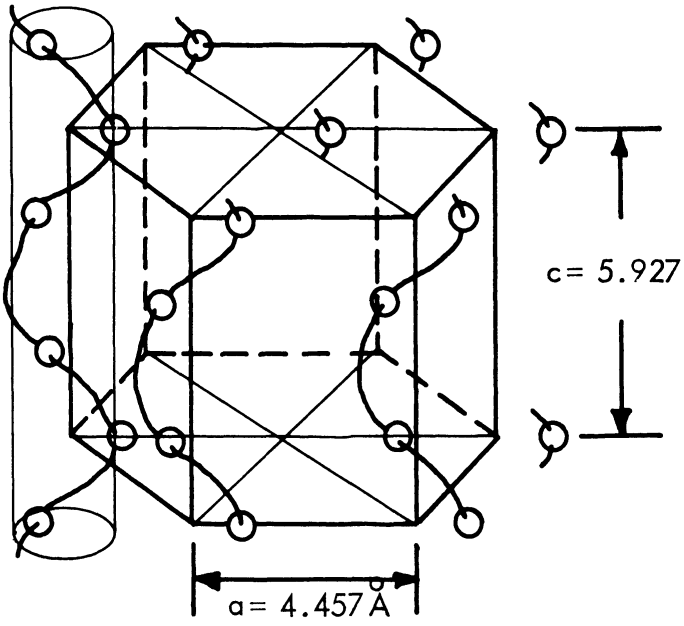

(b)

FIGURE IV-3

(a) PROJECTION OF TELLURIUM CRYSTAL STRUCTURE (DIFFERENTLY SHADED CIRCLES REPRESENT ATOMS AT DIFFERENT LEVELS)

(b) TELLURIUM CRYSTAL STRUCTURE

bonding. The electric field gradient for a single unbalanced p-electron in atomic tellurium calculated by Barnes and Smith[74] is $eq_o = 3.9 \pm .4 \times 10^{16}$ esu. Violet, et al.,[30] used such a formulation and obtained a value $eq = -2.8 \pm .3/.4 \times 10^{16}$ esu for tellurium metal.

The quadrupole splitting, as described in Equation (II.20), is determined by the separation of the two lines in the Mössbauer spectrum shown in Figure IV-2. The average value of the quadrupole splitting obtained from our measurements is $\Delta E_Q = 7.50 \pm .10$ mm/sec. It is in excellent agreement with previous measurements.[30,32-34,36]

b. Asymmetry

In all measurements with tellurium metal, the two lines in the spectrum were slightly asymmetric. The results consistently showed that the intensity of the negative velocity component was a few percent greater than the positive velocity component. However, the difference was of the order of the standard deviation of the fitted intensities. The asymmetry arises from the anisotropy of the f value. The origin of the effect was first discussed by Nicholson and Burns[75] and is known as the Goldanskii effect.[76] For a polycrystalline source such as the tellurium metal used here, the relative intensities of the components of the Mössbauer spectrum are obtained by averaging the angularly dependent emission probabilities over all angles. This is identical to the procedure described earlier for the intensities in the magnetic hyperfine

spectrum. With an isotropic f value, the average over angles involves only the emission probabilities and the ratio of intensities is 1. However, with an anisotropic f value, f is also angularly dependent and the angular average may provide a ratio unequal to 1. An angularly dependent f value would be expected for tellurium metal which has a highly anisotropic crystal structure.

The asymmetry is clearly not in agreement with the result reported by Stepanov, et al.[36] The asymmetry is opposite to and much smaller than their reported values. Violet, et al.,[30] reported no apparent asymmetry within the statistical accuracy of the fitting.

C. TeO_2

1. Results

a. Radiation Effects

The Mössbauer spectrum was taken using the $Te^{125}O_2$ source and a single line H_6TeO_6 absorber with a natural abundance of Te^{125}. The measurements were all made at liquid nitrogen temperature. The Mössbauer data taken before annealing are shown in Figure IV-4. The data are fit with two Lorentzian line shapes with variable line intensities. The results of the fitting and the subsequent fitting to the spectrum taken with the recrystallized source are shown as the solid and dashed lines in Figure IV-4. The fitting parameters for each of the spectra are listed in Table IV-3.

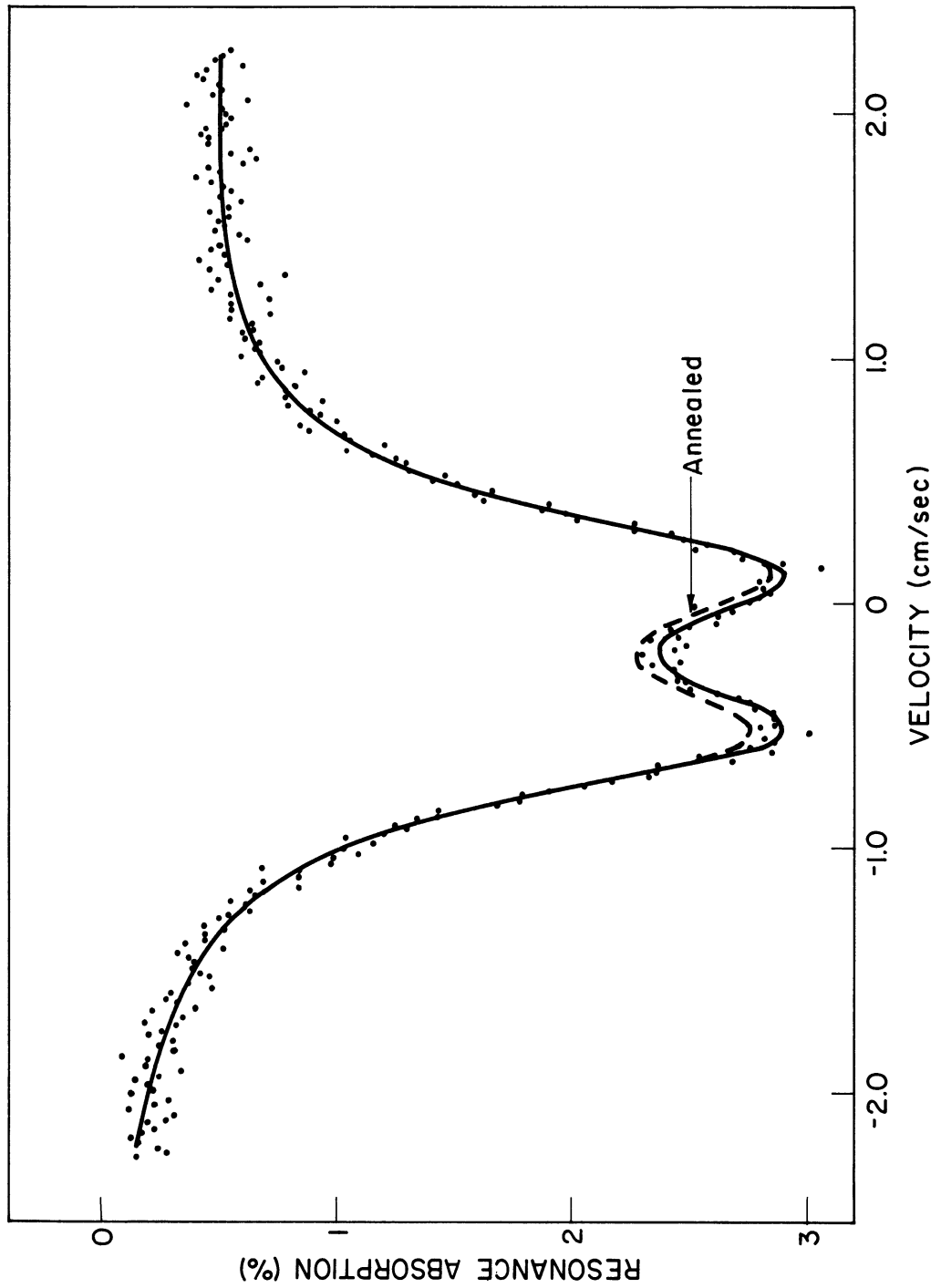

FIGURE IV-4

RESONANCE ABSORPTION SPECTRUM FROM THE TeO_2 SOURCE AND H_6TeO_6 ABSORBER BEFORE AND AFTER THE SOURCE RECRYSTALLIZATION

TABLE IV-3

PARAMETERS FROM TeO_2 RADIATION EFFECTS DATA AND ABSORBER MEASUREMENT

TeO_2 Source	Γ_{exp} (mm/sec)	δ (mm/sec)	ΔE_Q (mm/sec)	Resonance Intensity	Area (mm/sec)	χ^2/N
Pre-anneal	6.42±.12	-1.98±.04	6.72±.11	.0226±.0002	.514	.902
Post-anneal	6.49±.12	-1.99±.04	6.89±.11	.0219±.0002	.505	.791
TeO_2 Absorber	6.79±.28	.62±.16	6.96±.16	.0275±.0009	.540	.967

As in the previous measurement with tellurium metal, the line width, isomer shift, and quadrupole splitting parameters remain constant within the statistical accuracy of the fitting. The line intensity was 3.2 percent less for the recrystallized source spectrum, with the area decreased by 1.8 percent. These results again indicate that no significant hyperfine changes occur which could be attributed to radiation induced displacements. The variation in resonance intensity is opposite to the change seen in both PbTe and Te metal.

b. Absorber Measurement

For an additional measurement of the quadrupole splitting in TeO_2 and to obtain the isomer shift with respect to PbTe, the Mossbauer spectrum was taken using a source of $PbTe^{125}$ and a TeO_2 absorber with a natural abundance of Te^{125}. The measurements were made at liquid nitrogen temperature. The experimental

data are shown in Figure IV-5. The data are fit with a spectrum consisting of two Lorentzian line shapes. The results of the fitting are also shown in Figure IV-5, and the parameters are listed in Table IV-3.

2. Discussion of the Data

The value obtained for the quadrupole splitting is ΔE_Q = 7.0 $\pm$ .2 mm/sec. This result is in good agreement with the value obtained by several authors.[31-33] However, the value $\Delta E_Q \simeq$ 5.6 mm/sec has been quoted by two other authors.[35,36] The difference in the two ranges of ΔE_Q values is much greater than the quoted errors so the difficulty apparently arises from improper characterization of the material. Since there are three presumed structures for TeO_2,[100] some care must be exercised. The origin of the apparent differences has not yet been fully explained.

The crystal structure used in the preceding Mössbauer measurements is that of tetragonal α-TeO_2. The lattice is a distorted variant of the rutile structure. The structure appears to consist of a distorted trigonal bipyramid of oxygen atoms around each tellurium. One equatorial position is occupied by a lone pair of electrons. The average of the four Te-O distances is 2.003Å. There are also two oxygens at an intermediate Te-O distance of 2.89Å.

Unfortunately, the complexity of the structure precludes any simplified analysis of the bonding scheme. Swink and

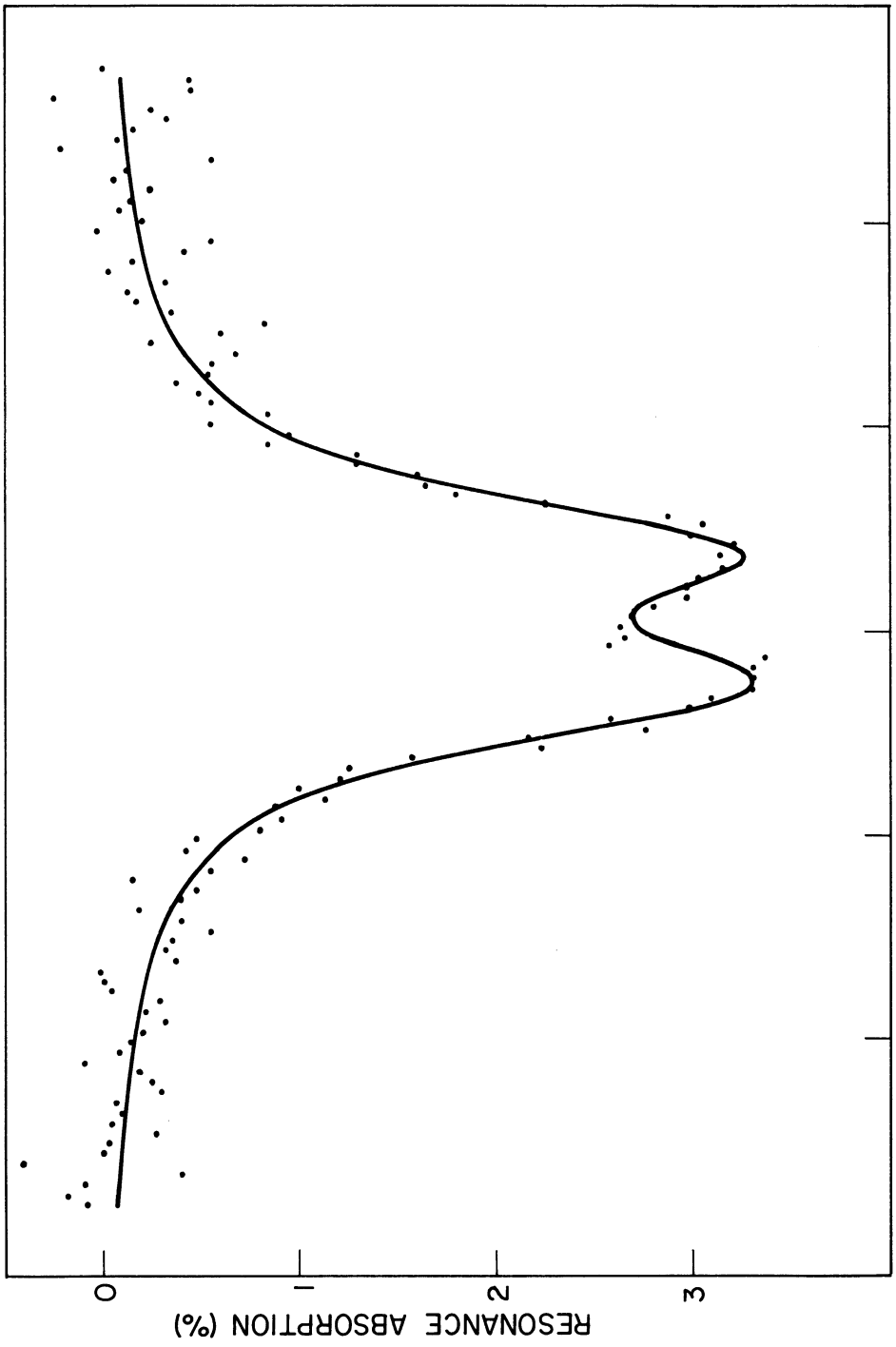

FIGURE IV-5

RESONANCE ABSORPTION SPECTRUM FROM A PbTe SOURCE AND TeO_2 ABSORBER

Carpenter[101] have indicated that the nearest neighbor axial and equatorial bonds probably involve different hybridizations. The origin of the intermediate length Te-O bonding is uncertain, and Te-Te bonds have also been postulated for the structure.[68] The possible existence of an electric field gradient at the tellurium site is obvious. Until the bonding scheme is clarified, though, an estimate of the field gradient is not possible.

D. Discussion of the Radiation Effects Measurements

1. Resonant Intensity

Summarizing the results of the radiation effects measurements, there appear to be no measurable changes in the Mössbauer hyperfine spectra in either PbTe, Te metal, or TeO_2. The only change observed in the measurements was a variation in the resonant intensity. However, after careful analysis, the variation does not appear to be due to a real change in the recoil-free fraction; rather, the variations may be considered as deviations within the experimental accuracy of the measurement. The measured changes in resonant intensity (3 to 10 percent) were certainly greater than the statistical error in the computer fit intensity ($\sim$ 1 percent); however, other experimentally introduced errors are considerably larger than the statistical error.

The deviations in the experimental measurement of the resonant intensity arise from both the lack of stability in the detection system during the course of a run and variations

in the reproducibility of experimental conditions between runs. To examine the lack of stability in the electronics during a run, the data were periodically analyzed during the course of the run. In the preceding PbTe measurement, the intensities, uncorrected for background, were observed to have a considerable variation over the course of the run. On the basis of these observed variations, the error bars on the measured resonant intensity are ± 2.2 percent for the unannealed run and ± 4.1 percent for the annealed run.

These variations arise principally from changes in the gamma ray detection system. Since the runs were usually of one-week duration, this is not wholly unexpected. Any part of the system which would cause gain drifts, gain changes, or noise variations would vary the signal-to-noise ratio in the escape peak and consequently affect the measured resonant intensity. Although changes in high voltage, amplification, and discriminator setting would affect the signal-to-noise ratio, no noticeable changes were encountered. The most likely source appeared to be the proportional counter and preamplifier. During the course of the measurements, difficulties were encountered with both noise from the preamplifier and gain variations and count rate fluctuations in the proportional counter. The signal gain and count rate fluctuations do not appear to be a unique problem with our proportional counters since the same effects have been encountered by other experimenters.* This appears to severely limit the use of

*R. D. Taylor, private communication.

gas-filled proportional counters for accurate measurement of Mössbauer resonant intensities.

Careful attempts were made to exactly reproduce the experimental conditions between the pre-anneal and post-anneal Mössbauer runs. Some differences were unavoidable, however. Variations in the signal-to-noise ratio no doubt occurred in resetting the single channel analyzer window. Analysis of the total gamma ray spectrum and escape peak spectrum taken before each PbTe run indicated a variation of approximately 1 percent in the signal-to-noise ratio. Since the determination of the signal-to-noise ratio is not extremely accurate, the reasonably close agreement may be fortuitous, and the error may even be larger.

The source temperature was continuously monitored and recorded during the course of an experiment. However, it is not possible to determine the actual temperature better than to within a few degrees from the recorder trace. In addition, the temperature was not controlled, so variations of the order of $9^{o}K$ occurred during a filling cycle. A variation in the average temperature would affect the measured f value. An average temperature variation of $1^{o}K$ would change the resonant intensity by 1.4 percent.

From the foregoing analysis, the experimental uncertainty in the measured resonant intensity could be of the same order as the measured differences. This is further confirmed by the fact that the effect is seen in Te metal where it is not expected, and variations of the same magnitude occur in other non-radiation effects measurements.

2. Reasons for the Observed Results

The presence of radiation induced changes of the order of a few percent in the Mössbauer recoil-free fraction cannot be excluded on the basis of the present measurements. There are a number of reasons, however, why the effects on the recoil-free fraction and the hyperfine spectra may be very small. Unfortunately, the data currently available is not satisfactory to fully confirm or eliminate any of the explanations. The explanations are the following.

a. Recoil Energy

The mean recoil energy of the atom after prompt gamma ray emission may not be sufficient to displace the atom from the normal lattice site. The value obtained in Chapter II was based on several assumptions regarding the prompt gamma ray spectrum, time and angular correlation of the gamma rays, and the displacement energy. In reality, the capture gamma ray spectrum may be much more complex than is assumed in the estimate of the recoil energy. Since the mean recoil energy estimated in Chapter II was only of the order of $2E_d$, a more complex capture gamma ray spectrum may yield a mean recoil energy less than the displacement energy E_d. Then only a small fraction of atoms would be displaced from the normal lattice site. The resultant Mössbauer pattern would then be characteristic of the "ideal" lattice, with only a small "background" contribution due to displaced atom sites. Since the statistics of the accummulated

Mössbauer data were usually of the order of ±.1 percent, any fraction of sites less than about 5 percent of the total would not provide a Mössbauer line distinguishable from the statistical background. In fact, even a fraction greater than 5 percent might not provide a distinguishable line if the defect sites are characterized by widely differing hyperfine interactions.

This uncertainty in recoil energy cannot be resolved without a measurement of the Te^{125} prompt gamma ray spectrum. A measurement of the Te^{125} capture gamma ray spectrum was attempted by Clifton,[91] but the effort was fruitless.

The fact that thermal neutron effects are observed in PbTe using other measurement techniques may be due to displacements produced by neutron capture in other isotopes of tellurium. The probability of displacements being produced due to neutron capture in the stable odd-n isotopes of tellurium (Te^{123} and Te^{125}) is certainly greater due to the approximately 2 Mev pairing energy increase in the binding energy. More favorable capture gamma ray spectra may also occur in the other tellurium isotopes.

b. Replacement Collisions

The final environment of the displaced atom may be a normal lattice site. Dederichs, Lehmann, and Wegener[11] have calculated the replacement probability for a primary recoiling atom. Assuming hard-core interactions, the probability P(E)

that a primary atom of energy E replaces a lattice atom during slowing down is given as

$$P(E) = \begin{cases} \ln E/E_d & E_d \leq E \leq 2E_d \\ \ln 2 & 2E_d \leq E \end{cases} \qquad \text{(IV.2)}$$

Assuming the values E = 58 ev and E_d = 25 ev used in Chapter II, the probability of replacement for the recoiling tellurium atom is P = ln 2 $\simeq$ .7. Thus, a large fraction of the recoiling atoms arrive at a normal lattice site.

However, even though these atoms are in a normal lattice site, the characteristic environment may not be that of the "ideal" lattice. First, since the recoil energies are low, the replaced atom probably remains very near the replacement site. Likewise, the initial site of the recoiling atom (now a vacancy) is probably also near the replacement site. Thus, although the primary tellurium atom may not be in the defect state, it is probably a near-neighbor to a defect. Second, the recoiling atom may replace the lead or oxygen in PbTe and TeO_2 rather than the tellurium. The replaced atom would then act as a substitutional impurity. This site would also be different from the normal tellurium site. In both of these cases, the characteristic environment should be different than that in the "ideal" lattice. So even though the replacement probability is large, the characteristic Mössbauer spectrum should still be altered.

c. Defect Annealing

Defect annealing may occur to restore the defects to normal lattice environments. This has been discussed in some detail in Chapter II so it will not be repeated here. The gist of the discussion was that defects are probably stable in PbTe, unstable in Te, and uncertain in TeO_2.

d. Hyperfine Interactions

The hyperfine interactions characteristic of the defect environment may be too small to produce resolvable changes in the Mössbauer spectrum. As discussed in Chapter II, isomer shift changes are expected to be very small compared to the experimental line width. Since the s-electron density could both increase and decrease in different defect environments, the sum over different defect configurations could easily produce an averaged spectrum which is apparently unshifted.

The rough calculation of the electric field gradient in Chapter II indicates that it should be possible to see quadrupole splitting in the Mössbauer spectrum for atoms in a defect environment. This cannot be further substantiated, however, without a more rigorous calculation of the electric field gradient involving the defect atom bonding. Evidence would indicate that defect atoms in noncubic environments (such as expected in PbTe) should produce quadrupole splitting which would at least broaden the characteristic spectrum.

It is unfortunate that more specific conclusions cannot be drawn from the present measurements. However, the present state of knowledge makes it impossible to conclusively confirm or deny any of the preceding observations.

CHAPTER V.

EXPERIMENTAL RESULTS OF MÖSSBAUER EFFECT MEASUREMENTS IN OTHER TELLURIUM COMPOUNDS

Mössbauer effect measurements were made of several additional compounds of tellurium. The interest here was solely in the information obtainable from the Mössbauer hyperfine structure. The measurements were all made with a single line source of $PbTe^{125}$. Both the source and absorber were at liquid nitrogen temperature in all of the measurements. The results for the various materials are described below.

A. $CuCr_2Te_4$

The ferromagnetic spinel $CuCr_2Te_4$ appeared to be an excellent candidate for the detection of magnetic hyperfine structure in the Te^{125} Mössbauer spectrum. This spinel is one of the group of chromium chalcogenide spinels which have shown an anomalous ferromagnetic coupling of the Cr spins.[80-82]

The magnetic hyperfine field which would be measured in our experiment is not the field at the magnetic Cr cation site, but rather the field at the nonmagnetic Te anion site. The Te^{2-} ion would not normally be expected to have a magnetic hyperfine field at the nucleus due to the completely filled 5s and 5p electron shells. However, the ferromagnetically coupled Cr spins can act to spin polarize or unpair the filled tellurium electron shells. This unpairing leads to a net spin density at the nucleus and a subsequent magnetic

hyperfine field through Equation (II.28). This is often referred to as a transferred hyperfine field.

Most spinels which have been studied have had magnetic properties dominated by antiferromagnetic interactions. The Cr spinels have been prepared with all of the chalcogenides O, S, Se, and Te and the metallic cations Cu, Ag, Zn, Cd, and Hg. A group of these chromium chalcogenide spinels, including $CuCr_2Te_4$, have magnetic properties dominated by strong ferromagnetic interactions.[80-82] For all metallic cations except Cu, the attempts to produce the Te anion spinel have been unsuccessful.[79,80] Since none of the other chalcogenides are amenable to Mössbauer study, this compound represents a rather unique opportunity for studying transferred hyperfine fields in the ferromagnetic spinels.

The compound was first prepared by Hahn, et al.,[78] in 1956. The magnetic properties were studied by Lotgering and reported at the 1964 Magnetism Conference.[79] Colominas[70] very recently performed x-ray and neutron diffraction measurements on the material to ascertain the spin configuration.

1. Results

Mössbauer measurements were taken using a single line $PbTe^{125}$ source and a $CuCr_2Te_4$ absorber with a natural abundance of Te^{125}. Measurements were made with two different absorber thicknesses. The spectra for both absorbers consisted of two rather broad lines. The experimental data for the thicker absorber is shown in Figure V-1.

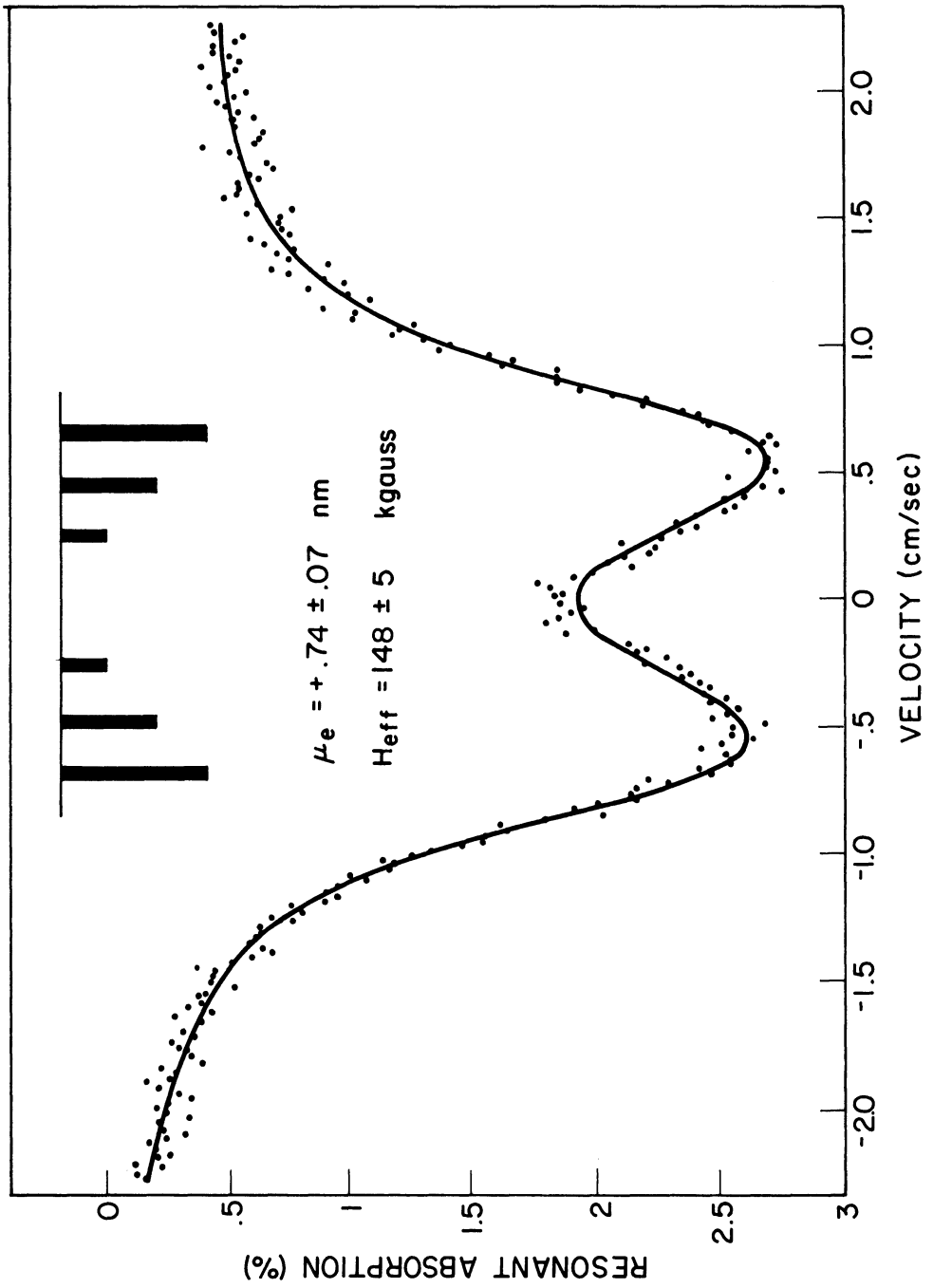

FIGURE V-1

RESONANCE ABSORPTION SPECTRUM FROM A PbTe SOURCE AND $CuCr_2Te_4$ ABSORBER (53.5 mg/cm^2)

a. Interpretation of Observed Spectrum

At first appearance, the spectrum seems to display two lines characteristic of a large quadrupole splitting. However, closer analysis indicates that the structure is due to a partially resolved magnetic hyperfine splitting rather than electric quadrupole splitting. The spectrum was fit with the following theoretical curves: First, a spectrum consisting of two Lorentzian line shapes with identical widths and varying intensities; and second, six Lorentzian line shapes with intensities constrained to the ideal intensity ratio for a powder absorber. Both the ratio of the excited state to ground state g value and the effective internal hyperfine field were used as variables for the six line fit. The smooth curve shown in Figure V-1 is the best fit with a six line spectrum. The bars denote the location and intensity of the six lines.

On the basis of the curve fitting, the two line spectrum was ruled out for two reasons: First, the χ^2/N value for the fitting with two lines is greater than that for the six line fit; and second, the line width obtained with the two line fit is broader than the predicted line width. As mentioned in Appendix C, χ^2/N is a measure of the "goodness of fit." The smaller χ^2/N, the better the fit. The values obtained in the fitting were $\chi^2/N)_{2L} = 1.32$ and $\chi^2/N)_{6L} = 1.01$. The line width obtained in the two line fit was $\Gamma_{exp} = 8.68$ mm/sec. This is 36 percent broader than the predicted line width $\Gamma_{theor} =$ 6.4 mm/sec corrected for absorber broadening. The line width

for the six line fit is Γ_{exp} = 6.83 mm/sec, which is in agreement with the predicted line width.

The third consideration ruling out electric quadrupole splitting as the origin of the hyperfine structure is the magnitude of the splitting. For a two line fit, the quadrupole splitting is ΔE_Q = 10.75 mm/sec. Using the quadrupole moment Q = .20 barns, the field gradient needed to give such a splitting is eq = 4.3 x 10^{16} esu. This is even greater than the field gradient from a single unbalanced p-electron, which as mentioned earlier is eq_o = 3.9 x 10^{16} esu.(74) If the tellurium occurred as purely ionic Te^{2-}, the electronic structure would be $(5s)^2(5p)^6$ with no unbalanced p-electrons. For any intermediate covalently bonded structure, such as $(5s)^2(5p)^4$, the number of unbalanced p-electrons, as defined in Equation (IV.1), is at most one. For the reasons described earlier, lattice field gradients would certainly be much less than this value. On the basis of these arguments, no possible bonding mechanism would contribute a field gradient as large as that determined above. The conclusion is that the origin of the hyperfine structure must be in the magnetic interaction.

b. Hyperfine Interaction Parameters

The fitting parameters obtained from the six line fit are listed in Table V-1 for both of the absorbers. In the final fitting, a quadrupole splitting parameter was also included in the analysis. The combined effect of the magnetic field

TABLE V-1

PARAMETERS OBTAINED FROM SIX LINE FIT TO RESONANCE ABSORPTION SPECTRA OF $CuCr_2Te_4$

Absorber	Γ_{exp} (mm/sec)	δ (mm/sec)	$\mu_g H_{eff}$ (mm/sec)	g_e/g_q	ΔE_Q (mm/sec)	Resonance* Intensity
$CuCr_2Te_4$-1	6.75±.19	-.05±.05	3.45±.20	-.261±.046	-.00±.30	.00282±.00010
$CuCr_2Te_4$-2	6.83±.21	-.01±.03	3.55±.11	-.293±.021	-.77±.33	.00437±.00007

Continued

Absorber	Area (mm/sec)	χ^2/N
$CuCr_2Te_4$-1	.298	.966
$CuCr_2Te_4$-2	.580	.991

*Actual resonance intensity for each line is obtained by multiplying by the appropriate relative intensity factor (3, 2, or 1).

and electric field gradient on the nuclear levels can be quite complicated. However, with some simplifying assumptions, the level scheme can be easily interpreted. It was assumed that the magnetic field and electric field gradient principal axes coincided and that there was axial symmetry for the electric field gradient ($\eta = 0$). It was also assumed that $\mu H_{eff} \gg e^2qQ$ so that the electric quadrupole interaction merely acted as a perturbation to the magnetic substates. For the small quadrupole splitting obtained in the actual fitting, these assumptions are not unreasonable.

Averaging the results obtained from the two measurements, the g factor ratio and effective internal hyperfine field were determined to be

$$g_e/g_g = -.28 \pm .03 \qquad (V.1)$$

and

$$H_{eff} = 148 \pm 5 \text{ kgauss.} \qquad (V.2)$$

Using the ground state nuclear moment $\mu g = -.8872$ nm determined by nuclear magnetic resonance measurement[57] and the measured g factor ratio, the excited state nuclear moment is

$$\mu_e = +.74 \pm .07 \text{ nm.} \qquad (V.3)$$

This result is in good agreement with the value of $\mu_e \simeq +.7$ nm estimated by Shikazono.[33]

2. Interpretation of the Data

a. Crystal Structure and Spin Configuration

An understanding of the origin of the effective field (Equation (V.2)) requires a more detailed study of the magnetic properties of $CuCr_2Te_4$. The spinels have the crystal structure shown in Figure V-2. The structure can be visualized as a close-packed array of Te atoms, into the interstices of which the metal ions are packed. There are two types of voids: the tetrahedral, or A sites, of which there are two per Te atom; and the octahedral, or B sites, of which there is one per Te atom. Since there are only three metal ions per molecule, only one-quarter of the sites are occupied.

One of the points of interest is how the metal ions occupy the A and B sites. This can be partially understood from the magnetic data. Lotgering[79] determined that the material showed spontaneous magnetization with Curie temperature $T_C = 365^oK$. At high temperature, the susceptibility followed a Curie-Weiss law with paramagnetic Curie temperature $\Theta = 400^oK$ and molar Curie constant Cm = 2.90. The saturated moment at 4^oK is $4.93\ \mu_B$.

The Cr^{3+} ions have the electronic configuration $3d^3$. When a transition metal ion is subjected to an octahedral crystalline field, the d energy levels lose their degeneracy and are split

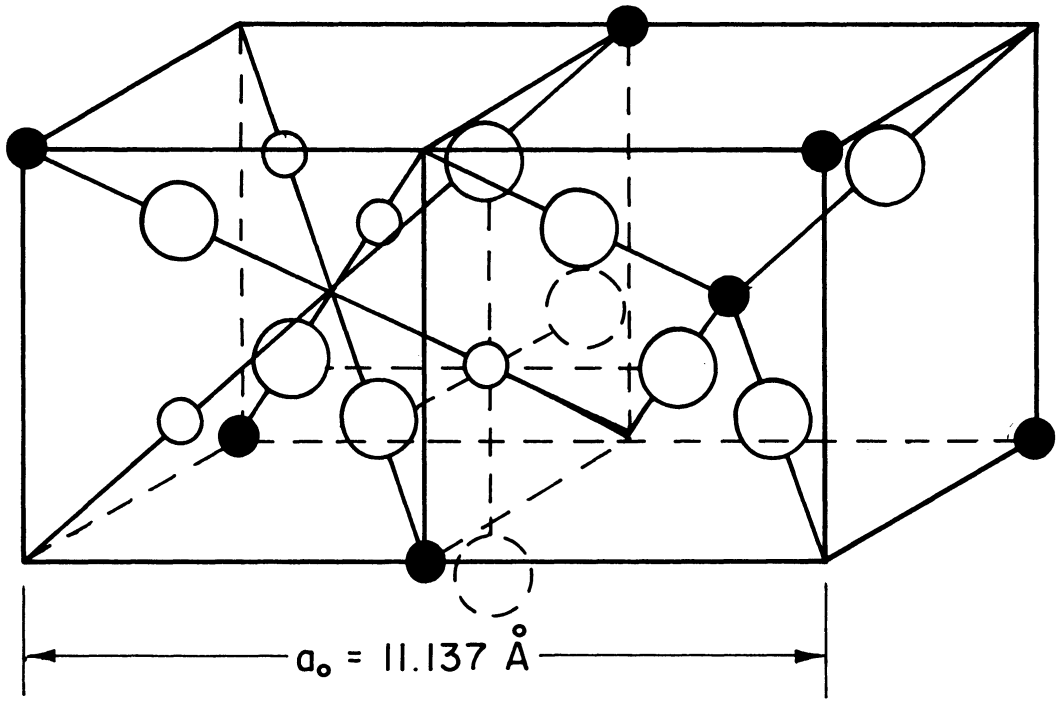

● Tetrahedrally Coordinated Cu^+ (A site)
○ Octahedrally Coordinated Cr^{3+} (B site)
◯ Tellurium ion

FIGURE V-2

CRYSTAL STRUCTURE OF $CuCr_2Te_4$ SPINEL

into a lower energy triplet, denoted by t_{2g}, and an upper energy doublet, denoted by e_g. The t_{2g} triplet contains the orbitals of the type d_{xy}, d_{yz}, and d_{zx}. The e_g doublet contains the orbitals of the type $d_{x^2-y^2}$ and d_{z^2}. The Cr^{3+} ion has a strong preference for octahedral sites since the three 3d electrons are stabilized in the t_{2g} orbitals. The Cu^{2+} ions have the electronic configuration $3d^9$. Hence Cu^{2+} has a single hole in the 3d shell.

Assuming that the Cr ions occupy the octahedral B sites in $CuCr_2Te_4$, the following spin configurations were proposed to explain the measured saturated moment ($\sim 5\,\mu_B$):

I. $Cu^{2+} \mid Cr_2^{3+} \mid Te_4$ with ferrimagnetic spin ordering.

II. $Cu^{+} \mid Cr^{3+}\ Cr^{4+} \mid Te_4$ with ferromagnetic ordering on the B sites.

The fact that $T_C \simeq \theta$ eliminates the possibility of ferrimagnetic ordering as in configuration I. The Curie constant Cm = 2.88 calculated for II is also in better agreement with the experimental value.

Colominas[70] recently reported neutron diffraction studies of $CuCr_2Te_4$ which indicated that neither configuration I nor II was correct. To fit the neutron diffraction data, the B sites were divided into two distinct sublattices. The moments on each of the B sublattices and the A sites were allowed to vary independently. The data were best fit with equal Cr moments on each of the B sublattices and zero moment at the A site. The magnitude of the moments indicates that all Cr is present

as Cr^{3+} and the Cu as Cu^{+}. However, the predicted saturated moment for this model is $6\,\mu_B$. This does not agree with the measured value of $4.93\,\mu_B$. This anomalous moment can be explained by assuming a nonlocalized moment of $\sim 1\,\mu_B$ anti-parallel to the Cr moments. A cause for this deviation from the theoretical value may be a spiral magnetic configuration.(80)

b. Superexchange Interactions

Since the origin of the hyperfine field may be intimately related to the ferromagnetic coupling of the Cr^{3+} spins, it is of importance to investigate the exchange interactions. The exchange interactions in ferromagnetic spinels were investigated by Baltzer, et al.(80) These authors assumed a Heisenberg spin Hamiltonian of the form

$$\mathcal{H} = -2J\sum_{ij} \underline{S}_i \cdot \underline{S}_j - 2K\sum_{ik} \underline{S}_i \cdot \underline{S}_k - g\mu_o H_z \sum_i S_{iz} \quad . \tag{V.4}$$

The sum over ij includes the six nearest-neighbor pairs, and the sum over ik includes the 30 next-nearest-neighbor interactions. The interaction between nearest-neighbor pairs was assumed to be a 90° superexchange of the type Cr^{3+} - Te - Cr^{3+}. This interaction is referred to as a superexchange interaction since the coupling does not involve direct exchange between the cations. The cations are instead coupled through the intermediary anion. The 90° refers to the Cr - Te - Cr bonding angle. For octahedrally coordinated Cr^{3+}, this exchange interaction is ferromagnetic,(83) so J is positive. Direct Cr - Cr

exchange is excluded due to the large separation of the ions. This is consistent with the lack of metallic conductivity in the ferromagnetic spinels. The next-nearest-neighbor interaction is assumed to be of the type Cr^{3+} - Te - Cu - Te - Cr^{3+}. Baltzer, et al.,[80] correlated the high temperature susceptibility with the Curie temperature and determined that the long range exchange interaction is antiferromagnetic, or K is negative.

In a paper by Kanamori[83] various mechanisms are discussed to explain the superexchange interaction. As mentioned earlier, in octahedral symmetry the three t_{2g} orbitals lie lower in energy than the two e_g orbitals and are singly occupied. The 90° ferromagnetic exchange interaction between Cr^{3+} ions can be explained by the symmetry relationships between the Cr^{3+} 3d orbitals and the Te^{2-} 5p orbitals. The bonding and exchange interactions can most easily be understood on the basis of the mechanism proposed by Anderson.[84] Anderson's proposal involves a virtual transfer of an electron from the $5p_\sigma$ orbitals to the neighboring Cr^{3+}. The unpaired spin left on the Te^{2-} couples with the spin of the other neighboring Cr^{3+} through exchange interaction. For the 90° Cr^{3+} - Te - Cr^{3+} interaction, an electron is transferred from the $5p_\sigma$ orbital of Te^{2-} to the nonorthogonal unoccupied e_g orbital of Cr^{3+}. On the basis of Hund's rule, the spin of the $5p_\sigma$ electron transferred is parallel to the t_{2g} spins of the cation. The $5p_\sigma$ spin remaining on the Te^{2-} is antiparallel to the t_{2g} spins of the Cr ion.

This antiparallel $5p_\sigma$ spin is exchange coupled to the t_{2g}' spins of the Cr^{3+} ion at 90°. Since the $5p_\sigma$ orbital is nonorthogonal to the t_{2g}' orbital, the exchange interaction is negative. The t_{2g}' spins are then coupled antiferromagnetically to the unpaired $5p_\sigma$ spin. This results in parallel or ferromagnetic coupling of the t_{2g} and t_{2g}' spins. The spins are identically coupled through the interaction involving $5p_\sigma'$ and t_{2g}' orbitals.

The bonding and exchange interactions involving the $5p_\sigma$ - e_g' orbitals and the $5p_\sigma'$ - e_g orbitals also predict ferromagnetic coupling of the cation spins.(83)

c. Transferred Hyperfine Field

As discussed in Chapter II, a purely ionic Te^{2-} configuration would not be expected to give rise to an effective hyperfine field. The spin paired 5s and 5p electrons would yield no contribution to H_{eff} through Equation (II.28). In the ferromagnetic spinel $CuCr_2Te_4$ both covalency and the exchange interaction could lead to an unpairing of the 5s electrons. Like the $5p_\sigma$ orbital, the Te 5s orbital can mix with the Cr e_g orbitals. In this case a partial covalent bond can be formed between the Te 5s and Cr e_g orbitals. Due to the ferromagnetic exchange between orthogonal orbitals (Hund's rule), the 5s spin transferred must be parallel to the t_{2g} spins. The net 5s spin density left at the tellurium nucleus must then be negative (antiparallel to the Cr t_{2g} spin).

The tellurium 5s electron spin polarization can also arise through the ferromagnetic exchange interaction of the 5s spins with the t_{2g} spins. Due to the different exchange interaction for the parallel and antiparallel 5s spins, the radial wave functions are no longer the same. For ferromagnetic exchange coupling, the parallel 5s spin has a lower potential energy in the vicinity of the t_{2g} spins. The parallel 5s spin is then "attracted" outward by the ferromagnetically coupled Cr^{3+} ions. With the radial expansion of the parallel 5s spin, a region of negative (antiparallel) spin density is left at the nucleus.

The hyperfine field due to covalency and exchange effects has been discussed by Watson and Freeman[59] for MnF_2. As described above, the covalency and exchange effects provide an unpairing of the tellurium 5s electrons (presumably 5s, although other orbitals may provide a small contribution). The unpaired tellurium 5s electrons provide an effective hyperfine field through the Fermi contact interaction in Equation (II.28). Both of the mechanisms described above provide a negative (antiparallel to Cr^{3+} spins) spin density at the Te nucleus. This would lead to a positive contact hyperfine field.* The spin polarization need not be large to provide an effective field of H_{eff} = 148 gauss as in $CuCr_2Te_4$. Although the effective field has not been calculated for a single unpaired 5s electron in tellurium, indications are that it is of the order of 2.0 Mgauss.[86] A polarization of only 7.5 percent would then produce a field of the right magnitude.

*Internal fields are defined as positive if parallel to an external magnetizing field. The magnetic moment of the 3d electrons orients parallel to an external magnetic field which orients the 3d spins antiparallel to the external field.

3. Magnetized Absorber Measurement

The fact that the hyperfine structure in $CuCr_2Te_4$ is magnetic in origin can be convincingly demonstrated by observing the hyperfine spectrum with oriented absorbers. As discussed in Chapter II, the relative intensities of the hyperfine components can be varied by orienting the spin axis with respect to the gamma ray beam. Several attempts were made to magnetize the absorber both parallel and perpendicular to the gamma ray beam. The absorber magnetization was done using either small permanent magnets or a solenoid coil with magnetic fields which varied from 300-1300 oersteds.

Unfortunately, the magnetic fields were not sufficient to saturate the absorber magnetic moment. The result is a Mössbauer hyperfine pattern with intensities which are averaged with an angular distribution of domain orientations characteristic of a partially magnetized absorber. The angular distribution function will be intermediate to the constant distribution characteristic of a random, nonmagnetized sample and the delta function characteristic of a fully magnetized sample. The magnetization of $CuCr_2Te_4$ at liquid nitrogen temperature has not been measured as a function of the applied field, so the degree of magnetization in these experiments is not know.

As shown in Figure V-3, the difference in shape of the spectra is not considerable even in the limit of complete alignment perpendicular or parallel to the gamma ray beam. The best possibility appears to be in using magnetization parallel to

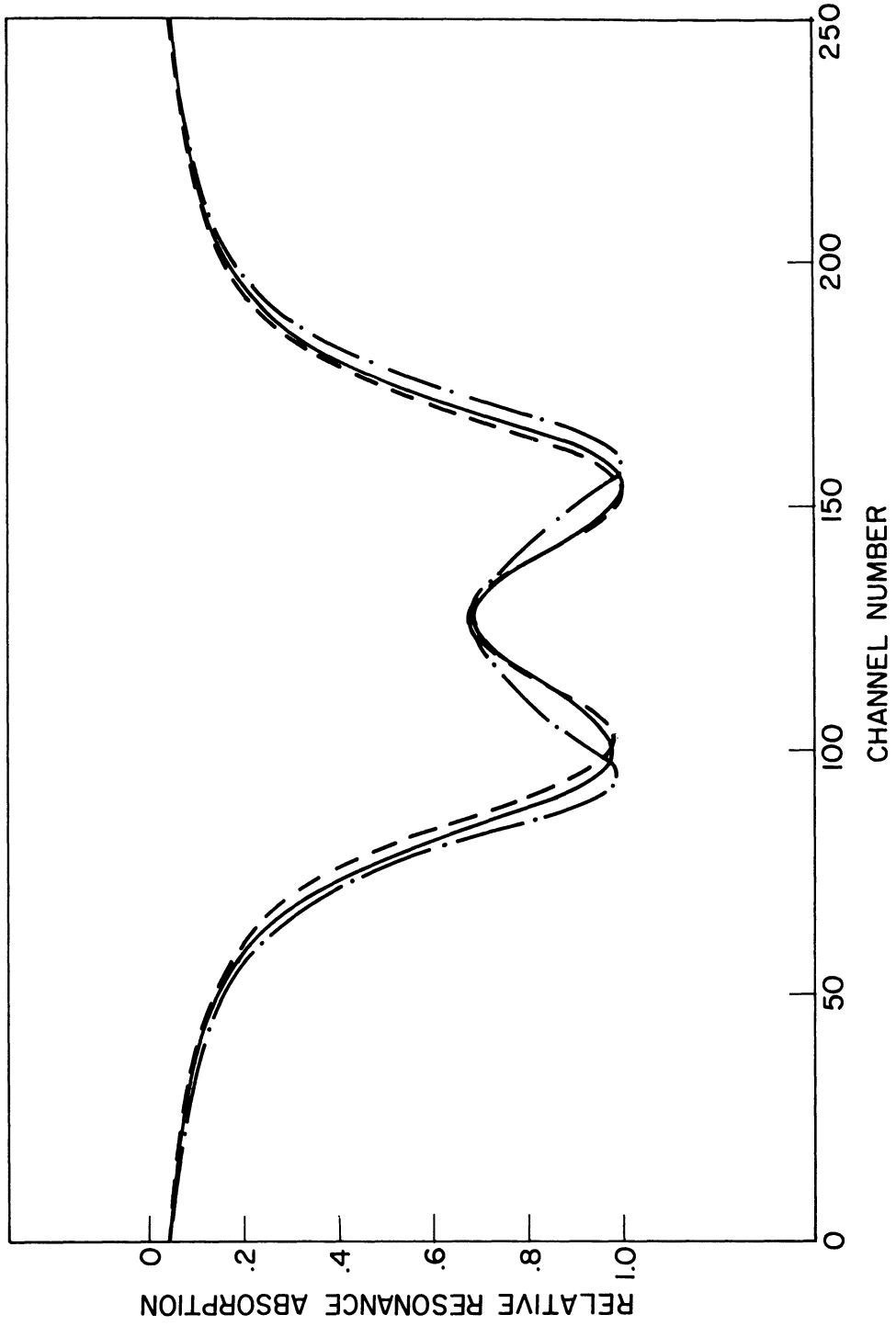

FIGURE V-3

PREDICTED MAGNETIC HYPERFINE SPECTRA IN CuCr2Te4 WITH ORIENTED INTERNAL FIELDS (——— RANDOMLY ORIENTED (MEASURED SPECTRUM), — — — PERPENDICULAR TO GAMMA-RAY BEAM, ——·—— PARALLEL TO GAMMA-RAY BEAM)

the gamma ray beam. The spectrum measurements with partially magnetized absorbers showed only slight changes with respect to the nonmagnetized absorber. This would indicate that the absorbers were only partially magnetized.

B. MnTe

Other interesting magnetic compounds of tellurium are formed with the transition metals. These include MnTe and CrTe, both of which have the NiAs crystal structure. The coupling of the transition metals in these compounds is antiferromagnetic and ferromagnetic, respectively. The MnTe results are discussed in this section and the CrTe results follow.

Some disagreement has arisen over the presence or lack of hyperfine splitting in the Mössbauer spectrum of MnTe. Shikazono[33] originally reported that the spectrum of MnTe taken at liquid nitrogen temperature consisted of a single line with no apparent broadening due to hyperfine interactions. In similar measurements at liquid nitrogen temperature, Violet and Booth [31] observed a quadrupole split spectrum with ΔE_Q = 3 ± 1 mm/sec. Shikazono attributed the lack of quadrupole splitting to a nearly ionic Mn^{2+} - Te^{2-} crystal with a filled 5p shell on the tellurium and a negligibly small lattice field gradient. Violet contends on the basis of the observed splitting that either the lattice field gradient is not negligibly small or there is covalent bonding in MnTe. It was hoped that measurements with good stoichiometric MnTe would help to clarify the disagreement.

1. Results

The Mössbauer spectrum was taken using a single line source of $PbTe^{125}$ and an absorber of MnTe with a natural abundance of Te^{125}. The experimental results are shown in Figure V-4. The Mössbauer spectrum was fit with a single Lorentzian, which is also shown in Figure V-4. The fitting parameters are listed in Table V-2.

It is apparent from the large difference between the theoretical and experimental line widths (Γ_{theor} = 5.9 mm/sec and Γ_{exp} = 7.66 mm/sec) that there is hyperfine splitting in MnTe. No resolved quadrupole splitting is observed, however. If it is assumed that the broadening is due solely to quadrupole splitting, the resultant splitting is approximately $\Delta E_Q \simeq$ 1.7 mm/sec. This is smaller than the value quoted by Violet and Booth, but the difference is still within the maximum error limits.

The thickness of the absorbers used in this experiment and Violet and Booth's experiments were nearly identical. Since the line widths are nearly identical, the resolution should be nearly the same.* In such event, the hyperfine splitting in the present measurement would indeed appear to be smaller.

2. Discussion of the Data

MnTe has the NiAs crystal structure. As shown in Figure V-5, this structure consists of a hexagonal close-packed Te anion sublattice with Mn cations in the octahedral interstices.

*This is valid only if source broadening and experimental broadening are assumed negligible.

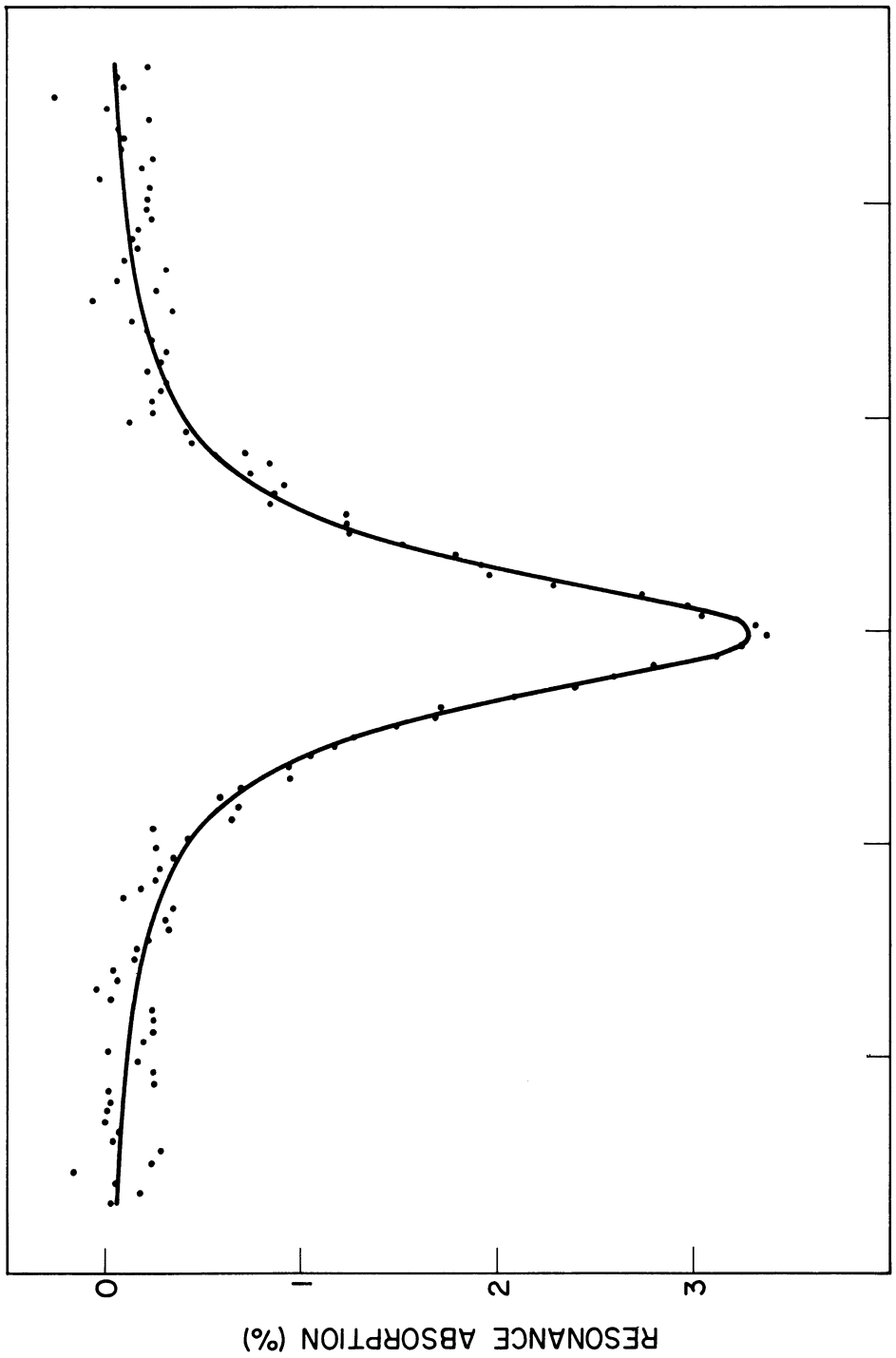

FIGURE V-4

RESONANCE ABSORPTION SPECTRUM FROM A PbTe SOURCE AND MnTe ABSORBER

TABLE V-2

PARAMETERS OBTAINED FROM SINGLE LORENTZIAN FITS TO MÖSSBAUER SPECTRA OF H_6TeO_6, MnTe, AND CrTe

Source	Absorber	Γ_{exp} (mm/sec)	δ (mm/sec)	Resonance Intensity	Area (mm/sec)	χ^2/N	Γ_{theor}* (mm/sec)
$PbTe^{125}$	H_6TeO_6	6.17±.15	-1.34±.04	.0377±.0004	.339	.948	6.0
$PbTe^{125}$	MnTe	7.66±.21	- .17±.05	.0331±.0004	.362	.795	5.9
$PbTe^{125}$	CrTe	9.59±.22	.05±.05	.0324±.0003	.376	.746	6.1

*Values of Γ_{theor} are obtained from Table III-1.

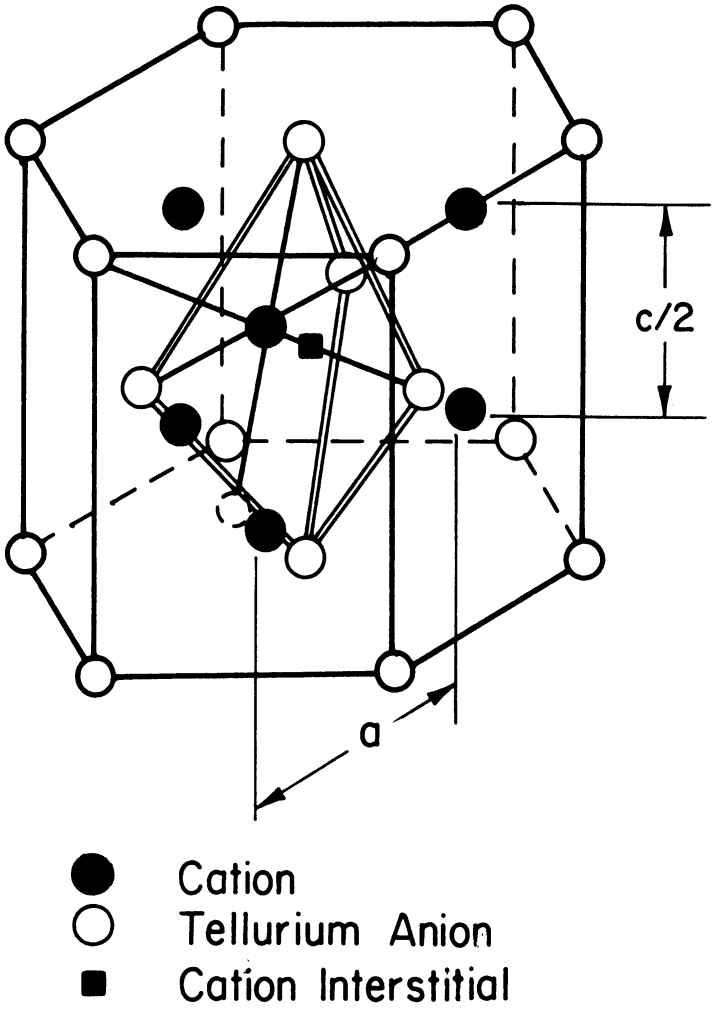

FIGURE V-5

CRYSTAL STRUCTURE OF MnTe AND CrTe (NiAs)

The cations form a simple hexagonal structure. Both the cations and anions have a six-fold coordination. The Mn sites are precisely octahedral only if the axial ratio c/a = 1.63. For MnTe the c/a ratio is c/a = 1.624.

The origin of the variations in hyperfine structure measurements with MnTe may arise from variations in composition of the material. As will be discussed in the next section for CrTe, it is difficult to characterize materials with NiAs structure due to the ease with which interstitial cations may be formed. The presence of interstitial cations can drastically alter physical, chemical, and magnetic properties. It is not at all unlikely that the Mössbauer hyperfine pattern would also be altered.

MnTe is antiferromagnetic with Néel temperature $T_N = 323^oK$. The saturated magnetic moment is $5.0\,\mu_B$, which is the expected value for a purely ionic Mn^{2+} $3d^5$ electronic configuration. The measured effective paramagnetic moment is $\mu_{eff} = 6.1\,\mu_B$. This agrees with the spin only value $5.92\,\mu_B$. It was on the basis of the magnetic structure that Shikazono[33] concluded that the crystal must be ionic. However, as will be discussed shortly, this does not appear to be the case.

The exchange coupling of the Mn spins again involves the superexchange process. The Mn-Mn bond distance (3.34Å) is much greater than the sum of atomic radii (2.80Å),[92] so direct exchange is not probable.[84] This is confirmed by the lack of metallic conductivity. The predominant cation-anion-cation superexchange interaction is between basal-plane layers.

The cation-anion-cation angle is $\sim 135^{o}$, and the magnetic interaction is assumed to have the sign of the 180^{o} superexchange interaction,[89] which is antiferromagnetic for the $3d^5$ electron configuration. The spin structure then consists of planes of ferromagnetically coupled Mn spins coupled antiferromagnetically.

MnTe has intrinsic semiconducting properties, high resistivity, and high thermoelectric power. This evidence seems to indicate that the bonding in MnTe is predominantly covalent. One model proposed for the MnTe bonding consists of resonating p^3 bonds.[90] This bonding mechanism does not involve the d-electrons, so the magnetic measurements still remain consistent. This bonding also fulfills the intrinsic semiconducting properties.

The superexchange mechanism in MnTe could presumably be the exchange polarization described by Slater[85] involving the Te 5s electrons. This superexchange mechanism does not involve a radial polarization of the 5s electrons, but rather an asymmetric angular polarization. The exchange interaction tends to "attract" the parallel 5s spin toward one Mn^{2+} and the antiparallel 5s spin toward the other Mn^{2+}. This polarization would affect the 5s electron charge density at the Te nucleus, but due to the equivalent exchange effects for parallel and antiparallel spin the 5s spin density should still remain paired at the Te nucleus. Then for antiferromagnetic coupling of the Mn^{2+} spins, no transferred hyperfine field is expected at the Te nucleus.

The tellurium sites in the NiAs structure are characterized as trigonal-prismatic. On the basis of covalent bonding, the structural symmetry would tend to indicate that the p orbitals are not equivalent. This would lead to an electric field gradient at the tellurium nucleus and quadrupole splitting in the Mössbauer spectrum.

The previous arguments support the claim that the measured hyperfine broadening has its origin in electric quadrupole splitting and not in magnetic hyperfine splitting. The variation in results observed in different measurements cannot yet be fully explained.

C. CrTe

Mössbauer measurements in CrTe were first reported by Shikazono.[33] A broadened single line was observed which was attributed to unresolved magnetic hyperfine splitting. Under the assumption that the width of the broadening was equal to the ground state magnetic splitting, the resultant internal field was estimated as H_{eff} = 50 kgauss. Due to the apparent disagreement between MnTe results, it was felt that the CrTe measurements were worth repeating.

1. Results

The Mössbauer spectrum was taken using a single line source of $PbTe^{125}$ and a CrTe absorber with a natural abundance of Te^{125}. The data are shown in Figure V-6. The data were fit

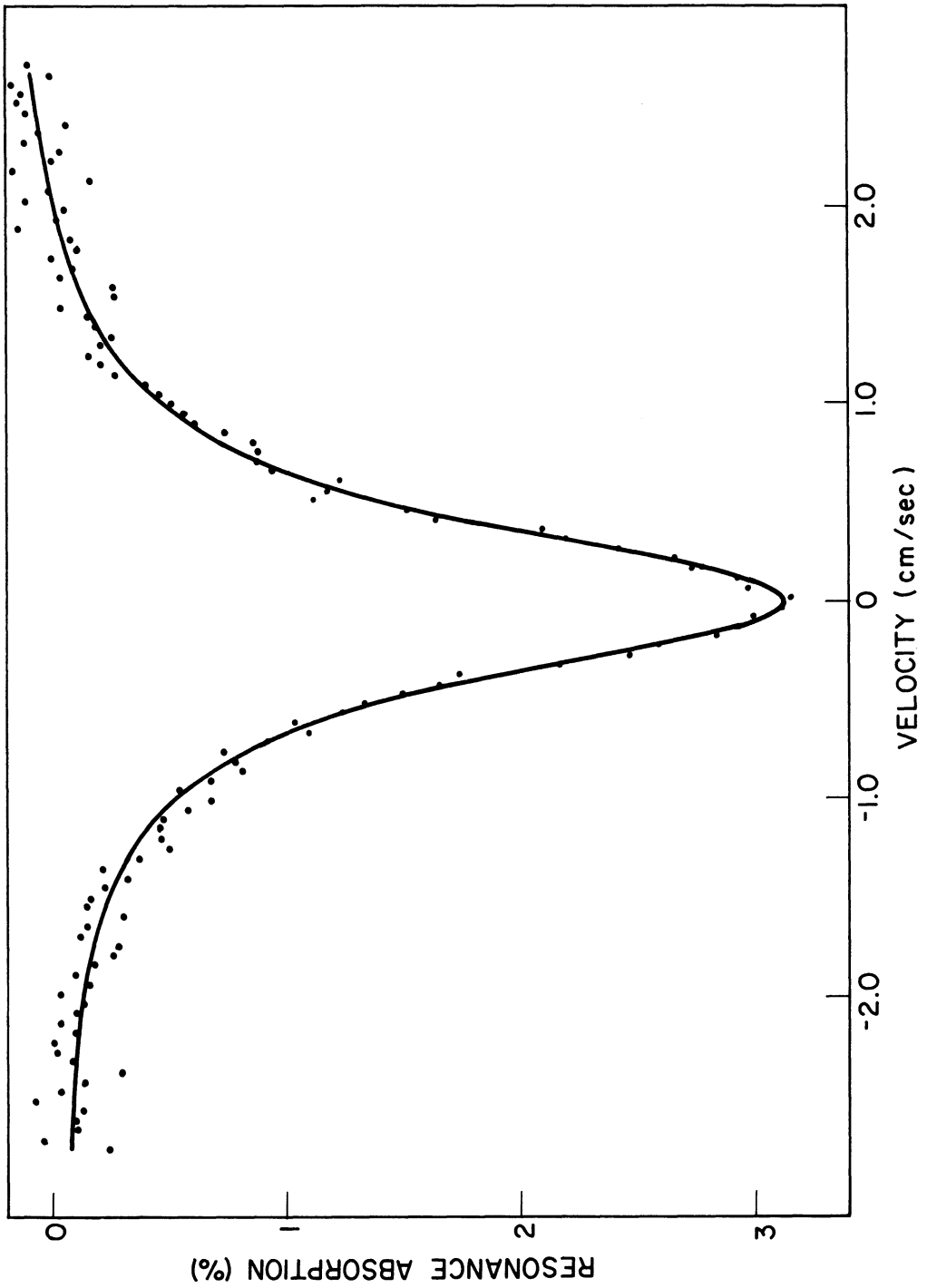

FIGURE V-6

RESONANCE ABSORPTION SPECTRUM FROM A PbTe SOURCE AND CrTe ABSORBER

with a single Lorentzian as shown in Figure V-6. The fitting parameters are listed in Table V-2.

It is readily apparent from a comparison of Γ_{exp} and Γ_{theor} that there is considerable broadening in the Mössbauer spectrum. A quadrupole splitting equivalent to the observed broadening $\Delta E_Q \simeq 3.5$ mm/sec should be partially resolved since $\Delta E_Q \sim .6$ Γ_{theor}. The fact that there is no resolved structure strongly suggests that the origin of the broadening is more likely magnetic hyperfine splitting. Assuming that the broadening is due solely to magnetic hyperfine splitting, the measured effective hyperfine field is H_{eff} = 58 kgauss.* The apparent agreement with Shikazono's result is somewhat fortuitous since the values were arrived at using different numbers and a different interpretation.

2. Discussion of the Data

CrTe, like MnTe, has the NiAs structure (Figure V-5). The composition of CrTe is even more difficult to characterize than MnTe due to the formation of interstitial ions. The tetrahedral interstices of the anion sublattice form a single trigonal-bipyramidal hole with a coordination of five. These holes easily accommodate cations as interstitials. An interstitial site is shown in Figure V-5. The presence of the interstitial sites makes it difficult to obtain stoichiometric CrTe and also allows the NiAs phase to extend over a considerable

*H_{eff} is calculated by assuming the broadening is equivalent to the spacing between peaks 2 and 5 in the hyperfine spectrum. (By observing the $CuCr_2Te_4$ spectrum in Figure V-1, it will be noted that the centers of the two unresolved peaks are approximately at the locations of peaks 2 and 5.) The measured value μ_e = +.74 nm (5.3) is used in the calculation.

range of composition.[93] Cation-rich compositions form interstitials and cation-poor compositions form vacancies.

The formation of interstitials in CrTe lowers the c/a ratio to c/a = 1.56. The smaller c/a ratio reduces the Cr-Cr bond distance to 3.10Å compared to the sum of atomic radii which is 2.80Å. The interstitial cations can interact through cation-cation exchange with the six neighboring octahedral cations. This introduces collective electrons as is evidenced by the metallic conductivity of CrTe.

CrTe is ferromagnetic with Curie temperature T_C = 350-360°K. The saturated magnetic moment is 2.45 μ_B, and the effective paramagnetic moment is μ_{eff} = 4.00 μ_B. Both of these values are lower than the expected values 4 μ_B and 4.90 μ_B, respectively, for a spin only Cr^{2+} $3d^4$ electronic configuration. The principal coupling of the Cr is again through the $\sim 135^\circ$ cation-anion-cation superexchange interaction. For $3d^4$ cations, the interaction is ferromagnetic.[89]

There are three possible explanations for the reduced moments: First, the presence of interstitials would reduce the saturated ferromagnetic moment since the cation-cation coupling is antiferromagnetic. The interstitial cations would then couple antiparallel to the principal cation lattice. Nevertheless, the paramagnetic moment should still approach the spin-only value 4.9 μ_B at high temperatures. Second, covalent bonding of the Cr 3d electrons with the Te would reduce the moment. Evidence from K absorption spectra in the

Cr indicates, however, that there is only a small participation of the d-electrons in the bonding.[94] Third, the competition between the antiferromagnetic cation-cation interactions and the ferromagnetic superexchange interaction may lead to spiral magnetic configurations and a reduced saturated moment.

The mechanism producing the hyperfine field is again the spin polarization of the Te 5s electrons by exchange coupling with the Cr 3d electrons. For ferromagnetic coupling of the Cr^{2+} spins (as opposed to the antiferromagnetic coupling of Mn^{2+}), the tellurium 5s electrons can be spin polarized. Since the exchange interactions with the parallel and antiparallel 5s spins are not equivalent, a radial polarization can occur resulting in unpaired 5s spin density (antiparallel to the Cr^{2+} spin) at the Te nucleus. This would yield a positive contact hyperfine field.

The bonding in CrTe may also be described by the resonating p^3 bonds.[44] As in MnTe, an unbalancing of the p-electrons may give rise to a field gradient at the Te site and subsequent quadrupole splitting. On this basis, the quadrupole interaction cannot be excluded as a source of the hyperfine broadening in CrTe.

Hyperfine measurements at anion sites in other ferromagnetic NiAs structures indicate the presence of both magnetic and electric quadrupole hyperfine effects. NMR measurements of the As^{75} resonance in MnAs[95] and the Sb^{123} resonance in MnSb[96] indicate internal hyperfine fields H_{eff} of 283.2 kgauss and 352.6 kgauss, respectively, and quadrupole coupling constants

e^2qQ of 16.1 Mc/sec and 93 Mc/sec, respectively. These quadrupole coupling constants correspond to splittings ΔE_Q = .28 mm/sec and ΔE_Q = 1.63 mm/sec. The measured broadening in CrTe was definitely larger than these values, but quadrupole splitting cannot be ignored as a possible contributor to the broadening.

D. H_6TeO_6

1. Results

Mössbauer measurements were taken using a single line source of $PbTe^{125}$ and an orthotelluric acid (H_6TeO_6) absorber with a natural abundance of Te^{125}. The experimentally measured spectrum, shown in Figure V-7, consisted of a very narrow single line. The parameters obtained from the fit with a single Lorentzian are listed in Table V-2. The fitting curve is also shown in Figure V-7. These are the first reported Mössbauer measurements for this compound.

The experimentally measured line width Γ_{exp} = 6.17 mm/sec is in excellent agreement with the theoretical line width Γ_{theor} = 6.0 mm/sec corrected for absorber thickness. This would indicate that there is no additional broadening caused by unresolved quadrupole splitting. This would confirm the existence of only the cubic crystalline modification of orthotelluric acid. The octahedrally coordinated tellurium sites in this structure would not be expected to have a quadrupole splitting. On the other hand, a monoclinic structure would

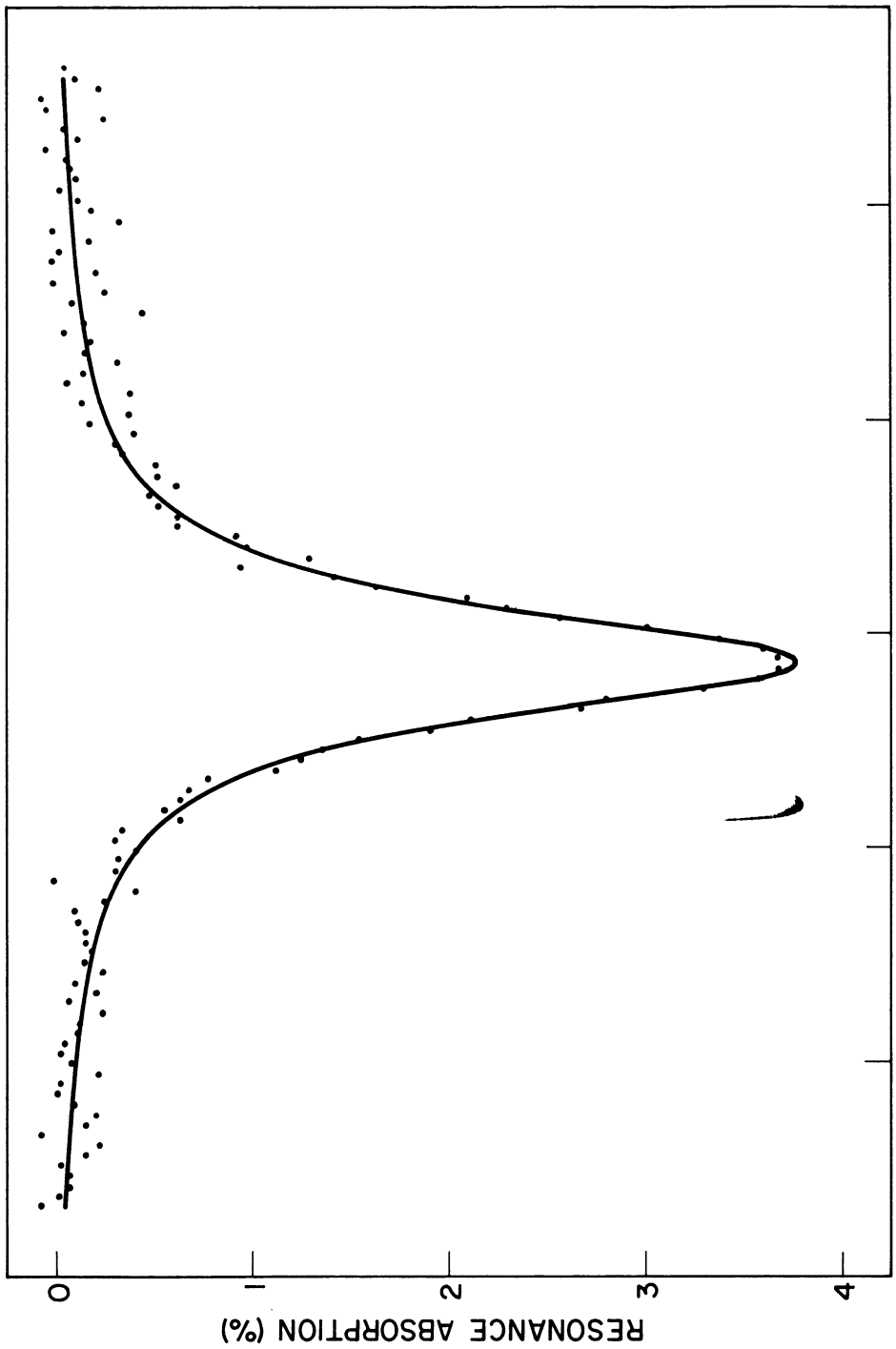

FIGURE V-7

RESONANCE ABSORPTION SPECTRUM FROM A PbTe SOURCE AND H_6TeO_6 ABSORBER

presumably contribute an electric field gradient at the tellurium sites and subsequent quadrupole splitting.

2. Discussion of the Data

The large negative isomer shift for H_6TeO_6 indicates a change in the 5s electron density compared to PbTe. Due to the strong electronegativity of the OH^- ligand, the compound presumably has considerable ionic character. In the limit of a complete ionic character, tellurium would be present as Te^{6+} with a bare 5s and 5p electron shell. Since an ion with this large a positive charge is highly unlikely, there is undoubtedly some covalent character. As an extreme limit, the bonding could be described as completely covalent. For octahedrally coordinated tellurium, the bonding can be represented by sp^3d^2 hybridization.[77] Since one electron occupies each orbital and the s character of each orbital is 1/6, there is the equivalent of one 5s electron at the tellurium site.

On the basis of this simple treatment, the 5s density could vary from the equivalent of one 5s electron to zero 5s electrons, depending on the percent ionic character. The effect of this change will be treated in more detail in the following section.

E. Isomer Shifts in Tellurium Compounds

The details of the isomer shift interaction were described earlier in Chapter II. Since nearly all of the preceding measurements were made using either a PbTe source or absorber, it is convenient to give the isomer shifts with respect to

this standard compound. In Table V-3, the measured values of the isomer shift are listed in order of increasing velocity. All of the values except that for the Te metal were obtained using the PbTe as a source.*

TABLE V-3

ISOMER SHIFT FOR VARIOUS TELLURIUM COMPOUNDS WITH RESPECT TO A PbTe SOURCE

Absorber	Isomer Shift (mm/sec)
H_6TeO_6	-1.34 ± .04
MnTe	- .17 ± .05
$CuCr_2Te_4$	- .03 ± .03
PbTe	+ .03 ± .03
CrTe	+ .05 ± .05
Te	+ .41 ± .09
TeO_2	+ .62 ± .16

If the change in s-electron density at the nucleus is known for the compounds, the measured isomer shifts can be used to determine $\delta R/R$ from Equation (II.17). Such an interpretation is simplified if we first make the assumption that only the outer 5s valence electron shell produces a change in the s-electron density at the nucleus. To make an accurate prediction of the change in s-electron density requires precise knowledge of the molecular wave functions. However, in some cases, it is possible to estimate the sign and perhaps the magnitude of the change in s-electron density without complete knowledge of the electron wave functions.** From this it is then possible to determine the sign and magnitude of $\delta R/R$.

*The sign of the isomer shift is reversed when the PbTe is used as the absorber rather than the source.

**These simplified interpretations can sometimes lead to erroneous results, though, as exemplified by the Sn^{119} controversy.

The isomer shift measurements for Te metal and H_6TeO_6 can easily be interpreted on the basis of a rather simplified description of the electronic structure for the compounds. Violet, et al.,[30] have estimated the 5s electron density for Te metal from their molecular orbital bonding scheme. The 5s electron density is calculated to be the equivalent of 1.6 5s electrons. In the models proposed earlier for H_6TeO_6, the density is the equivalent of 1 5s electron in the covalent bonding limit and 0 5s electrons in the ionic bonding limit. In using either bonding scheme for H_6TeO_6, the 5s electron density in Te is definitely <u>greater</u> than that for H_6TeO_6.

As described in Chapter II, the isomer shift for H_6TeO_6 and Te can be written as

$$\delta_{H_6TeO_6} = \frac{4\pi}{5} Z e^2 R^2 S'(Z) \left[|\psi_s(0)|^2_{H_6TeO_6} - |\psi_s(0)|^2_{PbTe} \right] \left(\frac{\delta R}{R} \right) \qquad (V.5)$$

$$\delta_{Te} = \frac{4\pi}{5} Z e^2 R^2 S'(Z) \left[|\psi_s(0)|^2_{Te} - |\psi_s(0)|^2_{PbTe} \right] \left(\frac{\delta R}{R} \right) . \qquad (V.6)$$

Combining Equations (V.5) and (V.6) to eliminate the s-electron density for PbTe yields

$$\delta_{Te} - \delta_{H_6TeO_6} = \frac{4\pi}{5} Z e^2 R^2 S'(Z) \left[|\psi_s(0)|^2_{Te} - |\psi_s(0)|^2_{H_6TeO_6} \right] \left(\frac{\delta R}{R} \right) . \qquad (V.7)$$

From the measured isomer shifts $\delta_{Te} - \delta_{H_6TeO_6} = +1.75$ mm/sec. Since the 5s electron density at the nucleus is greater for Te than for H_6TeO_6, the sign of the term in brackets is positive.

Since both the isomer shift and s-electron density terms are positive, $\delta R/R$ must be positive. This implies that the nuclear excited state radius must be greater than that for the ground state. This confirms the identical conclusions reached by other authors.[31,51]

If it is assumed that H_6TeO_6 has completely ionic character, the difference in s-electron density in Equation (V.7) is the equivalent of 1.6 5s electrons. Equation (V.7) can then be evaluated numerically using S'(52) = 2.44 and nuclear radius $R \simeq 1.5\ A^{1/3} \times 10^{-13}$ cm. The 5s electron density in tellurium can be estimated from the results of Shirley.[51] The value is approximately $\psi^2_{5s}(0) = .18 \times 10^{26}\ cm^{-3}$. Evaluating Equation (V.7) numerically yields a value of $\delta R/R = +2.8 \times 10^{-4}$. In the limit of completely covalent character, the value would be reduced to $\delta R/R = +1.1 \times 10^{-4}$. This range of values is in reasonable agreement with the values estimated by Shirley for Te^{125}.

APPENDIX A

SUMMARY OF RADIATION EFFECTS MEASUREMENTS USING THE MÖSSBAUER EFFECT

TABLE A-1

SUMMARY OF RADIATION EFFECTS MEASUREMENTS
USING THE MÖSSBAUER EFFECT

Preparation of Mössbauer Level	Mössbauer Nucleus	Chemical Form		Radiation Effects	Reference
		Source	Absorber		
Alpha Decay $Am^{241} \rightarrow Np^{237} + \alpha$	Np^{237}	NpO_2	NpO_2	Mössbauer fraction f following α-decay approximately ¼ f following β-decay.	1
Nuclear Reaction $K^{39}(d,p)K^{40}$ 3.5 Mev deuterons	K^{40}	K metal	KCl	Observed f=1.19% compared to expected f=.03%. Suspect oxidation in the source.	6
Nuclear Reaction $Fe^{56}(d,p)Fe^{57}$ 2.8 Mev deuterons	Fe^{57}	Fe metal	Fe metal	No reduction in f value. Less than 10% change in hyperfine interaction.	7
Nuclear Reaction $Fe^{56}(d,p)Fe^{57}$ 4.8 Mev deuterons	Fe^{57}	Stainless steel	Stainless steel	No reduction in f value.	8
Coulomb Excitation	Ni^{61}	Ni metal	Ni metal	f value only 75% of that observed for β-decay parent. Absorption areas identical. No change in f as a function of irradiation time.	2
Coulomb Excitation	Fe^{57}	Fe metal	$Na_4Fe(CN)_6 \cdot 10H_2O$	Essentially no change in f value.	14,3
		Fe_2O_3	Fe_2O_3	f value reduced by a factor of 2. No change in hyperfine splitting.	

Coulomb Excitation	Ge^{73}	Thick Ge metal	Ge metal	Source f value at 78°K=.8%. Ge showed conversion from crystalline to amorphous state after irradiation.	4,5
		Thin Ge metal on Cr	Ge metal	Source f value at 78°K=5.8%. Absorber f value at 78°K=6.0%.	
		Thin Ge metal on Cr	GeO_2	Thin targets used to implant Coulomb excited Ge atoms in Cr metal.	
Neutron Capture in Thermal Neutron Beam	K^{40}	KF KCl K	KCl	Observed f values are smaller than computed in all cases.	9
Neutron Capture in Thermal Neutron Beam	Gd^{156}	Gd_2O_3	Gd metal	"Mirror experiment" in Gd^{158} shows the following effect: f oxide target x f metal absorber = .6 x f metal target x f oxide absorber. Line for Gd_2O_3 target approx. 10% greater than for Gd metal target.	13
	Gd^{158}	Gd metal Gd_2O_3	Gd_2O_3 Gd metal		
Neutron Capture in Thermal Neutron Beam	Fe^{57}	Fe metal	Stainless steel	Splitting of outer lines in hyperfine spectrum greater than if used as absorber with Co^{57} source.	16
		Fe_2O_3	Stainless steel	Splitting of outer lines in hyperfine spectrum less than absorber value. Reduction in f value still uncertain.	

Isomer Production by Neutron Capture	Sn^{119}	SnO_2	SnO_2	No evidence of radiation effects.	
		Mg_2SnO_4	SnO_2	Satellite peak which anneals out at 600-1000°C. Postulate peak due to Sn^{2+} produced by (n,γ) recoil. Approx. 25% of Sn atoms in defect environment.	15
Isomer Production by Neutron Capture	Te^{125}	PbTe	PbTe	Isomer shift of 2 mm/sec after irradiation. Decayed to 0 with exponential lifetime τ = 10 days.	17
Isomer Production by Neutron Capture	Te^{125}	PbTe Te metal TeO_2	PbTe	No evidence of radiation effects.	Present Work

APPENDIX B

CIRCUIT DIAGRAMS OF MAGNET FIELD SUPPLY AND DRIVE AMPLIFIER

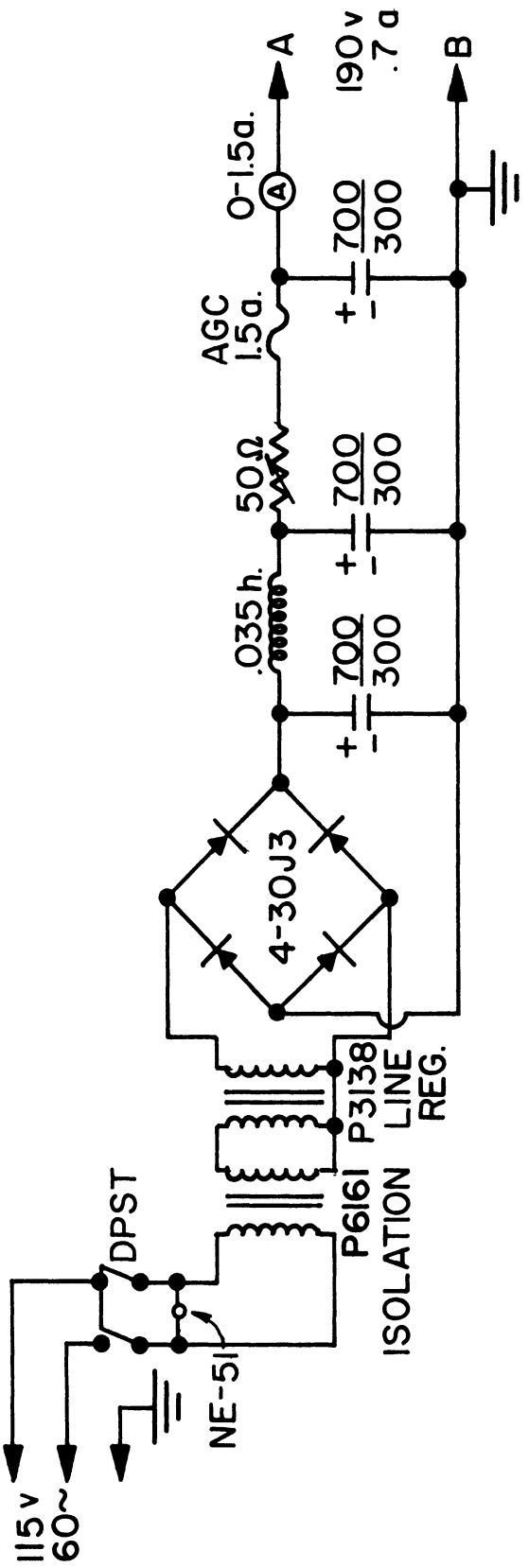

FIGURE B-1

CIRCUIT DIAGRAM OF MAGNET FIELD SUPPLY

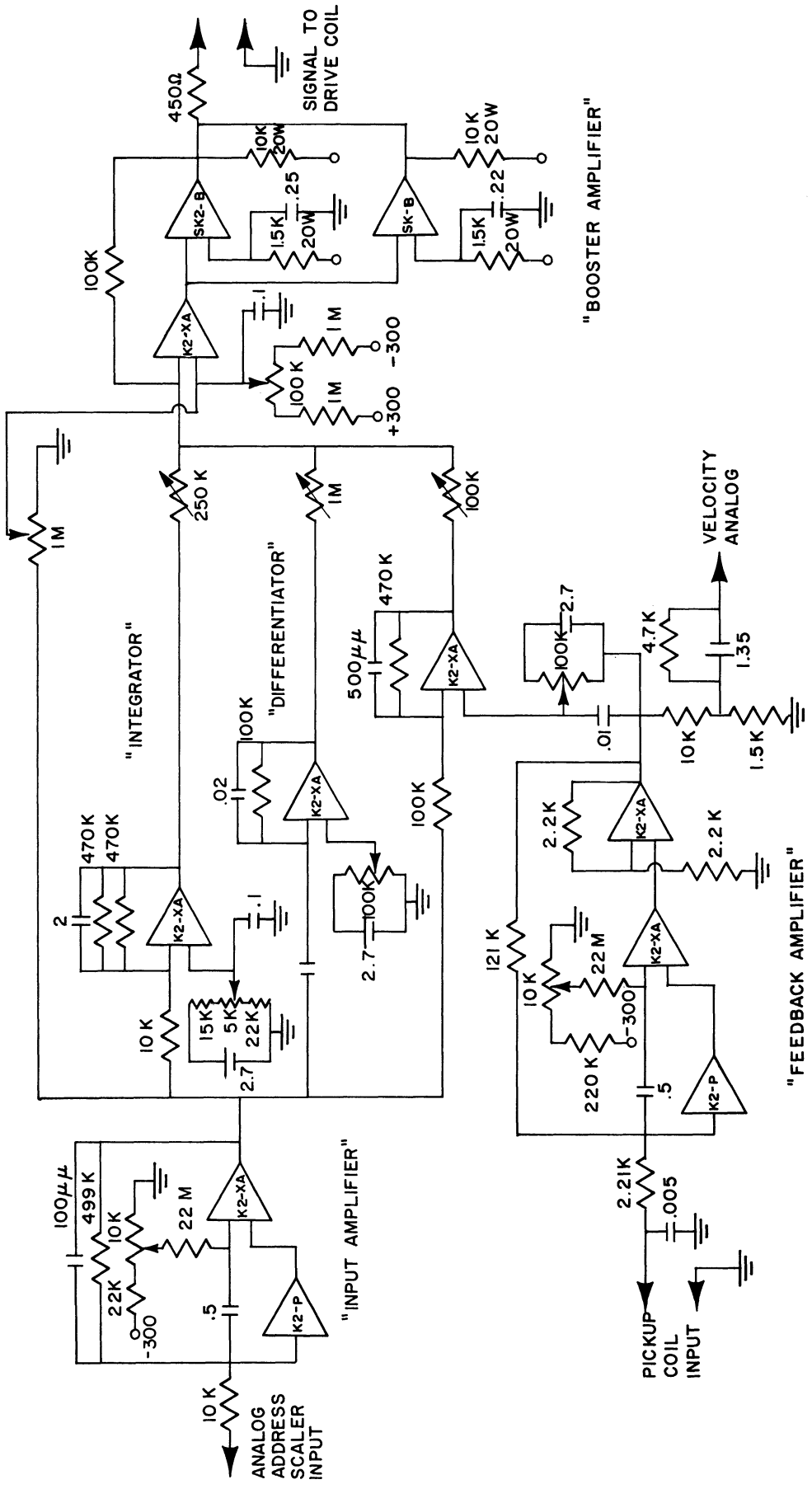

FIGURE B-2

CIRCUIT DIAGRAM OF DRIVE AMPLIFIER

APPENDIX C

DESCRIPTION OF DATA ANALYSIS PROGRAMS

The following is a description of the data analysis programs used for least squares fitting of Mössbauer effect data. In writing such a program to analyze data, it would be desirable to have a "universal program" which could be used to analyze all of the types of Mössbauer data that can be acquired. Experience has indicated that new situations arise so frequently that such a program is never up-to-date. For greater efficiency, a "main program" has been written which performs the basic data operations for all types of Mössbauer spectra. The details of the particular spectrum being analyzed are included in a "theory" subroutine. This subroutine can easily be modified to analyze any type of Mössbauer spectrum.* The programs are all written in the MAD (Michigan Algorithmic Decoder) language for use on the IBM 7090 computer.**

A. Least Squares Curve Fitting

The problem to be solved in a curve fitting routine is the following: For each channel in the analyzer, i, an experimentally measured number of counts, Y_i, are stored. One wishes to construct a curve of a known shape (Lorentzian shape for the resonance lines of Mössbauer spectra) so that it most closely approximates the data.

*This technique was suggested by W. Henning, Technische Hochschule, München.

**The translation from the MAD to FORTRAN language can be made rather easily.

In using the least squares procedure, we assume the measured values Y_i have a Gaussian distribution about the true value F_i with a standard deviation σ_i. The probability that for an experimentally determined Y_i the true value lies between F_i and $F_i + dF_i$ is

$$P(F_i)dF_i = \frac{1}{\sqrt{2\pi\sigma_i^2}} e^{-\frac{(F_i - Y_i)^2}{2\sigma_i^2}} \quad . \tag{C.1}$$

The best (most probable) guess of the fitting function F occurs when the product of the probabilities is a maximum.

$$P = \prod_i P(F_i) = \prod_i \frac{1}{\sqrt{2\pi\sigma_i^2}} e^{-\frac{(F_i - Y_i)^2}{2\sigma_i^2}} \tag{C.2}$$

$$= e^{-\sum_i \frac{(F_i - Y_i)^2}{2\sigma_i^2}} \prod_i \frac{1}{\sqrt{2\pi\sigma_i^2}} \quad . \tag{C.3}$$

Equation (C.3) is a maximum when $q \equiv \sum_i \frac{(F_i - Y_i)^2}{2\sigma_i^2}$ is a minimum. A reasonable estimate for the standard deviation σ_i is σ_i, the experimental standard deviation of Y_i.

Two general approaches can be used for minimizing q. The first is a brute force "variation of parameters." The independent variable parameters in F are incremented in preset steps and the function q is calculated for each set of parameters. The combination resulting in the smallest value of q is taken as the "best" set of fitting parameters. Due to the fact that the parameters are varied in finite increments, there is no assurance that the true minimum is reached nor that

there is not another set of parameters giving an equally good minimum. This particular technique was in use for some time for Mössbauer effect data analysis.* The main disadvantage was that it proved to be very time consuming when high accuracy in the parameters was desired. This method may be necessary, however, in analyzing complex spectra where other methods may fail.

The second approach used in minimizing q is the use of Gauss' method. The function F_i depends on i and the independent variable parameters $P_1 \cdots P_M$, or $F_i = F(i, P_1 \cdots P_M)$. To minimize q, the partial derivatives of q with respect to the variable parameters are taken and set equal to zero, or

$$\frac{\partial q}{\partial P_j} = \sum_i \frac{(F_i - Y_i)}{\sigma_i^2} \left.\frac{\partial F}{\partial P_j}\right)_i = 0 \quad . \tag{C.4}$$

This forms a set of M simultaneous equations. Suppose an initial estimate is made of the parameters $(P_{1_0} \cdots P_{M_0})$ and the function F_i is expanded in a truncated Taylor series about this point in parameter space, so

$$F_i \simeq F_{i_0} + \sum_k \left.\frac{\partial F}{\partial P_k}\right)_{i,0} \Delta P_k \tag{C.5}$$

and

$$\frac{\partial q}{\partial P_j} = \sum_i \frac{\left(F_{i_0} - Y_i + \sum_k \left.\frac{\partial F}{\partial P_k}\right)_{i,0} \Delta P_k\right)}{\sigma_i^2} \left.\frac{\partial F}{\partial P_j}\right)_{i,0} \quad . \tag{C.6}$$

*The program was similar to one used by M. B. Stearns, Scientific Laboratory, Ford Motor Company, Dearborn, Michigan.

Equation (C.6) can be rewritten as

$$\sum_k \Delta P_k \sum_i \frac{1}{\sigma_i^2} \frac{\partial F}{\partial P_k}\Big)_{i,0} \frac{\partial F}{\partial P_j}\Big)_{i,0} = \sum_i \frac{(F_{i_0} - Y_i)}{\sigma_i^2} \frac{\partial F}{\partial P_j}\Big)_{i,0} \quad . \tag{C.7}$$

This forms a set of M simultaneous equations of the form

$$\underline{D}\,\underline{\underline{A}} = \underline{B} \quad . \tag{C.8}$$

This set of equations is known as the normal equations, where

$$D_k = \Delta P_k \quad , \tag{C.9}$$

$$A_{kj} = \sum_i \frac{1}{\sigma_i^2} \frac{\partial F}{\partial P_k}\Big)_{i,0} \frac{\partial F}{\partial P_j}\Big)_{i,0} \quad , \tag{C.10}$$

$$B_j = \sum_i \frac{1}{\sigma_i^2} (F_{i_0} - Y_i) \frac{\partial F}{\partial P_j}\Big)_{i,0} \quad . \tag{C.11}$$

Since A_{kj} and B_j are obtained from the initial estimates of the parameters, the normal equations can be solved for D_k, or

$$\underline{D} = \underline{B}\,\underline{\underline{A}}^{-1} \quad . \tag{C.12}$$

The solutions D_k are then used as corrections to the initial estimates of the parameters, giving a new set of parameters

$$P_{k_1} = P_{k_0} + \Delta P_k \quad . \tag{C.13}$$

Using the corrected parameters of Equation (C.13), the entire procedure can be repeated to obtain the next increment ΔP_k.

After each iteration, the value of χ^2/N is computed where

$$\chi^2_N = \sum_i \frac{(F_i - Y_i)^2}{\sigma_i^2 (IM - M)} \quad . \qquad \text{(C.14)}$$

In this expression IM is the number of data points and M is the number of fitting parameters. Equation (C.14) is related quite simply to the earlier expression referred to as q. The function χ^2/N is a measure of the deviation of the measured spectrum and the fitted spectrum--the smaller the value, the better the agreement. The iteration procedure described earlier is continued until χ^2/N reaches a minimum value.

This method of solution has the added advantage that the statistical error in the parameters is immediately available. It can be shown[103] that

$$\sigma_k = \left(A_{kk}^{-1} \cdot \chi^2_N \right)^{1/2} \quad , \qquad \text{(C.15)}$$

where A_{kk}^{-1} is the k^{th} diagonal element of the inverse matrix of A_{kj}.

Gauss' method has proved very satisfactory in analyzing most Mössbauer data. Fully and partially resolved spectra were handled with no difficulty. Unresolved spectra could not be properly fit, however. In addition, the initial parameter

estimates need not be extremely precise to achieve rapid convergence. Most parameter estimates were made by just a quick visual check of the spectrum.

B. Data Analysis Program

1. Main Program

As mentioned earlier, the basic mechanics of the least squares fitting and routine data corrections are performed by a "main program." The following is a general outline of the operations the "main program" will perform: Several sets of input data can be added together with the appropriate number of overflow counts for each set. The data is then printed out along with the various input parameters. The input parameters are checked to see if: a) the number of fitting parameters M is less than 25; b) the number of data points IM is less than 512; and c) there are more data points than fitting parameters. The solution is terminated if any of these checks fail.

The infinite velocity background count rate and slope are determined approximately from the average count rates at large negative and positive velocities. The end points of the spectrum are determined so that 5 percent of the channels at each end of the spectrum are eliminated from the analysis. This is done because of the large error signal in this region of the spectrum.

The first and last data points are used to check the "theory" subroutine. The partial derivatives in the "theory"

subroutine are all evaluated using the first and last data points and the initial parameter estimates. These results are then printed out. This provides a very convenient check for errors in the subroutine if later analysis proves unsuccessful.

The program initially uses Gauss' method to provide an iterative solution for the "best" fit to the data. The solution is obtained as described in the first part of this appendix. The normal equations are evaluated for the fitting function described in the "theory" subroutine. The function is evaluated using the initial estimates of the parameters which are included as input to the program. The normal equations are then solved to give the increments in each parameter. The fitting parameters and χ^2/N value are printed out after each iteration. The iteration is continued at least three times and is terminated either when the number of iterations exceeds twenty or when the value of χ^2/N reaches a minimum.

In the event the normal equations are unsolvable or the error in the fitting is greater than a preset value, the method of steepest descent is used rather than Gauss' method to provide the interative solution for the "best" fit. In practice, this method was rarely needed so the details will not be discussed.

After the iteration is terminated, the data are normalized so the results are expressed as percent resonance intensity. In addition, the standard deviation of the data points and the

difference between the measured spectrum and the fitted spectrum are calculated. The area under the spectrum is obtained by numerical integration.

The error in the fitting parameters is calculated using the method described in the first part of the appendix (see Equation (C.15)). The distribution in standard deviation units of the error between the measured and fitted spectrum is also calculated.

The final results which are printed out include the "best" fitting parameters and their statistical fitting error, the area under the spectrum, and the error distribution for the fitting curve. The data printed out include the normalized measured spectrum, the fitted spectrum, the difference in spectra, and the standard deviation of the data.

The data are also plotted using an internal subroutine. The measured spectrum and the fitted spectrum are plotted on the same graph. The difference between the spectra is plotted on a separate graph. This provides a very quick visual check of the success in fitting the data.

The complete "main program" is included in section C of this appendix.

2. Theory Subroutine

The "theory" subroutine includes all of the details of the function which is to be fitted to the data. A typical subroutine is included in section C of this appendix. The

function which is fitted to the data consists of a superposition of Lorentzian line shapes and has the form

$$FT(I) = U_\infty \left\{ 1 - \sum_J \frac{I(J)\,\Gamma_{1/2}(J)}{(I - X(J))^2 + \Gamma_{1/2}(J)^2} - SL \cdot I \right\} , \qquad (C.16)$$

where

U_∞ = infinity counting rate

$I(J)$ = intensity of the J^{th} line

$X(J)$ = position of the J^{th} line

$\Gamma_{1/2}(J)$ = half width at half maximum of the J^{th} line

SL = normalized linear slope of the background counting rate.

The parameters $\Gamma_{1/2}(J)$ and $X(J)$ are expressed in channel units so I can be used in channel units. The line location $X(J)$ can be expressed as a function of the isomer shift, quadrupole splitting parameter, and magnetic hyperfine interaction parameters. All of these are expressed with respect to the zero velocity channel.

In addition to the function itself, the subroutine must include the partial derivatives DFT of the function FT with respect to each of the variable parameters.

For the example include in section C of this appendix, several simplifying assumptions have been made. The subroutine describes a six-line spectrum with equal line widths for each line. The intensities of the lines are constrained to the ratio 3:2:1. The variable parameters include $\Gamma/2$, $\mu_g H_{eff}$, δ, U_∞, C, $R = g_e/g_g$, and SL. $\Gamma/2$, the half width at half

maximum of the resonance line; $\mu_g H_{eff}$, the magnetic hyperfine interaction constant; and δ, the isomer shift, are expressed in channel units. C is the fractional multiplying factor for the line intensities, so the resultant line intensity ratio is 3C:2C:1C.

This subroutine can easily be changed to provide any possible variations in the fitting function.

C. Listing of Computer Programs

1. Main Program

```
      DIMENSION Y(512),SETUP(24),YS(512),P(25),X(512),DF1(25),DF2(2
     1 5),DY(512),BV(25),AM(625,AVV),PM(625,AVV),Z(25),LR(25),DP(25)
     2 ,FIT(512),YNRM(512),DYNRM(512),DIFF(512),SIG(25),INVDI(25),XX
     3 (512),ZP(512),IMAGE(10000),DF(25)
      VECTOR VALUES AVV=2,1,0
      INTEGER SETUP,IM,M,NDECKS,I,ID,ILC,IUC,K,ILP,IUP,J,L,SP,MDIF,
     1 P3S,P2S,P1S,P0S,N0S,N1S,N2S,N3S

       READ AND PRINT INPUT DATA

START EXECUTE ZERO.(Y(0)...Y(511),YS(0)...YS(511))
      EXECUTE SPRAY.($$,SETUP(1)...SETUP(24))
      READ FORMAT INPUT,SETUP(1)...SETUP(24),IM,M,VCAL,NDECKS,INCR
      VECTOR VALUES INPUT=$12C6/12C6/2I3,F8.5,I3,F8.0*$
      PRINT FORMAT INITAL,SETUP(1)...SETUP(24)
      VECTOR VALUES INITAL=$1H1,S10,12C6/S11,12C6*$
      PRINT COMMENT $0
     1   INPUT DATA$
      PRINT FORMAT INPR,IM,M,VCAL,NDECKS,INCR
      VECTOR VALUES INPR=$S20,4HIM= ,I3,S4,3HM= ,I3,S4,6HVCAL= ,F8.
     1 5,10H MM/SEC/CH,S4,8HNDECKS= ,I3,S4,6HINCR= ,F8.0*$
      THROUGH F1,FOR ID=1,1,ID.G.NDECKS
      READ FORMAT ADDIN,ADDC
      VECTOR VALUES ADDIN=$F8.0*$
      PRINT FORMAT ADDPR,ADDC
      VECTOR VALUES ADDPR=$//S20,20HADDITIVE CONSTANT = ,F8.0*$
      READ FORMAT IPUT,Y(0)...Y(IM)
      VECTOR VALUES IPUT=$(8F8.0)*$
      PRINT FORMAT DAT,Y(0)...Y(IM)
      VECTOR VALUES DAT=$//(S19,8F8.0)*$
      THROUGH F1,FOR I=0,1,I.G.IM
F1    YS(I)=YS(I)+Y(I)+ADDC
      PRINT COMMENT $0                                          SUMMA
     1 TION OF INPUT DATA$
      PRINT FORMAT YSUM,YS(0)...YS(IM)
      VECTOR VALUES YSUM=$//(S19,8F8.0)*$
      READ FORMAT PARIN,P(1)...P(M)
      VECTOR VALUES PARIN=$(8F8.0)*$
      PRINT FORMAT INITAL,SETUP(1)...SETUP(24)

       CHECK FOR PROPER CONDITIONS FOR ANALYSIS

      WHENEVER M.LE.0
      OR WHENEVER M-25.GE.0
      PRINT FORMAT MVAL,M
```

```
      VECTOR VALUES MVAL=$1HO,S20,48HONLY 1 TO 25 FITTING PARAMETER
     1 S ARE ALLOWED, NOT,I3*$
      TRANSFER TO START
      OTHERWISE
      CONTINUE
      END OF CONDITIONAL
      WHENEVER IM.GE.512
      PRINT FORMAT IMVAL,IM
      VECTOR VALUES IMVAL=$1HO,S20,42HONLY 1 TO 512 DATA POINTS ARE
     1  ALLOWED, NOT,I3*$
      TRANSFER TO START
      OTHERWISE
      CONTINUE
      END OF CONDITIONAL
      MDIF=IM-M
      WHENEVER MDIF.LE.0
      PRINT FORMAT DIFVAL,IM,M
      VECTOR VALUES DIFVAL=$1HO,S20,17HMORE PARAMETERS (,I3,20H) TH
     1 AN DATA POINTS (,I3,1H)*$
      TRANSFER TO START
      OTHERWISE
      CONTINUE
      END OF CONDITIONAL

C     APPROXIMATE SLOPE AND BACKGROUND

      ILC=1
      IUC=IM-1
      YMAX=0.
      THROUGH F2,FOR I=ILC,1,I.G.IUC
F2    WHENEVER YS(I).G.YMAX,YMAX=YS(I)
      BK=.7*YMAX
      SLP=0.
      THROUGH F5,FOR K=1,1,K.G.2
      XBKL=0.
      XBKU=0.
      BKL=0.
      BKU=0.
      THROUGH F3,FOR I=ILC,1,I.G.IUC/2
      WHENEVER YS(I).L.BK+SLP*I
      TRANSFER TO F3
      OTHERWISE
      XBKL=XBKL+1.
      BKL=BKL+YS(I)
F3    END OF CONDITIONAL
      THROUGH F4,FOR I=IUC,-1,I.L.IUC/2+1
      WHENEVER YS(I).L.BK+SLP*I
      TRANSFER TO F4
      OTHERWISE
      XBKU=XBKU+1
      BKU=BKU+YS(I)
F4    END OF CONDITIONAL
      BKL=BKL/XBKL
      BKU=BKU/XBKU
```

```
            SLP=2.*(BKU-BKL)/(IUC-ILC)
F5          BK=(BKL+BKU)/2.-SLP*(IUC-ILC)/2.
            BKND=BK
            SLOPE=SLP/BK*(IM+1)*100
            PRINT FORMAT APPSB,BKND,SLOPE
            VECTOR VALUES APPSB=$1HO,S19,25HAPPROXIMATE BACKGROUND = F14.
           1 4//S20,20HAPPROXIMATE SLOPE = F14.4,8H PERCENT*$

            END POINTS OF SPECTRUM

            ILP=ILC+.05*IM
            IUP=IUC-.05*IM
            PRINT FORMAT ENPT,ILP,IUP
            VECTOR VALUES ENPT=$1HO,S19,18HLOWER END POINT = I5//S20,18HU
           1 PPER END POINT = I5*$

            CHECK OF FIRST AND LAST DATA POINTS WITH THEORY

            THROUGH F6,FOR I=0,1,I.G.511
            DY(I)=SQRT.(YS(I))
F6          X(I)=I
            J=0
            I=ILP
            EXECUTE THEORY.(J,X(I),P,A1,B1,F1,DF1)
            I=IUP
            EXECUTE THEORY.(J,X(I),P,A2,B2,F2,DF2)
            PRINT FORMAT CK,ILP,IUP,X(ILP),X(IUP),YS(ILP),YS(IUP),DY(ILP)
           1 ,DY(IUP),F1,F2
            VECTOR VALUES CK=$////S10,20HCHECK OF DATA POINTS,I5,S2,3HAND
           1 ,I5,S2,11HWITH THEORY//S20,2HX ,2E18.4/S20,2HY ,2E18.4/S20,2H
           2 DY,2E18.4//S20,2HF ,2E18.4/*$
            THROUGH F7,FOR K=1,1,K.G.M
F7          PRINT FORMAT PARCK,K,DF1(K),DF2(K)
            VECTOR VALUES PARCK=$/S20,5HDF/DP,I3,E12.4,E18.4*$

            SETTING UP NORMAL EQUATIONS

            PRINT FORMAT INITAL,SETUP(1)...SETUP(24)
            PRINT COMMENT $0                                              I
           1 NTERMEDIATE RESULTS$
            PRINT COMMENT $0         ITERATION         CHISQ/N            PA
           1 RAMETERS$
            AVV(2)=M
            CHISQ=1.
F8          WVAR=0.
            EXECUTE ZERO.(BV(1)...BV(25),AM(1)...AM(625))
            THROUGH F9,FOR I=ILP,1,I.G.IUP
            EXECUTE THEORY.(J,X(I),P,A,B,F,DF)
            WT=DY(I).P.-2
            DIF=YS(I)-F
            WVAR=WVAR+WT*DIF.P.2
            THROUGH F9,FOR K=1,1,K.G.M
            BV(K)=BV(K)-WT*DIF*DF(K)
            THROUGH F9,FOR L=1,1,L.G.M
F9          AM(K,L)=AM(K,L)+WT*DF(K)*DF(L)
```

```
          CHISQ=WVAR/MDIF
          PRINT FORMAT INTRE,J,CHISQ,P(1)...P(M)
          VECTOR VALUES INTRE=$1HO,S13,I3,S3,E15.6,S5,4E15.6/(S39,4E15.
         1 6)*$

         TERMINATION OF ITERATION

          WHENEVER J-3.L.0
          TRANSFER TO F10
          OR WHENEVER WVAR-WVPRE.GE.0
          TRANSFER TO F20
          OR WHENEVER J-20.GE.0
          TRANSFER TO F19
          OTHERWISE
          CONTINUE
          END OF CONDITIONAL

         SOLUTION OF EQUATIONS

F10       THROUGH F11,FOR K=1,1,K.G.M
          Z(K)=-BV(K)
          THROUGH F11,FOR L=1,1,L.G.M
F11       PM(K,L)=AM(K,L)
          R=SLE.(M,M,PM(1),DP(1),Z(1),LR(1),0)
          WHENEVER R.LE.0
          PRINT COMMENT $0                    NORMAL EQUATIONS UNSOLVABLE
         1 , USE METHOD OF STEEPEST DESCENT$
          TRANSFER TO F13
          OTHERWISE
          CONTINUE
          END OF CONDITIONAL
          H1=0.
          THROUGH F12,FOR K=1,1,K.G.M
F12       H1=H1+DP(K).P.2*AM(K,K)
          WHENEVER SQRT.(H1).LE.INCR,TRANSFER TO F17

         METHOD OF STEEPEST DESCENT

F13       PRINT COMMENT $0                    METHOD OF STEEPEST DESCENT
         1 USED$
          H1=0.
          H2=0.
          THROUGH F14,FOR K=1,1,K.G.M
F14       H1=BV(K).P.2
          THROUGH F15,FOR K=1,1,K.G.M
          THROUGH F15,FOR L=1,1,L.G.M
F15       H2=H2+BV(K)*AM(K,L)*BV(L)
          THROUGH F16,FOR K=1,1,K.G.M
F16       DP(K)=-H1*BV(K)/H2

F17       WVPRE=WVAR
          THROUGH F18,FOR K=1,1,K.G.M
F18       P(K)=P(K)+DP(K)
          J=J+1
          TRANSFER TO F8
```

```
          TERMINATION OF ITERATION

F19         PRINT COMMENT $0                    NO CONVERGENCE AFTER 20 ITE
           1 RATIONS$
F20         PRINT COMMENT $0                    FINAL RESULTS$

          NORMALIZATION OF DATA

            AREA=0.
            THROUGH F21,FOR I=ILP,1,I.G.IUP
            EXECUTE THEORY.(J,X(I),P,A,B,F,DF)
            FIT(I)=B-1.
            YNRM(I)=(YS(I)-A)/A
            DYNRM(I)=DY(I)/A
            DIFF(I)=YNRM(I)-FIT(I)
F21         AREA=AREA-FIT(I)

          CALCULATION OF ERRORS

            PRINT FORMAT INITAL,SETUP(1)...SETUP(24)
            PRINT COMMENT $0
           1 FINAL RESULTS$
            THROUGH F22,FOR K=1,1,K.G.M
            THROUGH F22,FOR L=1,1,L.G.M
F22         PM(K,L)=AM(K,L)
            RS=GJR.(M,M,PM(1),DETER)
            WHENEVER RS.NE.1
            PRINT COMMENT $0                    MATRIX INVERSION UNSUCCESSF
           1 UL$
            THROUGH F23,FOR K=1,1,K.G.M
F23         SIG(K)=0.
            TRANSFER TO F25
            OTHERWISE
            CONTINUE
            END OF CONDITIONAL
            THROUGH F24,FOR K=1,1,K.G.M
            INVDI(K)=PM(K,K)
F24         SIG(K)=SQRT.(CHISQ*.ABS.INVDI(K))

          ERROR DISTRIBUTION

F25         SD=SQRT.(A)/A
            EXECUTE ZERO.(P3S,P2S,P1S,P0S,N0S,N1S,N2S,N3S)
            THROUGH F26,FOR I=ILP,1,I.G.IUP
            WHENEVER DIFF(I).G.SD*3.,P3S=P3S+1
            WHENEVER DIFF(I).G.SD*2..AND.DIFF(I).L.SD*3.,P2S=P2S+1
            WHENEVER DIFF(I).G.SD*1..AND.DIFF(I).L.SD*2.,P1S=P1S+1
            WHENEVER DIFF(I).G.0.AND.DIFF(I).L.SD*1.,P0S=P0S+1
            WHENEVER DIFF(I).G.-SD*1..AND.DIFF(I).L.0,N0S=N0S+1
            WHENEVER DIFF(I).G.-SD*2..AND.DIFF(I).L.-SD*1.,N1S=N1S+1
            WHENEVER DIFF(I).G.-SD*3..AND.DIFF(I).L.-SD*2.,N2S=N2S+1
F26         WHENEVER DIFF(I).L.-SD*3.,N3S=N3S+1
```

```
          DATA PRINT OUT

            PRINT COMMENT $0                                    FITTING PARAMETER
           1 S$
            THROUGH F27,FOR K=1,1,K.G.M
F27         PRINT FORMAT PAROUT,K,P(K),SIG(K)
            VECTOR VALUES PAROUT=$S20,I3,10H PARAMETER,S5,E15.6,4H +- ,E1
           1 5.6*$
            PRINT FORMAT AROUT,AREA,P3S,P2S,P1S,P0S,N0S,N1S,N2S,N3S
            VECTOR VALUES AROUT=$1H0,S19,6HAREA= F12.4//S20,18HERROR DIST
           1 RIBUTION,8I5*$
            PRINT FORMAT INITAL,SETUP(1)...SETUP(24)
            PRINT COMMENT $0                          CHANNEL           MEASURE
           1 D             FITTED         DIFFERENCE           MEASURED$
            PRINT COMMENT $                            NUMBER           SPECTRU
           1 M           SPECTRUM         IN SPECTRA              ERROR$
            THROUGH F28,FOR I=ILP,1,I.G.IUP
F28         PRINT FORMAT DATOUT,I,YNRM(I),FIT(I),DIFF(I),DYNRM(I)
            VECTOR VALUES DATOUT=$S25,I5,4E18.8*$

          DATA PLOT

            PRINT FORMAT INITAL,SETUP(1)...SETUP(24)
            PRINT COMMENT $0                                      PLOT OF MO
           1 SSBAUER SPECTRUM VS CHANNEL NUMBER$
            EXECUTE ZERO.(ZP(1)...ZP(IM))
            YMAX=0.
            YMIN=0.
            DMAX=0.
            DMIN=0.
            THROUGH F29,FOR I=ILP,1,I.G.IUP
            XX(I)=-I
            WHENEVER YNRM(I).G.YMAX,YMAX=YNRM(I)
            WHENEVER YNRM(I).L.YMIN,YMIN=YNRM(I)
            WHENEVER DIFF(I).G.DMAX,DMAX=DIFF(I)
F29         WHENEVER DIFF(I).L.DMIN,DMIN=DIFF(I)
            DELY=YMAX-YMIN
            DELD=DMAX-DMIN
            YMAX=YMAX+.1*DELY
            YMIN=YMIN-.1*DELY
            DMAX=DMAX+.1*DELD
            DMIN=DMIN-.1*DELD
            SP=IUP-ILP
            FILP=ILP
            FIUP=IUP
            EXECUTE PLOT1.(0,1,SP,1,100)
            EXECUTE PLOT2.(IMAGE,YMAX,YMIN,-FILP,-FIUP)
            EXECUTE PLOT3.($-$,ZP(ILP),XX(ILP),SP+1)
            EXECUTE PLOT3.($*$,FIT(ILP),XX(ILP),SP+1)
            EXECUTE PLOT3.($+$,YNRM(ILP),XX(ILP),SP+1)
            EXECUTE PLOT4.(1,$ $)
```

```
      PRINT FORMAT INITAL,SETUP(1)...SETUP(24)
      PRINT COMMENT $0                                          PLOT OF ER
     1 ROR VS CHANNEL NUMBER$
      EXECUTE PLOT1.(0,1,SP,1,100)
      EXECUTE PLOT2.(IMAGE,DMAX,DMIN,-FILP,-FIUP)
      EXECUTE PLOT3.($-$,ZP(ILP),XX(ILP),SP+1)
      EXECUTE PLOT3.($*$,DIFF(ILP),XX(ILP),SP+1)
      EXECUTE PLOT4.(1,$ $)
      TRANSFER TO START
      END OF PROGRAM
```

2. Theory Subroutine (Sample)

```
      EXTERNAL FUNCTION(JT,XT,PT,AT,BT,FT,DFT)
      DIMENSION PPT(25)
      INTEGER JT,I
      ENTRY TO THEORY.

     THEORY FOR CUCR2TE4 SPECTRUM, SIX LINES, R LESS THAN 0, CONST
     RAINED INTENSITIES, SAME WIDTHS, P2, 256,SLOPE

     CODE 6L,3INT-CONSTR,1LW,R.L.0,IS,P2,256,SL

      THROUGH T1,FOR I=1,1,I.G.25
T1    PPT(I)=PT(I)

      X1=127.5+PPT(3)+PPT(2)*(3*PPT(6)-1)
      X2=127.5+PPT(3)+PPT(2)*(PPT(6)-1)
      X3=127.5+PPT(3)+PPT(2)*(-PPT(6)-1)
      X4=127.5+PPT(3)-PPT(2)*(-PPT(6)-1)
      X5=127.5+PPT(3)-PPT(2)*(PPT(6)-1)
      X6=127.5+PPT(3)-PPT(2)*(3*PPT(6)-1)
      I1=PPT(5)*PPT(1).P.2
      I2=2*PPT(5)*PPT(1).P.2
      I3=3*PPT(5)*PPT(1).P.2
      D1=PPT(1).P.2+(XT-X1).P.2
      D2=PPT(1).P.2+(XT-X2).P.2
      D3=PPT(1).P.2+(XT-X3).P.2
      D4=PPT(1).P.2+(XT-X4).P.2
      D5=PPT(1).P.2+(XT-X5).P.2
      D6=PPT(1).P.2+(XT-X6).P.2
      C1=2.0*I3*(XT-X1)/D1.P.2
      C2=2.0*I2*(XT-X2)/D2.P.2
      C3=2.0*I1*(XT-X3)/D3.P.2
      C4=2.0*I1*(XT-X4)/D4.P.2
      C5=2.0*I2*(XT-X5)/D5.P.2
      C6=2.0*I3*(XT-X6)/D6.P.2
```

```
  BT=1.0-I3/D1-I2/D2-I1/D3-I1/D4-I2/D5-I3/D6-PPT(7)*XT
  AT=PPT(4)
  E=2.0*PPT(1)
  FT=AT*BT
  G=-AT*PPT(1).P.2
  H=(I3-3.0*PPT(5)*D1)/D1.P.2+(I2-2.0*PPT(5)*D2)/D2.P.2+(I1-PPT
1 (5)*D3)/D3.P.2+(I1-PPT(5)*D4)/D4.P.2+(I2-2.0*PPT(5)*D5)/D5.P.
2 2+(I3-3.0*PPT(5)*D6)/D6.P.2
  DFT(1)=AT*E*H
  DFT(2)=AT*((3.0*PPT(6)-1.0)*(C6-C1)+(PPT(6)-1)*(C5-C2)+(-PPT(
1 6)-1)*(C4-C3))
  DFT(3)=-AT*(C1+C2+C3+C4+C5+C6)
  DFT(4)=BT
  DFT(5)=G*(3.0/D1+2.0/D2+1.0/D3+1.0/D4+2.0/D5+3.0/D6)
  DFT(6)=AT*PPT(2)*(-3.0*C1-C2+C3-C4+C5+3.0*C6)
  DFT(7)=-AT*XT
  FUNCTION RETURN
  END OF FUNCTION
```

REFERENCES

1. J. A. Stone and W. L. Pillinger, Phys. Rev. Letters, 13, 200 (1964).

2. D. Seyboth, F. E. Obenshain, and G. Czjzek, Phys. Rev. Letters, 14, 954 (1965).

3. Y. K. Lee, P. W. Keaton, Jr., E. T. Ritter, and J. C. Walker, Phys. Rev. Letters, 14, 957 (1965).

4. G. Czjzek, J. L. C. Ford, Jr., F. E. Obenshain, and D. Seyboth, Phys. Letters, 19, 673 (1966).

5. G. Czjzek, J. L. C. Ford, Jr., J. C. Love, F. E. Obenshain, and H. H. F. Wegener, Phys. Rev. Letters, 18, 529 (1967).

6. S. L. Ruby and R. E. Holland, Phys. Rev. Letters, 14, 591 (1965).

7. D. A. Goldberg, P. W. Keaton, Jr., Y. K. Lee, L. Madansky, and J. C. Walker, Phys. Rev. Letters, 15, 418 (1965).

8. J. Christiansen, E. Recknagel, and G. Weyer, Phys. Letters, 20, 46 (1966).

9. D. W. Hafemeister and E. B. Shera, Phys. Rev. Letters, 14, 593 (1965).

10. U. Gonser and H. Wiedersich, J. Phys. Soc. Japan, 18, Suppl. II, 47 (1963).

11. P. H. Dederichs, C. Lehmann, and H. Wegener, Phys. Stat. Sol., 8, 213 (1965).

12. V. N. Belogurov, Phys. Stat. Sol., 10, K41 (1965).

13. J. Fink and P. Kienle, Phys. Letters, 17, 326 (1965).

14. D. A. Goldberg, Y. K. Lee, E. T. Ritter, R. R. Stevens, Jr., and J. C. Walker, Phys. Letters, 20, 571 (1966).

15. P. Hannaford, C. J. Howard, and J. W. Wignall, Phys. Letters, 19, 257 (1965).

16. F. E. Obenshain and W. Berger, Bull. Am. Phys. Soc., II, 12, 24 (1967).

17. E. P. Stepanov and A. Yu Aleksandrov, JETP Letters, 5, 83 (1967).

18. H. C. Schweinler, J. Appl. Phys., 30, 1125 (1959).

19. R. M. Walker, J. Nucl. Mat., 2, 147 (1960).

20. J. H. Crawford and J. W. Cleland, Radioisotopes in the Physical Sciences and Industry, IAEA, Vienna, 269 (1962).

21. R. Oswald and C. Kikuchi, Nuclear Sci. Eng., 23, 354 (1965).

22. C. Barnes and C. Kikuchi, ORA Technical Report, University of Michigan, Ann Arbor (1967).

23. J. C. Danko, G. R. Kilp, and P. V. Mitchell, Advanced Energy Conversion, 2, 79(1962).

24. R. T. Frost, J. C. Corelli, and M. Balicki, Advanced Energy Conversion, 2, 77 (1962).

25. J. C. Corelli, R. T. Frost, and D. M. Amorosi, IRE Trans. on Nuclear Science, NS-9, 303 (1962).

26. V. A. J. van Lint, E. G. Wikner, and P. H. Miller, Jr., GA-1513 (1960).

27. E. G. Wikner, GACD-2699 (1961).

28. P. Z. Hien, V. G. Shapiro, and V. S. Shpinel, Soviet Physics JETP, 15, 489 (1962).

29. C. E. Violet, D. L. Davis, and R. Booth, UCRL-7045 (1962).

30. C. E. Violet, R. Booth, and F. Wooten, Phys. Letters, 5, 230 (1963).

31. C. E. Violet and R. Booth, UCRL-12438 (1965); Phys. Rev., 144, 225 (1966).

32. A. B. Buyrn and L. Grodzins, Bull. Am. Phys. Soc., 8, 43 (1963).

33. N. Shikazono, J. Phys. Soc. Japan, 18, 925 (1963).

34. R. B. Frankel, P. H. Barrett, and D. A. Shirley, Bull. Am. Phys. Soc., 7, 600 (1962).

35. P. H. Barrett, R. B. Frankel, and D. A. Shirley, UCRL-10624 (1962).

36. E. P. Stepanov, K. P. Aleshin, R. A. Manapov, B. N. Samoilov, V. V. Sklyarevsky, and V. G. Stankevich, Phys. Letters, 6, 155 (1963).

37. R. B. Frankel, J. Huntzicker, E. Matthias, S. S. Rosenblum, D. A. Shirley, and N. J. Stone, UCRL-11882 (1965); Phys. Letters, 15, 163 (1965).

38. A. H. Muir, Jr., K. J. Ando, and H. M. Coogan, Mössbauer Effect Data Index, Issue 3 (1965).

39. D. J. Hughes and R. B. Schwartz, BNL-325, Second Edition, Supplement No. 2 (1965).

40. L. V. Groshev, A. M. Demidov, V. N. Lutsenko, and V. I. Pelekhov, translated by J. B. Sykes, Atlas of γ-Ray Spectra from Radiative Capture of Thermal Neutrons, Pergamon Press (1959).

41. H. C. Schweinler, Chemical Effects of Nuclear Transformations, IAEA, Vienna, 1, 63 (1963).

42. D. S. Billington and J. H. Crawford, Jr., Radiation Damage in Solids, Princeton University Press, Princeton, New Jersey (1961).

43. G. J. Dienes and G. H. Vineyard, Radiation Effects in Solids, Interscience Publishers, Inc., New York (1957).

44. F. Seitz, Dis. Faraday Soc., 5, 271 (1949).

45. R. H. Bube, Photoconductivity of Solids, John Wiley and Sons, Inc. (1960).

46. I. N. Rozantsev, Izv. Akad. Nauk. SSSR, Ser. Fiz. 28, 88 (1964).

47. R. S. Narcisi, Tech. Report No. 2-9, Department of Physics, Harvard University (1959).

48. A. H. Wapstra, G. J. Nijgh, and R. Van Lieshout, Nuclear Spectroscopy Tables, Interscience Publishers, Inc., New York (1959).

49. H. Frauenfelder, The Mössbauer Effect, W. A. Benjamin, Inc., New York (1962).

50. G. K. Wertheim, Mössbauer Effect: Principles and Applications, Academic Press (1964).

51. D. A. Shirley, Rev. Mod. Phys., 36, 339 (1964).

52. P. Brix and H. Kopfermann, Rev. Mod. Phys., 30, 517 (1958).

53. M. H. Cohen and F. Reif, Solid State Physics, Vol. 5, Academic Press (1957).

54. F. W. deWette, Phys. Rev., 123, 103 (1961).

55. R. Bersohn, J. Chem. Phys., 29, 326 (1958).

56. J. S. Geiger, R. L. Graham, I. Bergstroem, Nucl. Phys., 68, 352 (1965).

57. H. E. Weaver, Jr., Phys. Rev., 89, 923 (1953).

58. R. E. Watson and A. J. Freeman, Phys. Rev., 123, 2027 (1961).

59. A. J. Freeman and R. E. Watson, in Magnetism (G. T. Rado and H. Suhl, editors), Vol. II, Part A, Academic Press, New York (1965).

60. R. G. Shulman and V. Jaccarino, Phys. Rev., 108, 1219 (1957).

61. A. J. Freeman and R. E. Watson, Phys. Rev. Letters, 6, 343 (1961).

62. E. Kankeleit, Rev. Sci. Inst., 35, 194 (1964).

63. D. Rubin, Rev. Sci. Inst., 33, 1358 (1962).

64. H. DeWaard, G. DePasquali, and D. Hafemeister, Phys. Letters, 5, 217 (1963).

65. M. Kalvius, in Mössbauer Effect Methodology (I. J. Gruverman, editor), Vol. 1, Plenum Press, New York (1965).

66. H. Marshall, in Inorganic Syntheses (Ludwig F. Audrieth, editor-in-chief), Vol. 3, McGraw-Hill (1950).

67. V. P. Zlomanov, A. V. Novoselova, A. S. Pashinkin, Yu P. Simanov, K. N. Semenenko, Zhur. Neorg. Khim., 3, 1473 (1958).

68. W. A. Dutton and W. Charles Cooper, Chemical Reviews, 66, 657 (1966).

69. S. Margulies and J. R. Ehrman, Nucl. Inst. and Methods, 12, 131 (1961).

70. C. Colominas, Phys. Rev., 153, 558 (1967).

71. J. B. Gibson, A. N. Goland, M. Milgram, and G. H. Vineyard, Phys. Rev., 120, 1229 (1960).

72. W. M. Visscher, Phys. Rev., 129, 28 (1963).

73. A. A. Maradudin and P. A. Flinn, Phys. Rev., 126, 2059 (1962).

74. R. G. Barnes and W. V. Smith, Phys. Rev., 93, 95 (1954).

75. W. J. Nicholson and G. Burns, Phys. Rev., 129, 2490 (1963).

76. V. I. Goldanskii, E. F. Makarov, and V. V. Kharapov, Soviet Physics JETP, 17, 508 (1963).

77. L. Pauling, The Nature of the Chemical Bond, Cornell University Press, Second Edition (1948).

78. H. Hahn, C. de Lorent, and B. Harder, Z. anorg. Chem., 283, 138 (1956).

79. F. K. Lotgering, Proc. Int. Conf. on Magnetism, Nottingham, 533 (1964).

80. P. K. Baltzer, P. J. Wojtowicz, M. Robbins, and E. Lopatin, Phys. Rev., 151, 367 (1966).

81. P. K. Baltzer, H. W. Lehmann, and M. Robbins, Phys. Rev. Letters, 15, 493 (1965).

82. N. Menyuk, K. Dwight, and R. J. Arnott, J. Appl. Phys., 37, 1387 (1966).

83. J. Kanamori, J. Phys. Chem. Solids, 10, 87 (1959).

84. P. W. Anderson, Phys. Rev., 79, 350 (1950).

85. J. C. Slater, Quart. Progr. Rep. M.I.T., July 15 and Oct. 15 (1953).

86. D. A. Shirley and G. A. Westenbarger, Phys. Rev., 138, 170 (1965).

87. R. S. Preston, S. S. Hanna, J. Heberle, Phys. Rev., 128, 2207 (1962).

88. F. K. Lotgering and E. W. Gorter, J. Phys. Chem. Solids, 3, 238 (1957).

89. J. B. Goodenough, Magnetism and the Chemical Bond, Interscience Publishers (1963).

90. W. B. Pearson, Can. J. Phys., 35, 886 (1957).

91. D. Clifton, Master's Thesis, Department of Nuclear Engineering, The University of Michigan, Ann Arbor (1966).

92. J. C. Slater, Quantum Theory of Molecules and Solids, Vol. 2, McGraw-Hill (1965).

93. H. Haraldsen and A. Neuber, Z. anorg. Chem., 234, 353 (1937).

94. L. G. Gaidukov, N. P. Grazhdakina, I. G. Fakidov, Soviet Physics JETP, 12, 636 (1961).

95. T. Hihara, Y. Kôi, and A. Tsujimura, J. Phys. Soc. Japan, 17, 1320 (1962).

96. A. Tsujimura, T. Hihara, and Y. Kôi, J. Phys. Soc. Japan, 17, 1078 (1962).

97. C. O. Muehlhause, Phys. Rev., 79, 277 (1950).

98. R. L. Mössbauer, Z. Physik, 151, 124 (1958).

99. K. S. Singwi and A. Sjölander, Phys. Rev., 120, 1093 (1960).

100. R. W. G. Wycoff, Crystal Structures, Second Edition, Interscience Publishers (1966).

101. L. N. Swink and G. B. Carpenter, Acta Cryst., 21, 278 (1966).

102. J. D. Bowman, E. Kankeleit, E. N. Kaufmann, and B. Persson, Nucl. Inst. Methods, 50, 13 (1967).

103. P. Cziffra and M. J. Moravscik, UCRL-8523 (1958).